Application of Magnetic Resonance Imaging for *in vitro* investigation of meniscus and cartilage degeneration in the knee

Manyi Wang MSc (Distinction), Bachelor of Medicine

Submitted in accordance with the requirements for the degree of

Doctor of Philosophy

The University of Leeds

School of Mechanical Engineering

June 2012

The candidate confirms that the work submitted is his own, except Chapter 5 which has formed part of jointly-authored publications, has been included. The contribution of the candidate and the other authors to this work has been explicitly indicated below.

Chapter 5 in this thesis is based on work from the jointly co-authored publication: “Wang, M., Radjenovic, A., Stapleton, T. W., Venkatesh, R., Williams, S., Ingham, E., Fisher, J., Jin, Z. (2010) A novel and non-destructive method to examine meniscus architecture using 9.4 Tesla MRI. *Osteoarthritis and Cartilage*, 18: 1417-1420.”

The ITK-SNAP 3D surface reconstruction programme with a second graphical user interface for cartilage wear quantification in chapter 4 was the work of Dr Richard Holbrey.

The candidate confirms that appropriate credit has been given within the thesis where reference has been made to the work of others.

Acknowledgements

Foremost, I would like to express my greatest gratitude to my supervisors: Professor Zhongmin Jin, Professor Eileen Ingham, Dr Aleksandra Radjenovic, Dr Sophie Williams, and Professor John Fisher for guiding me with invaluable advice and discussion through this project.

A special thanks to Dr Laura McCann for her guidance during the initial months of my project and her help in pendulum friction simulator testing and MRI experiments at 9.4 Tesla.

This work would never have been accomplished without generous help provided by Dr Aleksandra Radjenovic in all MRI experiments, and help from Dr Richard Holbrey, who developed the 3D surface reconstruction method that I applied to fulfill MRI cartilage quantification in this project.

I greatly appreciate the help I received from Dr Mike Ries and Dr Robin Damion on MRI experiments in the School of Physics. Dr Daniel Binks and Dr Richard Hodgson, thank you very much for your help with the MRI studies in the LMBRU.

I would like to thank Dr Ram Venkatesh for his kind visits to the laboratory to help develop meniscal post-surgery/damage models. I'd like to thank Miss Halina Norbertczak and Dr Thomas Stapleton for their help in Histological aspect of this project. I'd like to acknowledge the help and support received from Mrs Susanne Patel in the Pycnometer measurement. I'd like to thank Mr Aidan Hindley for preparation of human cadaver menisci samples for the MRI studies in this project. I'd like to thank all of the iMBE laboratory technicians.

A big thank you to my dear mother Zhenxiu, father Chunxin, and aunt Alice. Without your encouragement and support, I could not come to the UK to continue my study. I'd like to thank my wife Ran for her support during my PhD, and thank her for giving birth to our lovely daughter Lizi.

Abstract

Damage to the meniscus and articular cartilage in the knee can lead to loss of function and compromise joint stability. This has led to the development of *in vitro* models to investigate the biomechanics and biotribological response of cartilage and menisci. In high-volume laboratory studies of cartilage tribology, it is important to measure cartilage loss after experiments. In order to understand the relationship between the structure and function of the meniscus in health and disease, it is essential to interrogate the internal structural components of the meniscus.

The aims of this project were to optimise protocols for magnetic resonance imaging (MRI) of menisci and articular cartilage in the knee in order to gain an increased understanding of their structure, and to detect and quantify morphological changes.

A novel porcine medial knee model was developed for creation of physiological cartilage damage using a friction simulator. The cartilage damage models were subject to *in vitro* MRI quantification at both 9.4 Tesla and 3.0 Tesla for the first time. The two customised MRI-based wear quantification methods were validated using Pycnometer measurements. In addition, a novel approach was developed at 9.4T MRI to non-destructively investigate intrameniscal architecture and damage.

Cartilage defect models were successfully created on the femoral condyle and tibia after friction simulator tests. The follow-up MRI investigation demonstrated the capability of MRI to assess cartilage defects using laboratory and clinical systems. At both of 9.4T and 3.0T, the two quantification methods were in excellent agreement with each other and with Pycnometer measurements. An optimised 10-hour 3D scan at 9.4T could clearly demonstrate 3D intrameniscal architecture.

The MRI quantification protocols showed promise for the non-destructive examination and quantification of cartilage defects in a large range of animal/human tissues after biomechanical/biotribological experiments. MRI at ultra-high-field strength also showed promise for the non-destructive examination of the intrameniscal structure in a 3D manner. The proof of concept measurements presented in this study illustrates the potential of non-destructive 3D MRI microscopy to bring a unique contribution to the field of functional cartilage/meniscus biomechanics and biotribology.

Table of Contents

ACKNOWLEDGEMENTS ..... **III**
ABSTRACT ..... **IV**
TABLE OF CONTENTS ..... **V**
LIST OF FIGURES ..... **VIII**
LIST OF TABLES ..... **XIV**
ABBREVIATIONS ..... **XVI**
NOMENCLATURE ..... **XVIII**
CHAPTER 1 INTRODUCTION: LITERATURE REVIEW AND GOALS **1**
1.1 OVERVIEW OF THE KNEE JOINT 1
1.1.1 The meniscus 5
1.1.1.1 Ultrastructure of the meniscus 6
1.1.1.2 Composition of the meniscus 9
1.1.1.3 Properties and functions of the meniscus 12
1.1.2 Meniscal degradation, injuries and treatment 21
1.1.2.1 Healing mechanisms of the meniscus 21
1.1.2.2 Degeneration of the meniscus 22
1.1.2.3 Types of meniscal tears 23
1.1.2.4 Current surgical treatment 27
1.1.2.5 Replacement of the meniscus 30
1.1.3 Articular cartilage 34
1.1.3.1 Composition and structure of articular cartilage 34
1.1.3.2 Biomechanics of articular cartilage 38
1.1.3.3 Cartilage lubrication 44
1.1.4 Cartilage wear and degradation 48
1.2 MRI OF THE KNEE 51
1.2.1 MRI of the meniscus 51
1.2.2 MRI of the articular cartilage 55
1.3 PROJECT AIMS AND OBJECTIVES 56
Rationale 56
Aims and Objectives 57
CHAPTER 2 GENERAL MATERIALS AND METHODOLOGIES **58**
2.1 MATERIALS AND INSTRUMENTS 58
2.1.1 Phosphate buffered saline 58
2.1.2 PMMA bone cement 58
2.1.3 Serum 59

2.1.4 Dissection instruments 59
2.2 HARVESTING OF ANIMAL SPECIMENS 59
2.2.1 Harvesting of porcine knee for tribological experiments 60
2.2.2 Harvesting of porcine medial meniscus for MRI 63
2.3 EXPERIMENTAL METHODS 65
2.3.1 Pendulum friction simulator testing 65
2.3.2 Magnetic Resonance Imaging 68
2.3.3 Post-acquisition MR image analysis 71
2.3.4 Cartilage wear quantification 73
2.3.5 Histological staining and microscopy 75

CHAPTER 3 SIMULATION OF CARTILAGE WEAR AND DAMAGE 80
3.1 INTRODUCTION 80
3.2 MATERIALS AND METHODS 81
3.2.1 Development of porcine models 81
3.2.2 Development of friction simulation protocol 85
3.2.3 Calibration of friction simulator 90
3.2.4 Design of simulation study 90
3.2.5 Contact stress measurement 91
3.2.6 Cartilage wear quantification 92
3.3 RESULTS 92
3.3.1 Generation of cartilage wear 92
3.3.2 Wear measurement 93
3.3.3 Contact pressure measurement 94
3.3.4 Friction measurement 94
3.4 DISCUSSION 95

CHAPTER 4 MRI QUANTIFICATION OF CARTILAGE WEAR 99
4.1 INTRODUCTION 99
4.2 MATERIALS AND INSTRUMENTS 100
4.2.1 Friction simulator-tested samples 100
4.2.2 Samples for validation study 101
4.2.3 MRI scanners 102
4.2.4 Pycnometer 102
4.3 METHODS 102
4.3.1 MRI of cartilage at 9.4 Tesla 102
4.3.2 MRI of cartilage at 3.0 Tesla 105
4.3.3 MRI quantification of cartilage wear 107
4.3.3.1 Preparation of image data 107
4.3.3.2 The 2D profile method 108
4.3.3.3 The 3D surface reconstruction method 108
4.3.3.4 Study design 109

4.4 RESULTS 110
4.4.1 Validation Group 111
4.4.1.1 Wear measurement on 9.4 Tesla MR Images using 3D surface method 111
4.4.1.2 Wear measurement on 9.4 Tesla MR Images using 2D profile method 114
4.4.1.3 Wear measurement on 3.0 Tesla MR Images using 3D surface method 117
4.4.1.4 Wear measurement on 3.0 Tesla MR Images using 2D profile method 119
4.4.1.5 Validation of MRI measurement of cartilage wear 122
4.4.2 Friction Simulator-tested Group 124
4.4.2.1 Comparison between the with-meniscus group and total meniscectomy group 124
4.4.2.2 MRI wear quantification of samples underwent meniscectomy 124
4.5 DISCUSSION 125
CHAPTER 5. MRI EXAMINATION OF THE MENISCAL ARCHITECTURE 130
5.1 INTRODUCTION 130
5.2 MATERIALS AND METHODS 132
5.2.1 Materials 132
5.2.1.1 Animal menisci samples 132
5.2.1.2 Human cadaver menisci samples 132
5.2.1.3 The MRI scanners 133
5.2.2 Methods 133
5.2.2.1 Ultra-High-Field MRI 133
5.2.2.2 Clinical MRI at 3.0 Tesla 137
5.2.2.3 Post-acquisition image analysis 139
5.2.3 Histology of MRI-examined samples 139
5.3 RESULTS 139
5.3.1 UHF MRI of the meniscus 139
5.3.2 MRI of menisci at 3.0T 147
5.4 DISCUSSION 148
5.5 CONCLUSION 152
CHAPTER 6. OVERALL DISCUSSION 153
CONCLUSIONS 158
REFERENCES 160

List of Figures

Figure 1.1 The drawing of (a) anterior and (b) posterior view of the human knee joint (Brukner and Khan, 2007)……..……1

Figure 1.2 A sagittal diagram of the knee joint…….. 2

Figure 1.3 Sagittal MR images of cadaveric medial tibio-femoral compartment at full extension (left image) and 120 degrees (right image)…….3

Figure 1.4 Photos of menisci. A) Medial meniscus in human cadaveric knee (Lee et al., 2006). B) A plan view of the tibial plateau (covered with the menisci) of a deer knee (the website of Fankhauser (2008), University of Cincinnati)…….5

Figure 1.5 Illustration of the anterior view of the knee with patella removed. The two meniscotibial ligaments which anchor the two menisci to the tibia are highlighted by circle (the website of the University of Oregon)…….6

Figure 1.6 Illustrations of the ultrastructure of the meniscal fibrils. (a) Fibrous structures reported by Bullough, *et al*. (1970). (b) A model of the ultrastructure of the meniscal fibrils (Petersen *et al*., 1998)…….....……...7

Figure 1.7 Diagram showing the mean movement (mm) in each meniscus from extension (shaded) to flexion (dashed) in (A) the weight-bearing and (B) the unloaded knee. (Vedi *et al*., 1999)……..….17

Figure 1.8 A virtual lateral view of the tibiofemoral compartment with and without meniscus……..17

Figure 1.9 Diagrammatic representation of different geometries of medial and lateral compartments in the sagittal plane without menisci, leading to differences in joint congruity. (McDermott 2006)…….18

Figure 1.10 Diagrammatic representation of load transmission of menisci (McDermott, 2006)……19

Figure 1.11 A diagram of four basic types of meniscus tears (Englund *et al*., 2001)……...24

Figure 1.12 Illustration of different degrees of longitudinal tears……..24

Figure 1.13 Schematic drawing of VMS technique (Remesz, 2007)……28

Figure 1.14 An illustration of the “four-layer” structure of articular cartilage…37

Figure 1.15 A tensile-strain curve of cartilage……..39

Figure 1.16 Schematic of a confined compression test (Eisenberg and Grodzinsky, 1987)…….40

Figure 1.17 Stress-relaxation test of cartilage tissue in confined compression…… 41

Figure 1.18 Creep response of cartilage under a constant compression (Mow *et al*.,1980a)…….. 42

Figure 1.19 An illustration of the three major engineering friction mechanisms (Wright and Dowson, 1976)…….. 46

Figure 1.20 Grading maps of the severity of cartilage destruction on (a) tibial plateau surface; and (b) femoral condyle surface…….. 50

Figure 1.21 The GE 0.5 Tesla Open-access interventional MRI scanner with a 56 cm gap between magnets (Williams and Logan, 2004)…….. 51

Figure 2.1 Photo of the specially made clamp set for mounting and fixing the porcine femur or tibia during the cutting of bony components…….. 59

Figure 2.2 Photo of a porcine leg delivered from the local abattoir between 24-48 hours after slaughter…….. 60

Figure 2.3 Photos show trimming of condyle specimen guided by CAD templates of known radius between 20-31 mm…….. 61

Figure 2.4 Porcine medial tibial plateau with meniscus attached intact…… 61

Figure 2.5 Schematic diagram of resection of the “inner section” of the meniscus…….. 62

Figure 2.6 Development of the partial meniscectomy model for tribological experiments…….. 63

Figure 2.7 Creation of markers on the meniscus…….. 64

Figure 2.8 Images of the ProSim friction simulator……..... 65

Figure 2.9 Jigs for friction simulator testing……. 66

Figure 2.10 Femoral specimen holder with delrin jig attached……. 66

Figure 2.11 Porcine medial knee model potted in jigs separately, ready for friction simulator testing…….. 67

Figure 2.12 The 9.4 Tesla Bruker Avance™ II 400MHz laboratory NMR system……... 68

Figure 2.13 Illustration of meniscus sample preparation for the 9.4T MRI…. 69

Figure 2.14 Preparation of cartilage samples for 3.0T MRI scan……. 70

Figure 2.15 Photo of setting up of a 3.0T MRI scans of porcine meniscus sample……... 71

Figure 2.16 An example of SNR and ReCon measurement of meniscal MR images using the Analyze™ software…….. 73

Figure 2.17 Photo of the AccuPyc 1330 Pycnometer……..... 74

Figure 2.18 Sample preparation for pycnometer measurements……. 75

Figure 2.19 Dissection of meniscal tissue for histological staining…….. 76

Figure 3.1 A photograph of a right porcine leg with muscles removed from femur……..... 81

Figure 3.2 Harvest of porcine medial femoral condyle for testing on the pendulum friction simulator……..... 82

Figure 3.3 Photo of trimmed femoral condyle specimen had been set up into the jigs using screws and bone cements……. 83

Figure 3.4 Illustration of dissection of porcine tibia plateau (without meniscus)…….. 84

Figure 3.5 Schematic representation of the friction simulator hard- and soft-ware…… 86

Figure 3.6 The single peak loading profile used during friction testing…….. 87

Figure 3.7 The motion profile used during friction testing…….…….. 87

Figure 3.8 The loading and motion profiles of a demand gait cycle……..... 89

Figure 3.9 Photographs of samples after a 3,600 cycle 900 peak load friction simulator test……..... 89

Figure 3.10 Contact press measurement of porcine medial knee model..... 91

Figure 3.11 Volumes of cartilage defects of meniscectomy samples, measured using 3D surface reconstruction method on 9.4T and 3.0T MRI.. 93

Figure 3.12 Photographs of the Fuji films after a static load of 330N was applied for 15 seconds on three models……..... 94

Figure 3.13 Laboratory development of *in vitro* meniscal tear models…….. 96

Figure 4.1 Sample preparation for Pycnometer validation study…….. 101

Figure 4.2 Imaging sequence comparison for in vitro MRI of porcine medial femoral condyles at 9.4T..... 103

Figure 4.3 FISP 3D MRI of porcine medial tibia and femoral condyle with different settings of flip angle at 9.4T..... 104

Figure 4.4 Photo of 3.0T MRI scan of multiple cartilage samples..... 106

Figure 4.5 An MR image extracted from 3.0T MRI of cartilage samples..... 107

Figure 4.6 MRI quantification of cartilage wear using a 2D profile method.. 108

Figure 4.7 Illustration of a 3D wear volume measurement…… 109

Figure 4.8 Representative image slices of quantitative morphology MRI of cartilage at 9.4T (left image) and 3.0T (right image)…….. 110

Figure 4.9 Volumes of cartilage defects of 6 validation samples, measured using 3D surface reconstruction method on 9.4T MRI……..... 111

Figure 4.10 Volumes of cartilage defects of validation samples, measured using 3D surface reconstruction method on 9.4T MRI……..... 113

Figure 4.11 Volumes of cartilage defects of 6 validation samples, measured using 2D profile curve fitting method on 9.4T MRI……..... 115

Figure 4.12 Volumes of cartilage defects of validation samples, measured using 2D profile method on 9.4T MRI…… 116

Figure 4.13 Volumes of cartilage defects of 6 validation samples, measured using 3D surface reconstruction method on 3.0T MRI…… 117

Figure 4.14 Volumes of cartilage defects of validation samples, measured using 3D surface reconstruction method on 3.0T MRI…… 118

Figure 4.15 Volumes of cartilage defects of 6 validation samples, measured using 2D profile curve fitting method on 3.0T MRI……..... 120

Figure 4.16 Volumes of cartilage defects of validation samples, measured using 2D profile method on 3.0T MRI…… 121

Figure 4.17 Validation of MRI quantification of cartilage loss by Pycnometer…… 123

Figure 4.18 Volumes of cartilage defects of meniscectomy samples, measured using 3D surface reconstruction method on 9.4T and 3.0T MRI..... 125

Figure 4.19 Illustration of the tap density measurement method…….... 129

Figure 5.1 Photos of MRI scanners used in this project…… 133

Figure 5.2 Illustration of the geometry settings of MR scans of menisci..... 134

Figure 5.3 Photo shows the setting up of 3.0T MRI of a meniscus sample…… 138

Figure 5.4 Two-dimensional image slices from 9.4T MRI of porcine menisci..... 140

Figure 5.5 SNR, CNR, Relative contrast, and Voxel number per cubic millimeter of three MRI sequences……..141

Figure 5.7 Two-dimensional MR images extracted from a series of 3D FLASH MRI scans showed the internal structure of porcine knee menisci…….. 143

Figure 5.8 Comparison between MR image and histological staining sections in fibrous architecture……..... 144

Figure 5.9 Comparison of Collagen IV staining section with MR image of the same porcine meniscal sample in blood vessel distribution…….. 145

Figure 5.10 MRI of human cadaver medial menisci…… 146

Figure 5.11 Two-dimensional MRI slices of porcine meniscus at 3.0 Tesla…… 147

Figure 5.12 MR images of porcine menisci……... 150

List of Tables

Table 1.1 Reported tibiofemoral joint peak loads in human for daily activities……... 4

Table 1.2 Material properties of the meniscus and articular cartilage (Fithian *et al*., 1989)…… 15

Table 1.3 Material constants for a model determined from bovine meniscus, mean (SD). Modified from Goertzen *et al*. (1997)…….. 15

Table 1.4 A comparison of the main components of the meniscus and cartilage……. 36

Table 2.1 Formulation of PBS tablets (by MP Biomedicals)……. 58

Table 2.2 Chemicals and reagents used together with UK suppliers……. 77

Table 3.1 Reported tibiofemoral joint peak loads in animals……. 87

Table 4.1 Parameter settings of quantitative morphological MRI of cartilage at 9.4T..... 105

Table 4.2 Parameter settings of MRI of cartilage at 3.0T……. 106

Table 4.3 MRI wear quantification study design of specimen number one of the validation group……... 110

Table 4.4 Coefficient of variation of measurement using 3D surface reconstruction method on 9.4T MRI, among repeat measurements for each scan…… 112

Table 4.5 Coefficient of variation of measurement using 3D surface reconstruction method on 9.4T MRI…….. 113

Table 4.6 Coefficient of variation of measurement using 2D profile method on 9.4T MRI, among repeat measurements for each scan…….. 114

Table 4.7 Coefficient of variation of measurement using 2D profile method on 9.4T MRI…… 116

Table 4.8 Coefficient of variation of measurement using 3D surface reconstruction method on 3.0T MRI, among repeat measurements for each scan…… 118

Table 4.9 Coefficient of variation of measurement using 3D surface reconstruction method on 3.0T MRI…….. 119

Table 4.10 Coefficient of variation of measurement using 2D profile method on 3.0T MRI, among repeat measurements for each scan…… 121

Table 4.11 Coefficient of variation of measurement using 2D profile method on 3.0T MRI…….. 122

Table 4.12 The average volume of cartilage wear of specimens from validation group…… 122

Table 5.1 Information of human cadaver menisci samples…… 132

Table 5.2 Parameter settings of 9.4T Spin Echo MRI of menisci…….. 135

Table 5.3 Parameter settings of 9.4T 3D FLASH MRI of menisci…..... 136

Table 5.4 Parameter settings of the 9.4T FISP 3D MRI of menisci…….. 137

Table 5.5 Parameter settings of the 3.0T MRI of porcine menisci…… 138

Abbreviations

2D	Two-dimensional
3D	Three-dimensional
AC	Articular cartilage
CMI™	collagen-glycosaminoglycan meniscal implant
CNR	Contrast to noise ratio
DESS	Dual echo at steady state
dGEMRIC	Delayed gadolinium enhanced MRI of cartilage
ECM	Extracellular matrix
FISP	Fast imaging with steady-state precession
FLASH	Fast low angle shot
FOV	Field of view
GAG	Glycosaminoglycan
GUI	Graphical user interface
H&E	Haematoxylin and eosin
IW	Intermediate-weighted
LMBRU	Leeds Musculoskeletal Biomedical Research Unit
MPa	Magapascal
MRI	Magnetic Resonance Imaging
MTF	modulation transfer function
NaCl	Sodium chloride
NMR	Nuclear magnetic resonance
OA	Osteoarthritis
PBS	Phosphate buffered saline

PGA	Polyglycolic acid
PRG4	Proteoglycan 4
PMMA	Polymethyl-methacrylate
ReCon	Relative contrast
SE	Spin echo
SIS	small intestinal submucosa
SNR	Signal to noise ratio
T	Tesla
TE	Echo time
TR	Relaxation time
TSE	Turbo spin echo
UHF	Ultra-high-field
VMS	Vertical mattress suture

Nomenclature

B_0	Main magnetic field strength
f	friction factor
σ	contact stress
R_1	radius
Ra	Arithmetic mean of absolute departure of roughness profile form the mean line
T	frictional torque
μ	coefficient of friction
W	applied load

Chapter 1 Introduction: Literature Review and Goals

1.1 Overview of The Knee Joint

The knee joint is the lower extremity joint connecting the femur, tibia and patella. It is the largest and most complex synovial joint in the human body and is made up of three bones which are covered in cartilage at the bone ends. Menisci are situated between the tibio-femoral articulation, and ligaments and muscles connect the bones and control movement. The knee is also one of the most vulnerable joints to both trauma and the development of degenerative lesions (Al-Turaiki, 1986)

Geometry and structure

The skeletal structure of the human knee joint comprises the femoral condyles, tibial plateau and the patella, forming the two functional compartments: the tibio-femoral articulation and the patello-femoral articulation. The fibula might also be considered to be part of the knee due to the importance of the articulation of fibula and tibia in weight bearing (Figure 1.1).

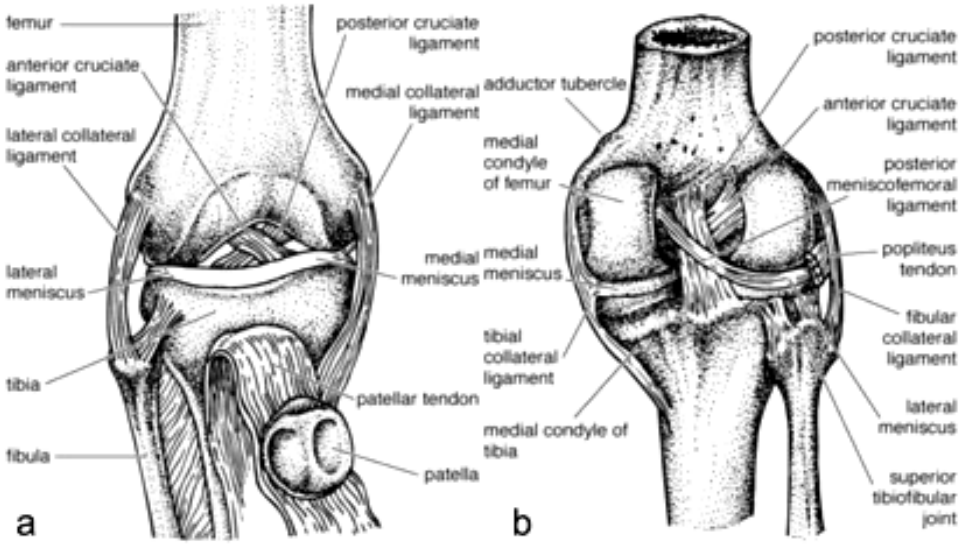

Figure 1.1 The drawing of (a) anterior and (b) posterior view of the human knee joint (Brukner and Khan, 2007).

The knee joint is a typical synovial joint, which has a synovial cavity between the primary articulation and it is wrapped by connective tissue of the articular capsule, with the opposing bone surfaces being covered by articular cartilage (Figure 1.2). The capsule is lined by a synovial membrane (Tortora and Derrickson, 2006). On the femur, the articular capsule of the knee attaches posteriorly around the articular margins of the condyles and above the inter-condylar notch. On the tibia, the attachment of the articular capsule is located near the articular cartilage. The articular capsule consists of three parts, an inner synovial membrane, fatty deposits, and an outer fibrous layer. It seals the joint space, and provides stability to the joint passively by limiting the movement and actively through reactions of proprioceptive nerve endings (Ralphs and Benjamin, 1994).

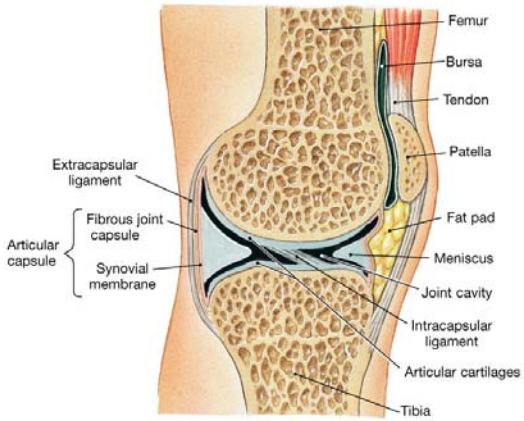

Figure 1.2 A sagittal diagram of the knee joint. (Image from the Internet, http://iupucbio2.iupui.edu/anatomy/images/Chapt08/FG08_01b.jpg)

The capsule is further reinforced by three major ligament groups: the lateral (fibular) collateral ligament which is the major ligamentous support of the knee; the medial (tibial) collateral ligament and the cruciate ligaments.

The shapes of the distal end of femur and the proximal end of tibia are very incongruous. In human, the shape of the femoral condyle is more round, while the upper surface of the tibia is flat and called the tibial plateau. In the medial compartment, the articular surface of the medial condyle is posteriorly circular

as shown in Figure 1.3 (Freeman and Pinskerova, 2005), and the femoral condyle moves no more than ±1.5mm anteroposteriorly when the knee is flexed from 0 to 120 degrees whether weight-bearing and non-weight-bearing (Johal *et al*., 2005). The radii of the curvatures of the femoral condyles differ and the medial condyle is longer than the lateral condyle. Excellent stability can be achieved within the knee joint due to the support of the ligament groups and menisci. The menisci are 'semi-lunar' shaped fibrocartilaginous tissues which are present between the articulating surfaces of the tibio-femoral compartment. A more detailed discussion of the menisci is given in Section 1.1.1.

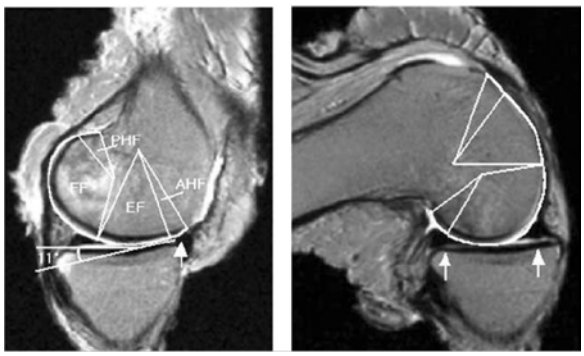

Figure 1.3. Sagittal MR images of cadaveric medial tibio-femoral compartment at full extension (left image) and 120 degrees (right image).

Motion and loads

As one of the major lower extremity joints, the knee joint has two main functions. Firstly, the knee facilitates ambulation and other purposeful motion, secondly it bears and transmits load. Due to the incongruity of the articulating surfaces, the knee differs from a simple hinge joint in the performance of flexion or extension. During knee flexion or extension, an axis-shifting rotation can be observed. Hallén and Lindahl (1966) reported a 7° outward rotation when the knee passively extended from 160° of flexion to full extension. This can be explained by a so-called "screw-home mechanism", which means that when the knee joint is nearly fully extended, there is a relative rotation between the tibia and femur. This will eventually screw the two bones together at full extension (Whiting and Zernicke, 1998).

The total range of motion of the knee is dependent on several factors such as the geometry of the joint surfaces, surrounding soft-tissue restraints, active insufficiency, and hamstring tightness (Lawrence *et al*., 2006). During daily movements a large range of flexion is required at the knee. Lamoreaux (1971) used exoskeletal linkages to measure the rotations at the knee joint during walking. Flexion of up to 65°-70°, internal rotation of up to 9° and external rotation of up to 12°, were reported. To stand from a chair, flexion of about 100° was observed and from a very low chair or stool this increased to 120°. Greater degrees of flexion are required for more strenuous activities such as squatting or kneeling (Dowson and Wright, 1981).

The knee is located below the centre of gravity of the body, which results in large loads acting on the knee. The tibio-femoral joint bears an average load of 1.2 to 20 times the body weight (Table 1.1). The patello-femoral joint bears a similar extent of loading as the tibio-femoral joint during daily activities (Matthews *et al*., 1977; Nisell, 1985; Ericson and Nisell, 1987). However, no details of the load of the patello-femoral joint will be discussed since this is beyond the scope of this study.

Table 1.1 Reported tibiofemoral joint peak loads in human for daily activities

Authors	**Activity**	**Tibio-femoral joint load (body-weight multiples)**
Collins (1995)	Level walking	3.9-6.0
Taylor (2004)	Level walking	3.0-3.3
	Stair climbing	5.1-5.9
Kuster (1997)	Level walking	3.9
	Downhill walking	8.0
Andriacchi (1980)	Downstairs walking	6.0
Ericson (1986)	Cycling	1.2
Maquet (1975)	Running & jumping	Up to 20

1.1.1 The meniscus

The meniscus, also known as ‘semi-lunar’ cartilage, is the crescent-shaped wedge of fibro-cartilage present within the knee joint, situated between the femoral condyles and tibial plateau. In each knee joint, there are two menisci, which lie between the two femoral condyles and the tibial plateau. The freshly dissected meniscus is white (yellow or light brown in older people) and glossy (Figure 1.4). The superior surface of the meniscus is concave in shape which accommodates the relatively round femoral condyles, while the inferior surface of the meniscus is flat or slightly convex and conforms with the tibial plateau. This wedge shape is very important in providing conformity between the two highly incongruent articular surfaces, ensuring smooth movement of the knee joint.

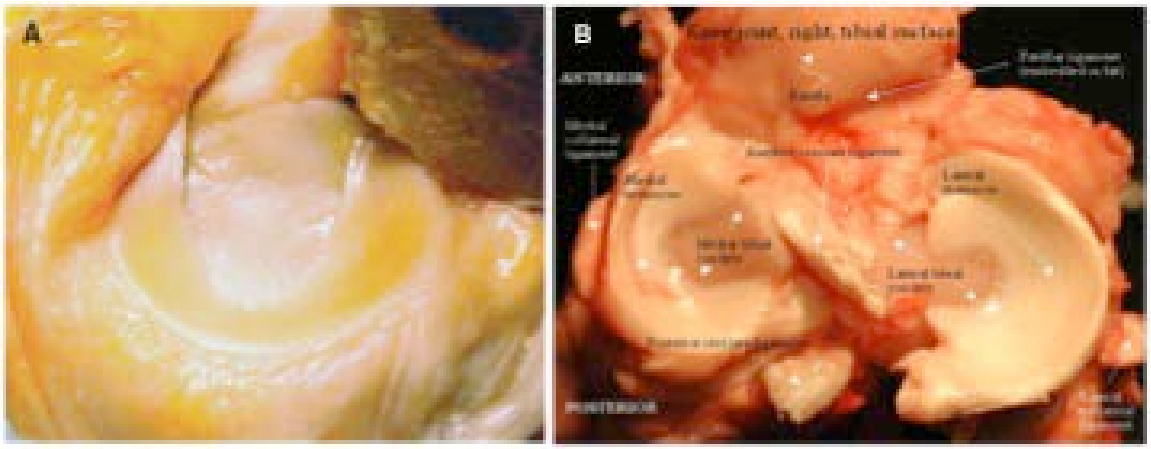

Figure 1.4 Photos of menisci. A) Medial meniscus in human cadaveric knee (Lee *et al*., 2006). B) A plan view of the tibial plateau (covered with the menisci) of a deer knee (the website of Fankhauser (2008), University of Cincinnati).

The medial and lateral menisci are not symmetrical in shape nor are their anatomical attachments. The medial meniscus is more C-shaped, while the lateral meniscus is more circular or O-shaped and therefore it covers a relatively larger portion of the tibial surface than the former. Both of the menisci have anterior and posterior horns which inserted into the intercondylar fossa. The medial meniscus is wider near the posterior horn and narrower near the anterior horn, while the lateral meniscus is almost uniform

in width from anterior to posterior. Peripherally, the medial meniscus is continuously attached to the joint capsule, with the middle portion being more firmly attached via the fibers of the deep medial collateral ligament. In contrast, the peripheral capsular attachment of the lateral meniscus is not continuous, with a non-attached area in the middle one-third. However, like the medial meniscus, this middle third of the lateral meniscus is anchored to the tibia via meniscotibial ligaments (Figure 1.5).

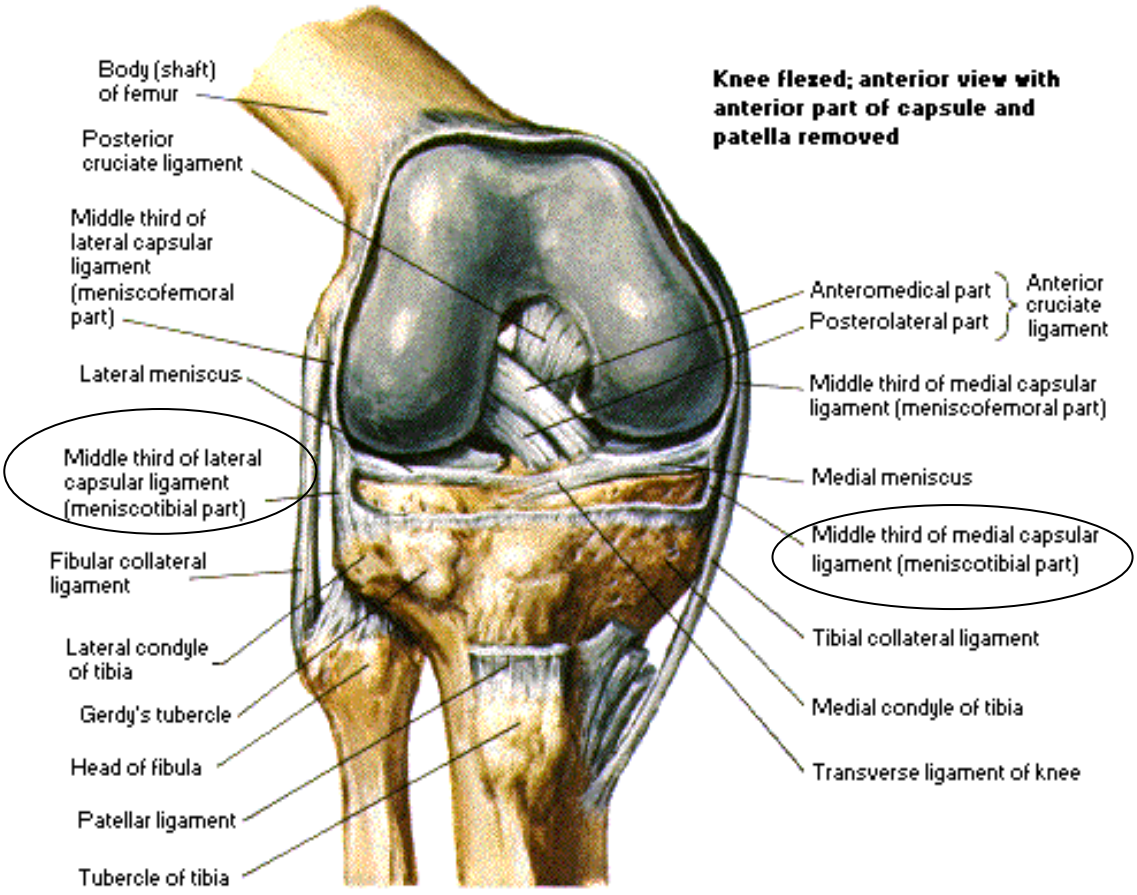

Figure 1.5 Illustration of the anterior view of the knee with patella removed. The two meniscotibial ligaments which anchor the two menisci to the tibia are highlighted by circle (the website of the University of Oregon).

1.1.1.1 Ultrastructure of the meniscus

The fibrous structure of the meniscus has a layered appearance. Bullough *et al*. (1970) introduced a three-dimensional model of the collagen distribution in

the meniscus tissue based on sectional photomicrographs (Figure 1.6-a), Petersen *et al*. (1998) drew a similar model based on scanning electron microscopy images (Figure 1.5-b).

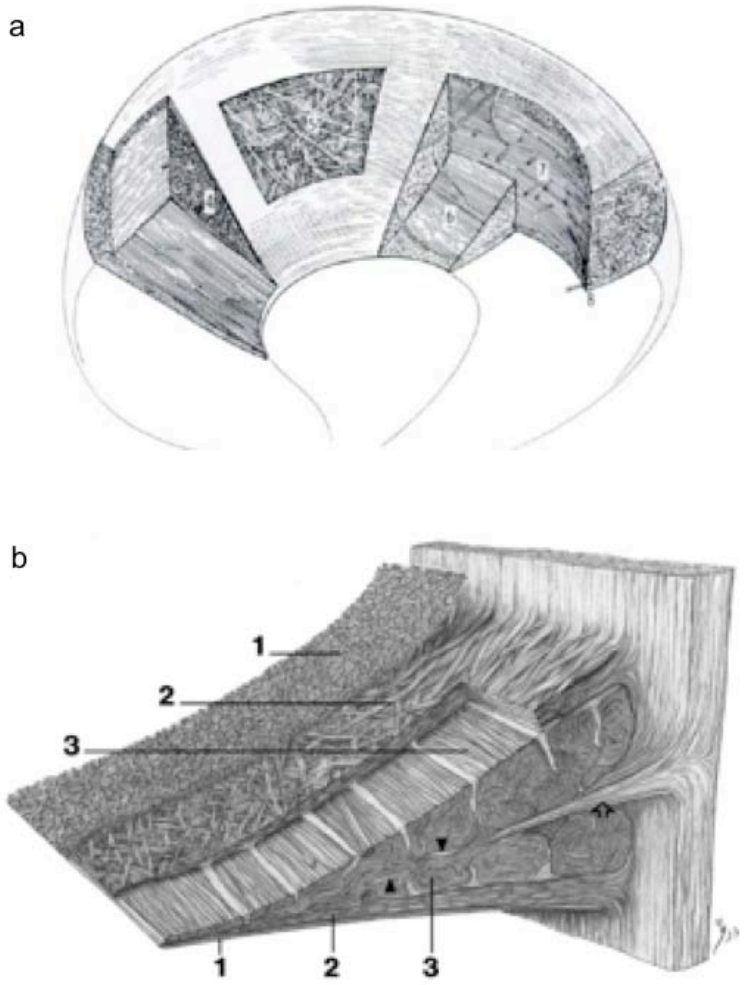

Figure 1.6 Illustrations of the ultrastructure of the meniscal fibrils. (a) Fibrous structures reported by Bullough, *et al*. (1970). (b) A model of the ultrastructure of the meniscal fibrils (Petersen *et al*., 1998). 1: The superficial network: a meshwork of thin fibrils; 2: Lamellar layer: fibrils are arranged radially in external circumference, and oriented randomly in other parts; Central main layer: fibrils are orientated in a circular manner. Arrowheads: a few radial (tying) fibrils are interwoven with the circular fibril bundles; Arrow: loose connective tissue from the joint capsule penetrates radially between the circular fibril bundles.

The meniscal surface in contact with the femur is dominated by randomly-woven, meshlike fine fibril bundles. Approximately 100 μm inferior to the surface layers are large rope like collagen fiber bundles that are principally

arranged circumferentially around the semi lunar meniscus. Radially arranged collagen fibers which tie the large circumferential fiber bundles together, are also present. More of these radial fibers exist near the tibial surface and the “inner third” (Nakano *et al*., 1986). Their function is to reinforce the structure of the meniscus.

According to the degree of fibrillar organisation, the meniscal tissue can be considered as two zones. The peripheral two-thirds is predominantly fibrillar, whereas the inner one-third appears to contain more randomly arranged smaller collagen fibers and proteoglycans, resembling hyaline cartilage (Ghosh *et al*., 1983; Nakano *et al*., 1986).

Meniscus vascularisation

Vascularisation can be identified in almost the entire meniscus in humans at birth. However, in adults only the outer rim (approximately 30% of the medial and 25% of the lateral meniscus) of the meniscus has a blood supply, whereas at least two thirds of the meniscus tissue becomes totally avascular (Petersen and Tillmann, 1995; Boyd and Myers, 2003). The region of the anterior horn is the most vascularised area of the meniscus, with 22 – 83% of the area showing vascularity in the medial meniscus and 18 – 95% in the lateral meniscus (Braz and Silva, 2010). The superior and inferior medial and lateral geniculate arteries are the main blood supplier to the meniscus. The middle geniculate artery and synovial fringe vessels also supply blood through peripheral vascularisation (DeHaven and Arnoczky, 1994).

A more surgically valid zonal division is based on the vascularity within the meniscus tissue. Only the outer 30 to 40% of the meniscus has a capillary blood supply, which is so called the “red zone”. The inner two-thirds is avascular and hence called the “white zone”.

1.1.1.2 Composition of the meniscus

Based on Mow's biphasic theory (Mow *et al*., 1980a), the meniscus can be regarded as a biphasic material which has two phases: a fluid phase and a solid phase (Favenesi *et al*., 1983). The fluid phase consists of water, which accounts for 70 to 75% of the wet weight of the fresh meniscus, and ions. The solid phase consists of chondrocytes, collagen, proteoglycans and other proteins such as elastin (Mow *et al*. 1980a; Mow and Huiskes, 2005). If dehydrated, up to 70% of the meniscal dry weight is collagen (Eyre and Muir, 1975), 1 to 2% proteoglycans, and 8 to 13% noncollagenous proteins such as elastin (Mow *et al*., 1980b; Fithian *et al*., 1989; Fithian *et al*., 1990; Mow and Huiskes, 2005). No significant difference between the composition of the medial and lateral menisci of the human knee joint has been reported (Peters and Smillie, 1972).

Fluid phase (interstitial water and electrolytes)

Water is the most abundant component of the meniscus. Peters and Smillie (1972) measured the water content of normal human menisci to be 73.6% ±2.1. Compared to human menisci, bovine menisci have a similar mean water content (73.8 ±3.1%), while the value of canine menisci is approximately 10% lower (63 ±2%) (Proctor, *et al*., 1989; Adams and Muir,1981).

Hellio Le Graverand *et al*. (1999) compared the water content of medial menisci with lateral menisci in rabbits, and found no statistically significant difference between the two. Proctor *et al*. (1989) demonstrated that the water distribution within the meniscus varied significantly with respect to the anterior-posterior location rather than with depth. The posterior part of the meniscal tissue had about 3% higher water content than the anterior tissue.

Mow and Huiskes (2005) summarised that the water distribution of the meniscus is mainly controlled by its solid phase, especially collagens and

proteoglycans. The glycosaminoglycans of proteoglycans attract water molecules and generate high interstitial swelling pressure, whereas the collagen network restrains this pressure and limits the tissue's water content.

Collagen

Collagen is the most abundant protein in the human body. It is a rod-shaped molecule with a high degree of right-handed triple helix structure that is made up of three polypeptide α chains. These three α chains can be either identical or different, for example, type I collagen is composed of two α1(I) and one α2(I) polypeptide chains (Eyre and Muir, 1975; Eyre, 1980). The collagen fibrils in tissues are often heterogeneous, containing more than one type of collagen.

In the collagen family, there are at least 28 sub-types, which altogether account for about 30% of body's total protein (Di Lullo *et al*., 2002; Horton *et al*., 2006). In the meniscus, 90% or more of its collagen content belongs to type I, with small amounts of type II, III, V and VI (Eyre and Muir, 1975; Eyre and Wu, 1983; Mow and Huiskes, 2005).

Collagen is a key structural component of load-bearing tissues such as meniscus and articular cartilage. Collagen fibrils form the tissue structure by directly providing tensile stiffness and strength, and they also maintain the compression stiffness of the tissue by restraining the swelling pressure of the embedded proteoglycans (Stanescu, 1990).

Proteoglycans

Proteoglycans (PGs) are heavily glycosylated proteins that have one core protein and one or more glycosaminoglycan (GAG) chains. Unlike collagen, PGs can hardly be classified as one protein family because of their diverse combinations of core protein and GAG chains, and also their complex molecular structures (Hardingham, 1981; Muir, 1983). The following species

of PGs are present in the meniscus: aggrecan, decorin, biglycan, versican and fibromodulin (Fosang and Hardingham, 1996; Hellio Le Graverand *et al*., 1999). In adult human meniscus, aggrecan and decorin are the dominant PGs with a ratio of 4:3 (Roughley and White, 1992).

As one of the dominant PGs in the meniscus, aggrecan is responsible for resisting compressive loading. Much of the compressive strength of aggrecan is derived from the glycosaminoglycan molecules which have abundant carboxyl and sulfate groups that are negatively charged under physiologic conditions. These negatively charged GAGs will derive a swelling pressure which resists the compressive forces. This will be discussed in more detail in Section 1.2.3. Decorin and fibromodulin are PGs that also play important roles in the organisation of the meniscal extracellular matrix, and their function is to bind the proteoglycans to the collagen fibrils (Hardingham and Fosang, 1992).

Elastin

Elastin is an important non-collagen fibrillar component found in the meniscus, and it accounts for 0.47-0.64% of the dry weight of the meniscus (Peters and Smillie, 1972). The elastin molecules are composed of loose and unstructured tropoelastin polypeptide chains, and are embedded in fibrillin micro-fibres which are cross-linked by covalent bonds to form elastin fibers. These fibers are found throughout the meniscal tissue, normally oriented in parallel but occasionally perpendicular to collagen fibres, bridging the adjacent collagen fibers and enabling the meniscus to recover to its previous shape after deformation without fracture (Hopker *et al*.,1986; Alberts *et al*., 2006).

Meniscal cells

Meniscal cells are termed as “fibrochondrocytes” because they posses characteristics of both chondrocytes and fibroblasts (Webber *et al*., 1985). The predominant morphology of meniscal cells resembles that of the chondrocytes of articular cartilage. For example, the fibrochondrocytes of the

meniscus are oval or spindle-shaped with a few small processes in superficial layers, while they are rounded or polygonal with more processes in deeper zones (McDevitt and Webber, 1990; Sweigart *et al*., 2003).

The meniscal fibrochondrocytes produce predominantly type I collagen with smaller amounts of types II, III, V and VI collagens, and small amounts of aggrecan (Tanaka *et al*., 1999). Hence, when considering cell products, meniscal fibrochondrocytes are more like fibroblasts, rather than chondrocytes which mainly synthesise type II collagen.

Nakata *et al*. (2001) reported that there are various subtypes of the fibrochondrocytes existing in the meniscus, and their distribution is consistent with a previous study by Moon *et al.* (1984), who found that the inner rim of the meniscus contains chondrocyte-like cells, whereas the periphery of the meniscus contains cells that are fibroblast-like. McDevitt and Webber (1990) explained that this cell distribution correlates with the functional aspects of the tissue. The inner rim of the meniscus is mainly responsible for load bearing within the knee joint, hence the meniscal tissue of this area should be capable of resisting compressive forces and shear stress, which means there must be sufficient GAGs. Therefore, chondrocyte-like cells are dominant in the inner rim due to their ability to produce GAGs. The periphery is responsible for shock absorption, is subjected mainly to tensile hoop stresses, and therefore contains large amounts of type I collagen that is produced by fibroblast-like cells.

1.1.1.3 Properties and functions of the meniscus

The properties and functions of the knee meniscus have been studied for decades but have never been completely understood. To date, the majority of studies of meniscal properties have been focused on biophysical behavior. Very little literature is available on the tribological properties of the meniscal

tissue, except some joint lubrication studies which indicated that the lubrication mechanism of the meniscus may improve the tribological behavior of the knee joint (Schumacher *et al*., 2005; Sun *et al*., 2006). Some reported functions of the meniscus include load bearing and transmission, shock absorption, joint stabilisation and joint lubrication (Shelbourne and Gray, 2000; Schumacher *et al*., 2005; McDermott, 2006; McDermott *et al*., 2008). Innervation of human menisci has also been reported, which suggests that menisci might be able to function simultaneously during activities (Assimakopoulos and Katonis, 1992; Ashraf *et al*., 2011). Being regarded as a biphasic tissue, the meniscus fulfils its functions through interactions within and between the fluid and solid phases, and also through the co-operation with other tissues such as ligament groups.

Material properties of the meniscus

To fully understand the fundamental behaviour of the meniscus, it is necessary to have a comprehensive knowledge of the material properties of the meniscus. Fithian *et al*. (1989) compared the material constants (tension, compression and shear) and the permeability of the bovine meniscus with bovine articular cartilage (Table 1.2), and they found that the meniscal tissue was only half as stiff, and one sixth as permeable as articular cartilage. In a later published paper Fithian and coworkers (1990) confirmed the biphasic nature of the meniscal tissue which was first proposed by Favenesi *et al*. (1983). Spilker *et al*. (1992) presented a finite element model of the meniscus and using this model, they studied the response of the meniscus to different loading conditions. They observed an expected fluid motion, and found that the pressure of the fluid phase of the meniscus was larger than either axial or radial normal stress, and concluded that the fluid phase played an important role in carrying loads at early times after the onset of loading.

The anisotropic nature of the meniscal tissue was firstly reported by Whipple *et al*. (1985). They found that samples which were taken tangentially to

collagen fibers had a much greater tensile modulus (198.4 MPa) compared to samples taken radially (2.8 MPa). Fithian *et al*. (1990) also mentioned that the meniscus was anisotropic in compression. In a more recent study, Goertzen *et al*. (1997) used a specifically designed methodology and confirmed that the meniscal tissue belongs to a specific class of anisotropic materials which is transversely isotropic. They obtained a more detailed list of material constants of the meniscus (Tale 1.3). It should be noted that the tensile modulus of the anterior horn of the meniscus was higher than that of the posterior horn (Lechner *et al*., 2000), which is not shown in Table 1.2 and 1.3.

The characteristic material properties of the meniscus can to some extent explain the major function of the meniscus within the knee joint. When under compression, the meniscus serves as a highly efficient shock absorber and load distributor. This is due to the combination of its low compression stiffness (i.e., highly deformable) and low permeability (i.e., can maintain the high fluid pressure by resisting any easy fluid flow) compared to articular cartilage. However, the current methodologies used to study biomechanical properties of the meniscal tissue have limitations. For example, Lechner *et al*. (2000) found that the selection of test meniscus sample thickness had a great impact on test results, which indicated that previous estimates of material property constants of meniscal tissue were questionable. Therefore, it is challenging to fully understand the function of the meniscus.

Table 1.2 Material properties of the meniscus and articular cartilage (Fithian *et al*., 1989)

	Tension (MPa)				
Site	**Parallel**	**90°**	**Compression (MPa)**	**Shear (MPa)**	**Permeability (m^4/Ns)**
Meniscus	**59.8 (s)**	**59.8 (s)**	**0.42**	**0.112 (a)**	**0.81×10^{-15}**
	198.4 (m)	**2.8 (m)**		**0.130 (c)**	
	138.0 (d)	**4.6 (d)**			
Cartilage	**10.2 (s)**	**3.24 (s)**	**0.79**	**0.68**	**4.7×10^{-15}**
	3.2 (m)	**1.01 (m)**			
	0.87 (d)	**0.32 (d)**			

MPa = mega-pascals. Ns = Newton second, s = surface, m = middle, d = deep. a = axial. c = circumferential, 90° = perpendicular to split-lines (articular cartilage) or circumferential fiber bundles (meniscus).

Table 1.3 Material constants for a model determined from bovine meniscus, mean (SD). Modified from Goertzen *et al*. (1997).

	Young's modulus (MPa)	Poisson's ratio	Shear modulus (MPa)
Longitudinal	**316 (146)**	**0.78 (0.23)**	
Transverse	**25.2 (17.7)**	**0.88 (0.34)**	
Isotropic	**20.6 (7.5)**	**0.95 (0.20)**	**5.4 (2.3)**

Collagen-proteoglycan interactions

The collagen fibrils and proteoglycan networks interact with each other to maintain the stability of the meniscus or articular cartilage, as well as providing important functions (Mow *et al*., 1992; Mow and Huiskes, 2005). Firstly, the GAG chains of proteoglycans are anionic due to the high content of negatively charged sulfate and carboxyl groups, making the GAG chains hydrophilic. This means that they attract water molecules and restrict the flow of water. Taking into account that the natural tendency of GAG is to repel each other, and also repel the negatively charged ions dissolved in the interstitial fluid, proteoglycans induce a high osmotic swelling pressure, inflating the tissue. This swelling pressure is restrained by collagen fibres

which form networks to entangle and immobilise aggregates of large proteoglycans (Stanescu, 1990).

The main function of the collagen-proteoglycan interactions includes maintenance of the ECM organization, providing shear stiffness through the swelling pressure to resist compressive forces and shear stress and resisting tensile hoop stress through the circumferential collagen networks.

Load bearing and transmission

During loading of the knee joint, the meniscus (mainly the inner part) can resist the compressive forces by its internal swelling pressure, and after loading, it can recover from deformation.

Macroscopically, although the knee meniscus is attached firmly to the tibial plateau by the anterior and posterior horn, it is capable of small-scale movements during knee flexion. Vedi *et al*., (1999) used an open MRI system to study *in vivo* meniscal movements, and found that upon load bearing, if the knee moved from full extension to 90 degree flexion, the anterior horns of the lateral and medial menisci could move an average of 9.1 mm and 7.1 mm, respectively. The lateral and mediolateral radial movements of the menisci were 3.7 mm and 3.6 mm, respectively (Figure 1.7). A more recent study by Yao *et al*. (2008) reported similar results, and this anterior-posterior motion allows the meniscus to maintain the articular congruency and optimise the load bearing function of the knee joint.

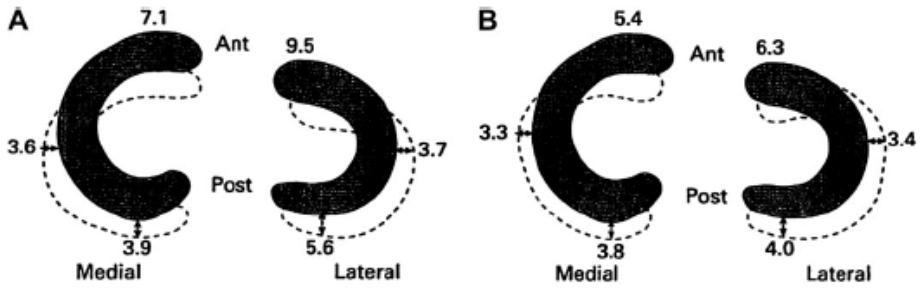

Figure 1.7 Diagram showing the mean movement (mm) in each meniscus from extension (shaded) to flexion (dashed) in (A) the weight-bearing and (B) the unloaded knee. (Vedi *et al*., 1999)

When under loading, the meniscus deforms into a transversely broader and sagittally thinner shape, resulting in an increase of the contact areas of the intra-articulation. A number of studies have demonstrated that under a high load (1000 to 1472 N), the meniscus could cover up to 71% of the joint contact surface area (Walker and Erkman, 1975; Fukubayashi and Kurosawa, 1980). An increase of contact area consequently mitigates the peak local contact stresses on the articulating cartilage (Figure 1.8).

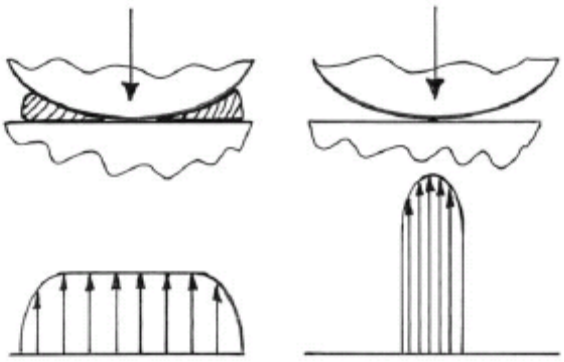

Figure 1.8 A virtual lateral view of the tibio-femoral compartment with and without meniscus.

Baratz *et al*. (1986) concluded that after total meniscectomy, the peak contact stresses increased by more than twice the value when the meniscus was present, because the contact areas decreased by approximately 75% without the menisci. McDermott (2006) further added that it was the lateral tibio-

femoral compartment which tended to undergo point loading and hence bear high peak contact stresses after meniscectomy (Figure 1.9). An in vitro study Fukuda *et al*. (2000) showed a significant increase in the stress in the subchondral bone of the porcine knee joint after meniscectomy. McCann *et al*. (2009) used a tribological simulation of the medial compartmental bovine knee to study the friction and wear of articular cartilage, with and without the meniscus. They found that with the meniscus, the peak contact stresses within articular cartilage were less than 5 MPa even under a peak loading of 1000 N. In contrast, the peak contact stresses could be increased to 17.1 MPa if the meniscus was removed.

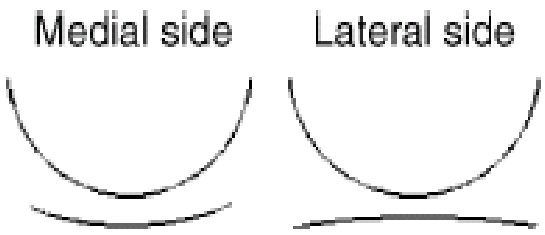

Figure 1.9 Diagrammatic representation of different geometries of medial and lateral compartments in the sagittal plane without menisci, leading to differences in joint congruity. (McDermott 2006)

Different percentages of loads that the menisci carry within the knee joint have been reported. A study by Krause *et al*. (1976) demonstrated that human meniscus specimens carried 30 to 50% of the load in the medial compartment, and a similar result was found by Ihn *et al*. (1993). Seedhom *et al*. (1974; 1979), however calculated that the menisci would carry more than 50 per cent of the joint load. Ahmed *et al*. (1983) reported that when then knee joint was at 90 degree of flexion, the menisci would accommodate 85% of the joint load.

The meniscus transmits loads between the femur and tibia. When the femoral condyles press on the meniscus, the latter will gain a tendency to be extruded towards the periphery (Figure 1.10 a). The anterior and posterior cruciate

ligaments restrict this extrusion and thus transmit some of the load through their structure (from the femur to the tibia, through their surfaces which are not in direct contact.). At the same time the tensile hoop stress, which is generated within the circumferentially arranged collagen fibres transferring the axial force, resists a further increase in meniscal radius (Figure 1.10 b). The rest of the load acting through the joint would be transmitted onto the areas of direct contact between the condyles.

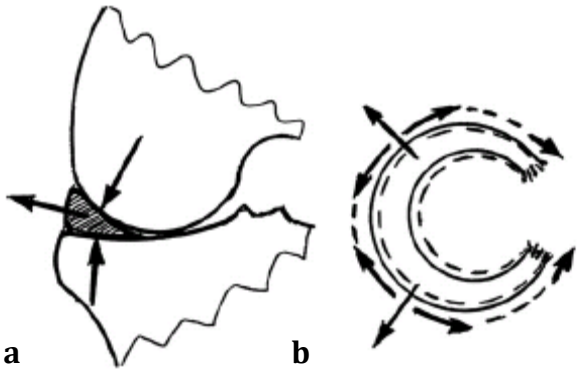

Figure 1.10 Diagrammatic representation of load transmission of menisci (McDermott, 2006).

Shock absorption

There are two major mechanisms of shock absorption by the meniscus. Firstly, the meniscus reduces the peaks in the axial forces transmitted across the knee, and transmits these forces as tensile hoop stresses within the circumferential collagen fibres. Secondly, when the meniscus tissue is deformed under compression, energy is further absorbed by the expulsion of the fluid phase of the meniscus (McDermott *et al*., 2008). Voloshin and Wosk (1983) used an accelerometric method to access the shock absorbing capacity of the knee menisci, and they found that after total meniscectomy the knee lost approximately 20% of its shock absorption capability.

Joint stabilisation

Studies of the consequences of total meniscectomy have also shown that the menisci act as the secondary stabiliser of the knee joint. An early study by

Tapper and Hoover (1969), in which 113 patients were followed up at 10 to 30 years after their meniscectomy, showed that 24% of them could be diagnosed as having knee instability.

Hsieh and Walker (1976) measured the effect of the removal of the menisci without cutting any other structures. They found that at zero degrees of flexion the meniscus had a relatively greater effect (approximately 4-degrees difference) on the joint laxity than at 0 to 30 degrees of knee flexion. However, after cutting the cruciate ligaments, the meniscus showed its potential capabilities in joint stabilisation. A similar result was found by Levy *et al.* (1982), which suggested that when the anterior cruciate ligament (ACL) was disrupted, the medial meniscus restrained the tibia from further anterior displacement. In a further study, Levy *et al.* (1989) confirmed that lateral meniscectomy after resection of the anterior cruciate ligament resulted in a small, but significant, further increase in anterior translation.

After studying medial and lateral meniscectomy separately, Levy *et al*. (1989) concluded that compared to medial meniscectomy, the removal of the lateral meniscus could lead to a smaller increase in anterior laxity. This may be explained by the fact that the lateral meniscus is more mobile than the medial. However, the relatively immobile posterior horn of the medial meniscus would resist the posterior translation of the medial femoral condyle, hence a medial meniscectomy might have a greater effect on the knee joint's stability. This has been confirmed by several recent studies. Allen *et al*. (2000) showed that after medial meniscectomy, in the anterior cruciate ligament (ACL) deficient knee, there was a significant increase in induced anterior tibial translation of up to 5.8 mm. Shelbourne and Gray (2000) followed up a large population of patients at 5 to 15 years after ACL reconstruction surgery. They reported that patients who had their medial meniscus partially or totally removed had greater laxity on a KT-1000 arthrometer manual maximum testing and lower subjective scores than patients in the non-meniscectomy group and lateral-meniscectomy group. They suggested that the medial meniscus might

contribute to the long-term knee stability after ACL reconstruction. Bahr *et al*. (2004) argued that the lateral knee meniscus may also have an effect on joint stability for its "…greater functional significance…". In conclusion, the meniscus is now been considered as a secondary knee joint stabiliser that it is only inferior to the ACL.

Joint lubrication

A study by Schumacher *et al*. (2005) indicated that proteoglycan 4 (PRG4), which is also called 'lubricin' and thought to be involved in the joint's boundary lubrication (Jay *et al*., 1992), can be synthesised by meniscal cells. PRG4 was found to be present not only at the surface of, but also within the meniscus tissue (along the tie and circumferential fibres). Sun *et al*. (2006) confirmed the presence of PRG4 in canine meniscus. Therefore, the meniscus may contribute to knee joint lubrication, especially when boundary lubrication is initiated. Moreover, Schumacher *et al*. (2005) postulated that PRG4 also lubricated the microcosmic relative motions of fibres within the peripheral zone of the meniscus, due to its unique deeper distribution in the meniscus tissue compared to a superficial distribution in the articular cartilage. The details of joint lubrication will be discussed in Section 1.1.3.3.

1.1.2 Meniscal degradation, injuries and treatment

The knee meniscus is highly vulnerable to injuries, which are commonly in the form of tears. Similar to other load-bearing biological tissues, the meniscus is prone to physiological degeneration and presents wear, fraying or calcification. However, due to its avascular nature, the healing of the meniscus is always a major challenge to surgeons.

1.1.2.1 Healing mechanisms of the meniscus

The meniscus has limited capability to heal because the majority of the tissue is avascular and alymphatic. Any injuries which occur in the vascular zone,

commonly called “red-red or red-white tears”, may possibly heal, while injuries located in the avascular zone, the “white-white tears”, are very unlikely to heal (DeHaven and Arnoczky, 1994). Mankin (1982) summarised that the response to trauma in the white zone mainly includes two phases: necrosis or cell division, without any inflammation phase (exudation, organisation, vascularisation) which is important in any repair process. Furthermore, existing chondrocytes are the only cells that can respond to the trauma, however, their number is small and they are not metabolically active. Therefore, it is very difficult for white-zone injuries to heal.

1.1.2.2 Degeneration of the meniscus

For decades, the degeneration of the meniscus has been observed by investigators both macroscopically (through surgery or necropsy) and microscopically (by histological studies). Noble and Hamblen (1975) studied 400 menisci of random necropsy cases of over 60 years olds, aiming to investigate the correlations between the meniscal degeneration and the horizontal cleavage tear. The authors found that the surfaces of many menisci were frayed due to degeneration. They also examined the menisci histologically, and found either degeneration of the cartilaginous matrix or proliferation of meniscal cells, and also, 18% of the examined menisci showed calcification.

Recently, interest has been attracted to the MRI studies of the knee meniscus (Reicher *et al.*, 1986; Lee *et al*., 2002; Yao *et al.*, 2008; Griffin *et al.*, 2008). Most of these studies are based on diagnostic medical MR images, for detecting meniscal tears. In contrast, very few studies have reported upon quantitative studies of meniscal degenerative changes which can be asymptomatic. Kornick *et al*. (1990) and Jerosch *et al.* (1994) graded the meniscal degenerate changes based on MR signals, however, they did not further investigate the relevant morphological changes and volume loss of the meniscus tissue.

In summary, a process of natural deterioration of the meniscus with increasing age has been demonstrated through imaging modalities. However, compared to the studies of degeneration of articular cartilage, the number of studies of degeneration of the meniscus is still rather limited.

1.1.2.3 Types of meniscal tears

Tear is the major form of meniscal injury, and it has been identified as an important risk factor for knee osteoarthritis (Ding *et al*. 2007; Englund *et al*. 2003; Hunter *et al*. 2006). There are several ways to categorise meniscal tears. Based on morphological appearance, meniscal tears can be classified into four basic types: longitudinal, horizontal, radial, and flap tears (Figure 1.11). Though there are more complicated tear types such as parrot beak tears, they are beyond the scope of this study, hence only the aforementioned four basic types will be discussed.

Meniscal tears can also be classified as peripheral and central, according to their anatomical locations. Many of the longitudinal tears are peripheral, whereas horizontal and radial tears are the main kind of central tears, and they are more common than peripheral tears (Bahr *et al*. 2004). Based on their causative factors or chronicity, meniscal tears have been further classified into two categories, which are traumatic tears and degenerative tears (Englund *et al.*, 2001).

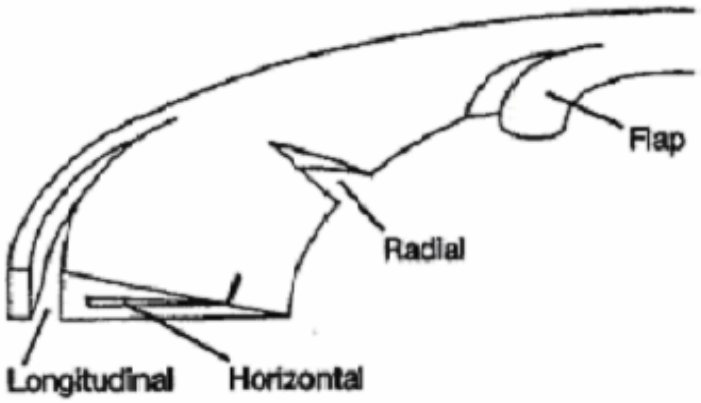

Figure 1.11 A diagram of four basic types of meniscus tears (Englund *et al*., 2001).

Traumatic tears

The longitudinal tear, also known as the vertical tear, is regarded as the traumatic tear because it mainly results from a severe knee rotation manoeuvres such as tackling in rugby or swinging in football. These sports-induced injurious tears mainly result from rapid flexion-rotation or extension-rotation during weight bearing, and they usually occur in conjunction with ligament injuries or chondral damage. Moreover, they may develop into a more severe version such as a bucket handle tear (Figure 1.12). By studying a finite element model of the meniscus, Spilker *et al*. (1992) proposed a hypothesis that the bucket handle tear could be caused by a large tensile strain, and the mid to outer third of the meniscal geometry was most susceptible to the bucket handle mode of failure.

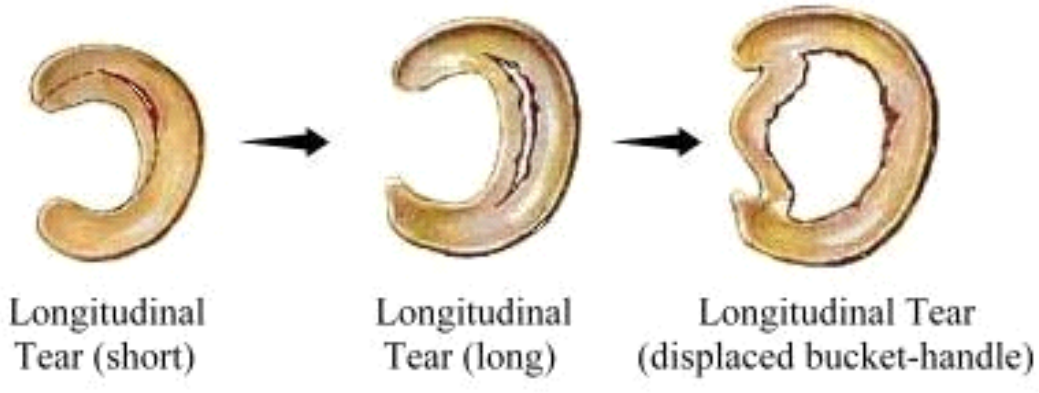

Figure 1.12 Illustration of different degrees of longitudinal tears.

When the bucket handle tears occur, the loose peripheral portion may jam into the femoral condyle notch and cause “locked knee”, which means that the knee cannot be straightened (Brown, 2004; Roberts, 2004). In most cases of longitudinal meniscal tears, the tear occurs in the periphery of the meniscus. Therefore, the collagen structure may not be disrupted severely and the vascular supply may be in contact with the damaged area. Both of these conditions allow a chance of healing. Approximately 85% of injuries of this type can achieve restoration of natural tissue after repair, providing that the diagnosis can be made within 1 to 2 weeks (Bahr *et al*., 2004; Boyd and Myers, 2003).

Degenerative tears

The horizontal, radial and flap tears have been classified as degenerative tears by Englund *et al*. (2001). The causes of these tears can be non-sports injuries, such as crouching. Unlike the traumatic tears, these degenerative tears may cause mild or low-grade pain and other symptoms at the beginning. However, with the progress of degeneration, knee problems will eventually arise (Bahr *et al*., 2004).

Horizontal tears

In most cases, horizontal tears develop from subtle collagen–related degradation in the early degenerate meniscus (Boyd and Myers, 2003). Due to degenerative changes of collagen fibres, inconsistent shear stresses between superior and inferior layers of the meniscus may result in a lesion inside the tissue. If they communicate with the periphery, a cyst may also develop. Horizontal tears are often not repairable, and the treatment mainly aims to relieve symptoms (Boyd and Myers, 2003).

Radial tears and flap tears

Radial tears are the vertical tears starting in the free (central) margin of the meniscal tissue. This tear type is usually a consequence of ACL disruption. If radial tears can be detected when they are of small range, they can be sutured through arthroscopy and the tissue can still possibly resume its function partially (Noyes *et al*., 2000; Boyd and Myers, 2003). However, when radial tears extend to peripheral regions, the chances of complete healing are small due to the disruption of circumferential collagen fibrils, which are mainly responsible for resisting tensile hoop stresses. Flap tears are oblique vertical cleavages which occur in two or more planes within the meniscal tissue. These complex tears are reported to be irreparable.

Effects of meniscal tear types on underlying cartilage

An *in vivo* clinical trial by Moffet *et al.* (1998) proposed an interesting issue that different meniscal tear types may have different impact on the degeneration of underlying cartilages. The authors studied 35 patients with confirmed medial meniscus tears of three different types (bucket-handle, flap and degenerative). Through arthroscopy, they found that 10 patients' knee cartilage (femoral, tibial and/or patellar) showed associated degenerative lesions, and among three groups 63% were degenerative-tear patients, 20% were flap-tear patients, and 17% were bucket-handle patients. A retrospective study by Christoforakis *et al*. (2005) suggested that the horizontal cleavage tear and complex tears (those tears in two or more planes within the meniscal tissue) were highly associated with an increase in incidence and severity of articular cartilage degeneration than other patterns of injuries such as bucket handle, radial and flap. This difference may be due to the fact that different types of tear particularly influence different functional zones of the meniscus, and the impact on the underlying cartilage can be different. Hitherto, evidence for the effects of meniscal tear types on the underlying cartilage are limited, hence more clinical and experimental studies are required in this area.

1.1.2.4 Current surgical treatment

Many factors should be considered when deciding on a treatment plan for a patient with meniscal tears. Besides age, health and activity level, the type of the tear (orientation, extent, and location) is the main issue of concern, the location of the tear being the most crucial factor. Whether the tear is in the red or white zone will have a large impact on the healing process as described in Section 1.1.2.1.

Techniques of meniscal repair

Orthopedic surgeons often perform meniscus surgery by arthroscopy, a sophisticated endoscopic technique designed for arthrological study, to both examine and repair the inside of a joint. In general, if a meniscal tear can satisfy most of the following description, it is suitable for repair: the tear should be fresh, full-thickness, vertical, solo (with no associated damage), and more than 7 or 8 mm in longitudinal extension if located in the vascularised periphery (DeHaven *et al*., 1994; Boyd and Myers, 2003). Boyd and Myers (2003) pointed out that partial-thickness tears in the red zone may heal spontaneously and may not require treatment. Additionally, short tears (less than 7 mm) also frequently heal spontaneously or be asymptomatic even when left untreated. Therefore, only longer longitudinal tears would be considered for repair (DeHaven *et al*., 1994).

The repair techniques include open, outside-in, inside-out and all-inside repairs. In the past, many surgeons preferred the open technique, in which the knee capsule would be incised open for surgical operation (DeHaven *et al*., 1994). However, in recent years, the all-inside repair has been widely used, as a result of the advances in arthroscopy technique (Haklar *et al*., 2008). The vertical mattress suture (VMS) is now the gold standard suture technique used in meniscal repair (Figure 1.13), while some other suture techniques such as cruciate suture have also been reported to have good results (Abdelkafy, 2007). To date, some medical devices are used for all-inside

repairs. In an *in vitro* study by Chang *et al*. (2005), two suture devices, a commonly available FastT-Fix device (Smith & Nephew Endoscopy Inc, US) and a relatively new Meniscal Viper Repair System (Arthrex, US) were compared with the gold-standard VMS on porcine meniscus specimens by subjecting to cyclic testing and load-to-failure testing. The results showed that the conventional VMS technique was superior to the FastT-Fix and Viper Repair System in meniscal repair, while the two devices had better ultimate tensile load and stiffness in load-to-failure testing.

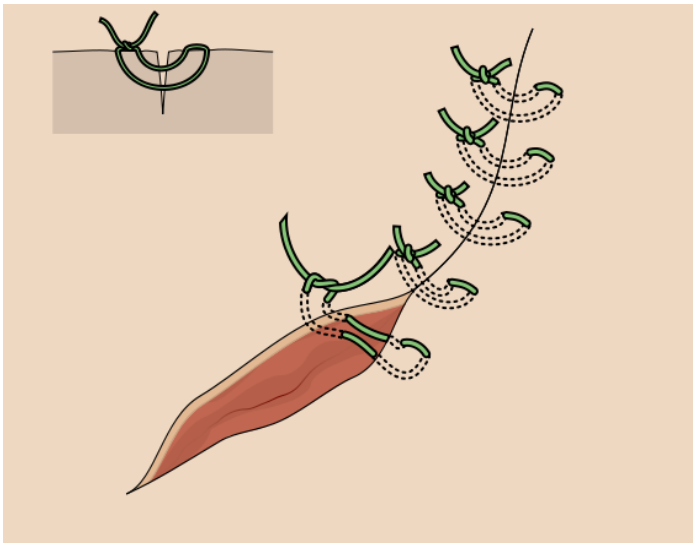

Figure 1.13 Schematic drawing of VMS technique (Remesz, 2007).

Usually near-complete healing is only achievable if the tears are located in the outer peripheral third of the menisci, and approximately 85% of injuries from this region regain native function after repair (Boyd & Myers, 2003). Ahn *et al*. (2008) also reported that nearly complete healing had been achieved by using the all-inside repair technique in patients with a lateral meniscus root tear, which is a type of tear that occurs less than 10 mm from the posterior insertion.

However, it should be noticed that even fully healed menisci might not regain normal biomechanical strength. Roeddecker *et al*. (1994) showed evidence that at 12 weeks post meniscal suture, the meniscal strength was significantly reduced to only 26% of normal. Soejima *et al*. (1997) argued that, even

though the meniscal repair techniques showed better results than partial meniscectomy cases, they could not supply significant improvement in the prevention of deterioration of the underlying cartilage.

There are two main drawbacks associated with these repair techniques, which are greater peri-operative morbidity and a long rehabilitation period. Therefore, currently a meniscal repair would only be considered when the surgeon anticipates a high degree of success and benefit (McGinty *et al*., 2002).

Partial meniscectomy

Partial meniscectomy would be considered when repair is thought to be unachievable. When carrying out partial meniscectomy, the first and foremost thing for surgeons to bear in mind is that the normal meniscus tissue must be preserved as much as possible.

As discussed in Section 1.1.1.3, the meniscus provides many important functions within the knee joint such as shock absorption and load transmission. Since the 1970's, studies have revealed that partial and total removal of the menisci have different degrees of effect on knee degeneration (Johnson *et al*., 1974; Cox *et al*., 1975; McGinty *et al*., 1977; Wilson *et al*., 2003). A retrospective study showed that 39% less patients suffered degenerative changes of the knee after partial meniscectomy than those who had a total meniscectomy (Andersson-Molina *et al*., 2002). Therefore, during the partial meniscectomy operation, unstable meniscal fragments are removed, while the remaining meniscus is preserved and its edges are smoothed so that there are no frayed ends. The operation typically lasts for 45 minutes (Tregonning, 1983).

There are two main indications for partial rather than total meniscectomy. Firstly, the collagen network of the injured meniscus must be intact. Secondly,

the “red zone” must be intact, otherwise the native function would be lost due to the inability of the meniscus to transfer load stresses.

Total meniscectomy

Using biomechanical analysis, Wilson *et al*. (2003) found a correlation between total meniscectomy and osteoarthritic degenerative changes in underlying articular cartilage. After meniscectomy, maximal values and distribution of the shear stresses were introduced to the articular cartilage which may accelerate the degeneration of the cartilage. Therefore, total meniscectomy might only be performed when the presence of the menisci becomes an irreversible impediment to the knee’s movements or causes excessive pain to the patient.

1.1.2.5 Replacement of the meniscus

Clinical consideration

Currently, meniscal replacement is considered as a surgical option for its potential of either, forestalling the expected degenerative changes or enhancing knee stability after meniscectomy (Rodeo, 2007). However, the prognosis of this treatment can be highly unpredictable if the patient’s knee has already presented advanced degenerative changes prior to the operation (van Arkel and de Boer, 1995; Noyes *et al*., 2004). Hence, it has been recommended that meniscus replacement should be limited to those patients with at least partial cartilage thickness preserved (Rodeo, 2007). Both autografts and allografts have been widely studied for their performance as meniscal substitutes.

Meniscus autografts involve the use of a tissue from another site of the patient’s body to re-implant into their knee, to substitute the meniscus. So far, a wide range of tissues, such as semi-tendinosus and patellar tendon, have been studied for their performance as meniscus autografts. Using ovine

models, Kohn (1993) inserted the central strips of quadriceps tendon and fixed them to the tibial plateau and the surrounded capsule to substitute the medial meniscus. The 1-year follow-up results showed no complications and no cartilage changes. Kohn also investigated the possibility of using the pediculated infrapatellar fat pad as autograft and found prevalent cartilage defects at 12 months following replacement in 15 sheep (Khon *et al*., 1997). Overall, none of the autografts have exhibited mechanical properties comparable to those of the meniscus, hence they might not be an ideal choice for long-term meniscal replacements.

Allografts are transplants of tissue from one individual to another of the same species. The reported short-term outcome of allografting was promising, however, long-term outcome of this technique could be unpredictable due to the potential for immune rejection and disease transmission plus the method used for attachment/fixation and individual differences between biomechanical factors of the knee joint (Verdonk *et al*., 2008). van Arkel and de Boer (1995) argued that misalignment of the knee joints would result in failure of meniscal allografts. At present, cryopreserved allografts have been considered the most successful. A mid-term study by Rath *et al*. (2001) showed encouraging Short Form-36 clinical evaluation results, in that patients' physical functions, social functions and pain were all significantly improved at an average of 5.4 years, after cryopreserved allograft transplantation. Most patients showed reduced symptoms without significant decrease in the joint space.

Tissue engineering of meniscal substitutes

Tissue engineering has the potential to play an important role in many areas of Orthopaedics including meniscus substitution. In the context of meniscal injuries, tissue engineering involves the design and production of meniscus substitutes that can either sustain (as scaffolds) or totally replace the injured meniscus.

Many factors should be considered in the selection or synthesis of a meniscus substitute material, and some of these factors are given below. The material should be biocompatible. It can be shaped into the geometry of the normal meniscus. The substitute needs to have similar biomechanical properties to that of the normal meniscus. It would be advantageous if the material was permeable to macromolecules for nutrition. Finally, the substitute must be free from disease transmission (Messner, 1994; Buma *et al*., 2004). So far, both natural and artificial materials have been studied *in vivo* and *in vitro* for their capability of acting as meniscal substitutes, and some of these are discussed in the following sections.

Porcine small intestinal submucosa scaffolds

The porcine small intestinal submucosa (SIS), which is extracted from the porcine small intestine, has been tested as a meniscal scaffold. After a series of treatments, to lyse and solubilise the cells, the ECM of SIS was preserved and used as a scaffold for meniscal repair. It was shown that the porcine SIS ECM was comprised of collagen (types I, III, IV, and VI), glycosaminoglycans, fibroblast growth factor, and transforming growth factor that may contribute to structural, chemotactic, mitogenic, and stimulatory effects on cells and matrix (Cook *et al*., 1999). Following suturing into the meniscal defect in canine models, the treated SIS was shown to be a suitable scaffold for repair of the meniscal tissue. It promoted a benign response which led to tissue reconstruction (Badylak, 2002; Badylak, 2004).

Cook *et al*. (1999; 2001; 2006) carried out a series of studies in canine models to investigate the potential of using porcine SIS grafts to regenerate damaged meniscus tissues. They found that the SIS grafts had a very limited effect in the avascular area of the meniscus. However, in the vascularised meniscal zone, the SIS was capable of inducing tissue regeneration, and the SIS grafts were eventually absorbed and replaced by the host tissue. This was consistent with the results of a study by Record *et al*. (2001). Cook also found that the reconstructed meniscus tissues showed improved

biomechanical properties in contrast to untreated meniscal defects, although they did not match those of the normal native tissues.

The main drawbacks associated with using porcine SIS include religious and ethical issues, and the risk of introducing porcine endogenous retrovirus (PERV's) (Martin *et al*., 1998; Specke *et al*., 2001).

The collagen-glycosaminoglycan meniscal implant (CMI^{TM})

The collagen-glycosaminoglycan meniscal implant (CMI^{TM}) was designed by Stone's research group in 1990. A series of relevant studies, in canine models and 10 human patients, has been published (Stone *et al*., 1990; 1992; 1997). The CMI^{TM} is so far the only artificial meniscal replacement that has been approved for clinical application in Europe. It has several advantages such as consisting of type I collagen, easy storage, non-antigenicity and easy modeling into an ideal configuration. An improvement over preoperative status and maintenance of a good status at 2 years in eight patients were reported by Steadman and Rodkey (2005). In a follow-up study of 85 patients, who were treated with the CMI^{TM} implant over an average 5-year period, Rodkey *et al*. (2008) found that CMI^{TM}-treated patients had a significantly higher survivorship from re-operation, than the untreated control group. However, others have expressed their concern about the instability of the biomechanical properties of CMI^{TM} (Martinek *et al*., 2006; Buma *et al*., 2007).

Synthetic acellular scaffolds

A wide range of materials has been tested as potential components for meniscal scaffold synthesis such as polyester, polyglycolic acid (PGA) and other polymer materials. Some non-polymer materials such as carbon fibres are under investigation.

There are advantages and disadvantages associated with these synthetic materials. On the positive side, synthetic materials can be deliberately tailor-made to have a meniscus-mimicking configuration in terms of shape, strength and porosity (Stone, 1996; Arnoczky, 1999). However, there are two major drawbacks associated with synthetic materials. Firstly, synthetic materials are likely to release friction-inducing particulate debris, which is known to cause knee joint synovitis (Rodosky *et al.*, 1990; Wood *et al.*, 1990). Secondly, biocompatibility is a hugely important consideration and to date, no eligible synthetic materials have been reported.

1.1.3 Articular cartilage

Articular cartilage (AC) is a smooth and glistening white tissue which can be found on the articulating surfaces of diarthrodial joints. Within the knee joint, the articulating surfaces of the femur, tibia and patella are all lined by a layer of AC. The unique mechanical properties of AC contribute largely to the formation of an outstanding low-friction and wear resistant articulation.

1.1.3.1 Composition and structure of articular cartilage

Articular cartilage, like the meniscus, can be considered to comprise two phases: the solid phase and the fluid phase (Mow *et al*., 1980a). In general, the composition of articular cartilage and meniscus are quite similar. Hence, the following sections will mainly focus on the known differences between these two tissues.

Chondrocytes

Chondrocytes account for less than 10% of the total cartilage volume (Mow and Huiskes, 2005). They are present widely throughout the tissue, and their shapes and sizes vary depending on the depth of their position. Chondrocytes appear to be ellipsoidal near the surface, spherical in the middle zone, while in the deep zone they form columns.

As the only cell type within articular cartilage, the chondrocytes provide fundamental and unique cellular functions. Firstly, chondrocytes synthesise the components of the extracellular matrix (ECM), such as collagen (mainly types II and IX), and proteoglycans (Nishimura *et al.*, 1989; Sandell *et al.*, 1991; Mow *et al.*, 1992). Chondrocytes also regulate the cellular functions by synthesising enzymes which can degrade the ECM proteins. The typical enzymes produced by chondrocytes are matrix metalloproteinases-1, 8, 13 (MMPs-1, 8, 13), among which the MMP-13 is the most efficient at cleaving type-II collagen and hence plays an important role in cartilage degradation (Mow and Huiskes, 2005). Chondrocytes are responsible for the assembly of macromolecules and the organisation of the ECM. Their metabolic activities maintain the homeostasis of the inner environment of the cartilage tissue (Mow *et al.*, 1992).

Due to the fact that there are no blood vessels or lymphatic vessels within cartilage, the chondrocyte must gain nutritional support through other routes, rather than the blood/lymph vessels. It has been reported that the two major nutritional supplies of the chondrocyte are the synovial fluid through diffusion mechanisms, and through direct contact with the vascularised subchondral bone (Mow *et al.*, 1992).

Cartilage extracellular matrix

Similar to the constituents of the meniscus, the ECM of articular cartilage consists of water, proteoglycan (PG), collagen, and other proteins and glycoproteins. A comparison of the percentage weight of the components of the two tissues was summarised by Mow and Hayes (1997) and is shown in Table 1.4.

Table 1.4 A comparison of the main components of the meniscus and cartilage

Component	Meniscus	Cartilage
Collagen	**Dominantly Type I, 15-25% of wet weight or 70% of dry weight**	**Dominantly Type II, 10%-30% of wet weight**
Proteoglycans	**1-2% of wet weight**	**3%-10% of wet weight**
Cells	**Fibrochondrocytes** **(<10% of tissue volume)**	**Chondrocytes** **(<10% of tissue volume)**
Water	**60%-70%**	**60%-87% of volume**

It can be seen from the table that the most significant difference between these two tissues is their proteoglycan (PGs) content, that is articular cartilage contains considerably more PGs than meniscus. This has been shown in many studies (Adam *et al*., 1981; Fithian *et al*., 1990; Hellio Le Graverand *et al*., 1999).

The significance of a higher PG content of articular cartilage compared to the meniscus, may due to their functional differences. Since cartilage is mainly responsible for resisting compressive forces, it needs more PGs to generate a sufficient osmotic swelling pressure, while the meniscus is responsible for resisting not only compressive forces, but also tensile hoop stresses, and therefore, in the peripheral parts of the meniscus there is less PG present. Pickard *et al*. (1998) investigated the effect of PG content on frictional properties by comparing the friction coefficients among healthy and degraded bovine femoral cartilage, and healthy bovine meniscus. The results showed that under high load, the meniscus increased in friction more quickly than the two cartilage groups. However, no significant difference existed between the two cartilage groups no matter what test conditions were applied, which indicated that PG content might have a limited effect on the tissue's friction coefficient.

Structures of articular cartilage

The macrostructure of articular cartilage can be depicted in a four-zone fashion, which is illustrated in Figure 1.14. As a heterogeneous tissue, normal human articular cartilage is comprised on average of 74% deep zone, 19% transitional zone, and 7% superficial zone (Changoor *et al*., 2011).

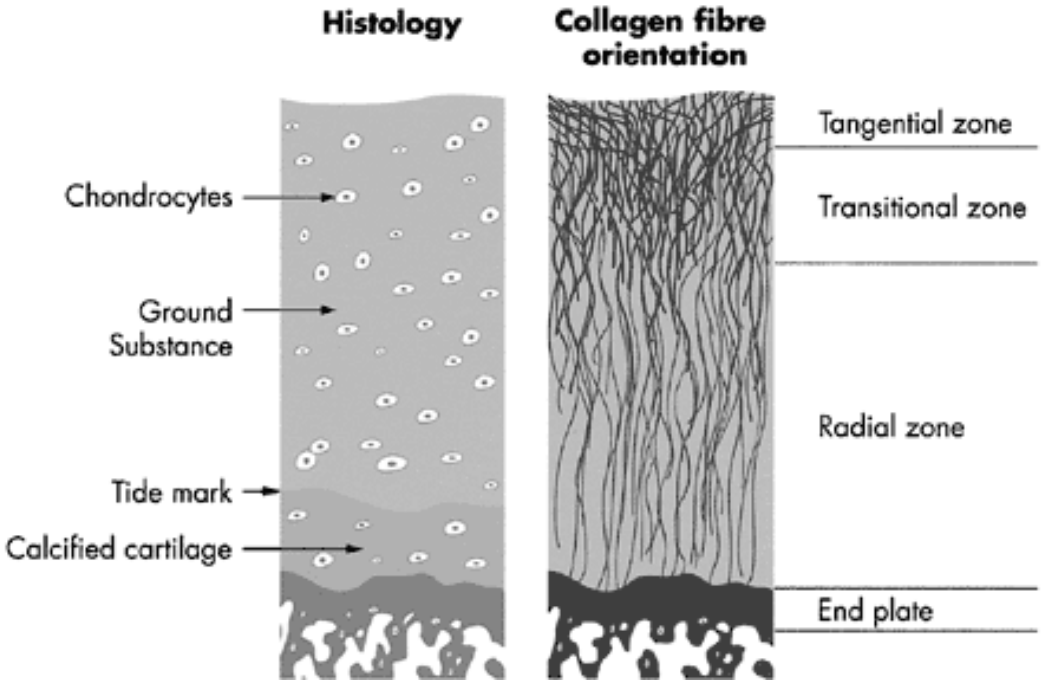

Figure 1.14 An illustration of the "four-layer" structure of articular cartilage. (Image from the website of Knee Joint Surgery, link:

http://www.kneejointsurgery.com/html/articular_cartilage/anatomy.html)

In the superficial zone of articular cartilage, also known as the tangential zone, the collagen fibrils are oriented parallel to the surface and the chondrocytes are ellipsoid in shape. The water content is at its highest, and the PG content is at its lowest. The transitional zone is inferior to the superficial zone. The collagen fibers are thicker and less organised in this zone. Below the transitional zone is the deep zone, containing large-diameter collagen fibers which are oriented perpendicular to the articular surface. Changoor *et al*. (2011) characterised the collagen network in human articular cartilage using polarised light and scanning electron microscopy. The average

diameter of collagen fibres was 108.2 nm in deep zone, 87.5 nm in transitional zone, and 55.8 nm in superficial zone. The water content is at its lowest, and the PG content is at its highest. The deepest zone of articular cartilage is the calcified zone, which is separated from the deep zone by the tidemark. The main function of this zone is to anchor the cartilage to the subchondral bone.

1.1.3.2 Biomechanics of articular cartilage

Even following exposure to high loads up to 20 times the body weight, normal articular cartilage can return to its previous shape without crushing or tearing when the load is withdrawn. This is due to the specific structure of AC which enables it to store, transmit, and dissipate mechanical energy. Upon loading, the hysteresis energy which is a part of the external energy that is absorbed by the articular cartilage, can then dissipate, for example, by heat (Nordin and Frankel, 2001).

Biomechanical properties of articular cartilage

As described in Section 1.41, the microstructure and macrostructure of articular cartilage vary throughout the depth of tissue, which makes the mechanical behavior of articular cartilage anisotropic and inhomogeneous. Considered as a biphasic material, articular cartilage has flow and deformational behaviours under a variety of conditions. The tensile and compressive properties of articular cartilage are derived from the collagen fibrils and proteoglycans, respectively. *In vitro* studies have shown that the tensile modulus of articular cartilage is correlated to the alignment of collagen fibres, while the proteoglycan content has no effect on the tensile modulus (Schmidt, 1990; Mow and Ateshian, 1997). Tensile strength is always higher in the direction parallel to the collagen fibres than in the perpendicular direction. Mow *et al*. (1992) tested the tensile properties of cartilage in a constant low strain-rate condition, and a resultant tensile-strain curve showed a typical toe region and a linear region which indicated a strain-correlated

stiffness (Figure 1.15). Failure occurs when the collagen fibres are stretched to rupture.

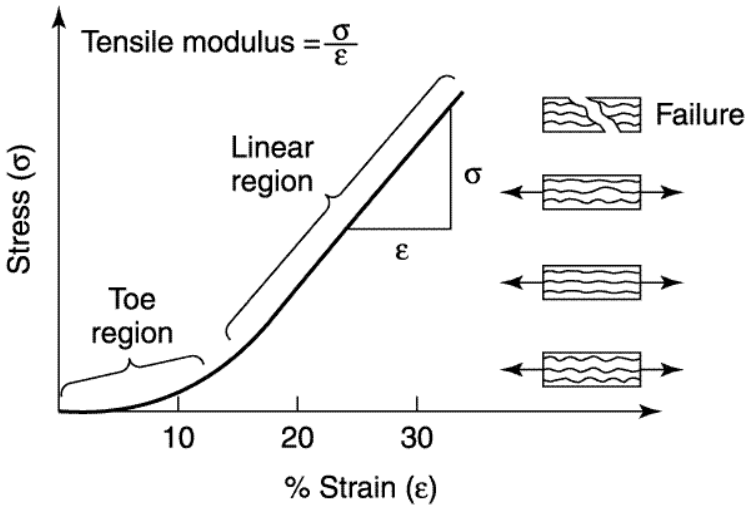

Figure 1.15 A tensile-strain curve of cartilage. The toe region is assigned to the strengthening of the coiled collagen fibres under tension. The linear region shows that more collagen fibres will be involved to resist tension when the latter is constantly increasing (Mow *et al*., 1992).

The compressive properties of articular cartilage tissues are directly correlated with its proteoglycan content, and inversely correlated with its interstitial water content (Armstrong and Mow, 1982; Armstrong and Mow, 1983). The compressive modulus of articular cartilage is between 0.1 to 1 MPa (Ateshian *et al*., 2003). In addition, articular cartilage has well-defined shear and viscoelastic properties. The shear properties of cartilage are derived from the collagen network and the energy storage capacity. The basic mechanism is that the shear stiffness of cartilage allows the solid phase to deform while it retains the fluid phase in position when under a torsional stress (Mow *et al*., 1989).

The viscoelastic properties of cartilage tissue are derived from the interactions between the fluid and solid phases, as well as from the interactions between matrix components within the solid phase (Setton *et al*., 1993; DiSilvestro *et al.*, 2002). Since the solid matrix of cartilage is highly porous (porosity in the range of 0.75-0.8) with a small pore size (in the range of 2.0-6.5 nm), it is

permeable and allows the interstitial fluid which resides in the microscopic pores to flow when loads are applied (Dowson, 1990). The ability of solid matrices to induce fluid flow can be presented as the coefficient of hydraulic permeability, while the ability to resist flow can be described by diffusive drag coefficient. The latter is mainly responsible for cartilage's viscoelastic behaviour (Mow *et al*., 1980a). Because the cartilage tissue permeability is very low (10^{-15} to 10^{-16} m^4/Ns), consequently a very large drag force will be induced when a compressive stress is applied (Lai *et al*., 1980). Within the cartilage, the rate of the fluid flow varies at different stages after a load or stress is initially applied. In brief, the flow always starts at a high rate, and then gradually slows down, until a state of no flow is reached.

Stress-relaxation behavior

As the consequence of viscoelastic nature, the stress-relaxation behavior of cartilage tissue has been observed in confined compression tests (Figure 1.16).

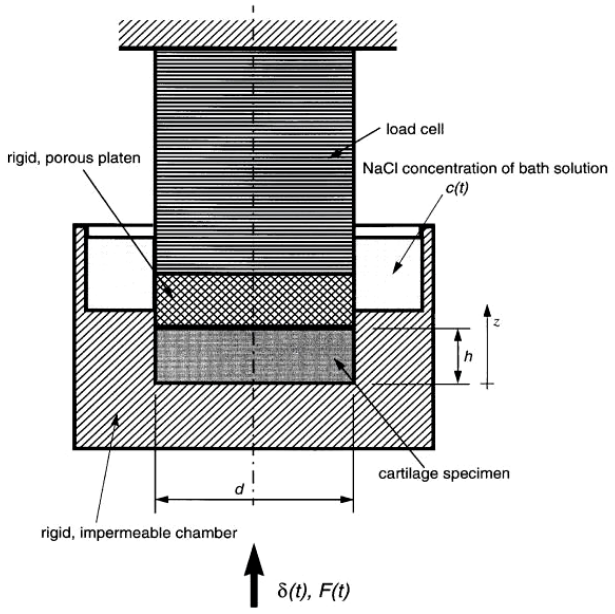

Figure 1.16 Schematic of a confined compression test (Eisenberg and Grodzinsky, 1987).

A cylindrical cartilage specimen was compressed by a rigid porous plate in a rigid impermeable chamber. Fluid exudation and exchange with the bath solution could only occur through the porous plate across the surface of the cartilage specimen. The stress and fluid re-distribution in cartilage tissue while under a confined compression test is shown in Figure 1.17 (Mow *et al*., 2005).

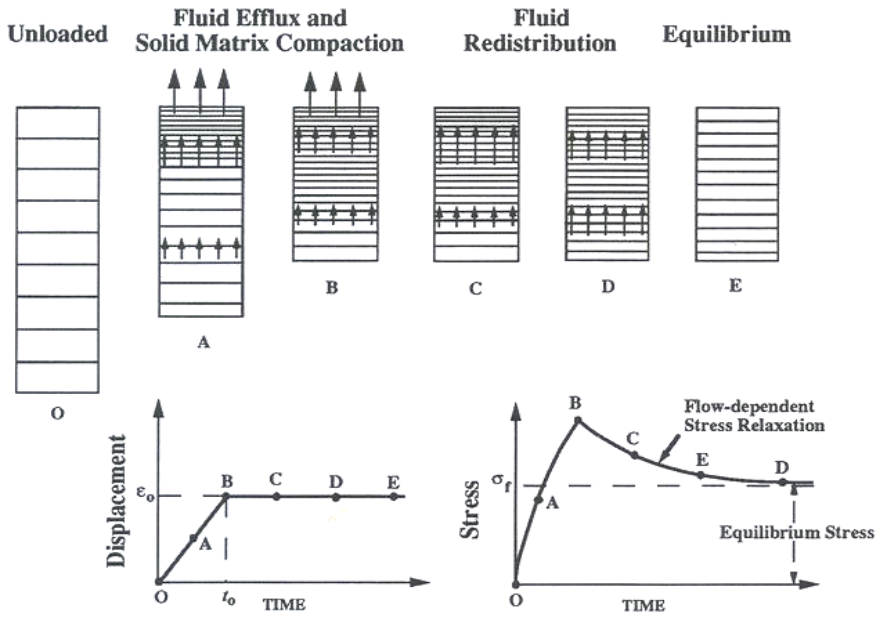

Figure 1.17 Stress-relaxation test of cartilage tissue in confined compression. Applied displacement and stress-relaxation response show that stress increases with the displacement level (time points 0-A-B), and it will then relax due to the stress relief at the solid matrix surface (B-C-D-E), resulting re-distribution of fluid and hence the corresponding hydrostatic pressure (Mow *et al*., 2005).

Compressive creep behavior

Compressive creep deformation of cartilage occurs when fluid exudes from the tissue (Mow *et al*., 1980a; Lai *et al*., 1981; Mow *et al*., 1989). The rate of fluid exudation is high initially, hence the rate of deformation is high at the beginning, and then it decreases gradually as the flow ceases (Figure 1.18).

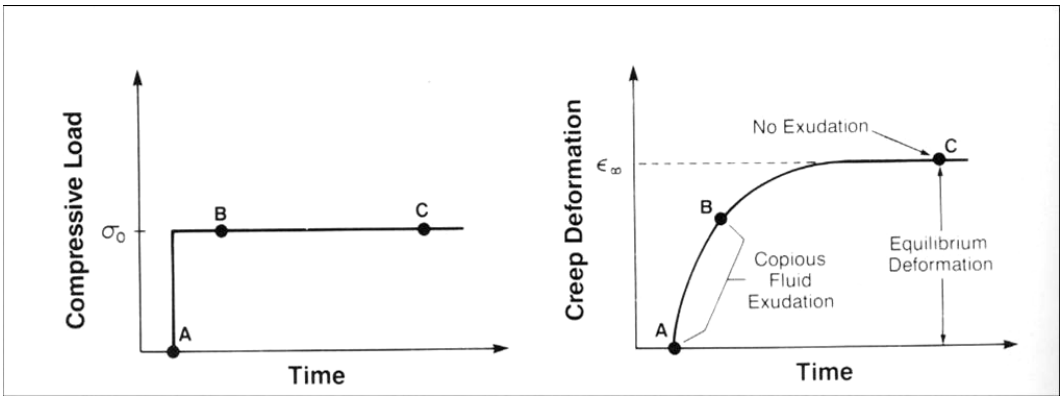

Figure 1.18 Creep response of cartilage under a constant compression (Mow *et al*.,1980a)

Therefore, the biomechanical properties of cartilage are in fact time-dependent. Moreover, since this viscous dissipation is highly related to the degree of hydration of the tissue, any diseases which cause changes in the water content, will affect the intrinsic properties of articular cartilage, an example is osteoarthritis. (Setton *et al*., 1993; Nordin and Frankel, 2001).

Frictional properties of articular cartilage

Numerous studies have investigated the frictional properties of articular cartilage, either using simple pin-on-plate or sphere-on-disc geometries (Freeman *et al*., 2000; Park *et al*., 2003; Bell *et al*., 2006; Katta *et al*., 2007; Northwood *et al*., 2007; Katta *et al*., 2008), or using anatomical joint simulation (McCann *et al*., 2008).

During daily motion, two types of friction can be seen in the articular cartilage. The first type is surface friction. In normal knee cartilage, this friction is mainly from the sheared lubricant film between the two articulating surfaces. However, on some occasions, it can also come from the direct contact of the two surfaces. The second type is called internal friction or bulk friction. For cartilage, the internal friction comes from the frictional diffusive drag, which has been discussed in the previous section (Mow *et al.*, 1984). The *in vitro* coefficient of friction (COF) of the surface of the normal knee AC is either

between 0.005 to 0.02 (Charnley, 1960), or between 0.01 to 0.056 (McCann *et al*., 2008), which is considerably lower than the friction coefficient found between many artificial and natural materials. For example, the COF of a glass-on-glass articulation is around 0.9, while the COF of a steel-on-steel articulation is 0.6 to 0.8 (Dowson, 1981). Articular cartilage has unique and exceptional frictional properties which contribute to the long-term, low friction and low wear performance of the synovial joints. It should be noted that the COF of AC-on-AC will increase with the age of an individual, and this has been suggested to be associated with the age-related depletion of GAG content in the cartilage (Thompson and Oegema, 1979; Katta *et al*., 2008b).

Synovial fluid

It should be noted that the amazing low friction performance of articular cartilage does not only result from the frictional properties, but the synovial fluid within the joint capsule also plays an important role.

Synovial fluid is a transparent, mucous liquid which is secreted by the synovium. It is a dialysate of blood plasma that is void of clotting factors such as fibrinogen, erythrocytes, or hemoglobin. A healthy human knee joint contains approximately 1 to 5 ml synovial fluid (Jay *et al.*, 1998; Katta *et al.*, 2008a). Studies carried out *in vitro* in the 1970s demonstrated that synovial fluid lubrication can significantly reduce the friction coefficient and wear of articulating cartilage surfaces (Simon 1971; Lipshitz *et al.*, 1975).

Studies of the contribution of the components of synovial fluid to its lubrication properties revealed that various components were responsible for the lubrication properties provided by synovial fluid. An extended glycosaminoglycan chain which is called hyaluronate, contributes to the viscosity of synovial fluid, while a lubricating glycoprotein called lubricin, has been shown to affect friction during joint articulation, when this glycoprotein is absorbed onto the articular cartilage surface (Swann *et al*., 1981; 1985;

Zappone *et al.*, 2008). Synovial fluid also contains phospholipids which are reported to be responsible for retarding wear (Katta *et al*., 2008a).

Even though there is still a debate over the effectiveness of hyaluronic acid in boundary lubrication, recent studies by Bell *et al*. (2006) and Forsey *et al*. (2006), have shown that hyaluronic acid provided a lower friction coefficient compared to other solutions such as Ringers solution. Since it is not fully understood which components are responsible for most of the lubricating properties and in what proportions they act, more relevant studies are needed.

1.1.3.3 Cartilage lubrication

The mechanism of the lubrication of human joints is very complicated but highly efficient. A healthy synovial joint can bear high loads and perform a wide-range of movement for seventy or eighty years, with a combination of almost all kinds of lubrication modes in engineering such as fluid film lubrication, boundary lubrication, and mostly importantly the biphasic lubrication**.**

Fluid film lubrication

In 1932, MacConail proposed the concept of hydrodynamic lubrication to describe a lubrication regime in which two loaded articulating surfaces are completely separated by a thin film of lubrication fluid without direct contact (MacConail, 1932). This hypothesis was then developed into the concept of fluid film lubrication which has been widely upheld. To date, many regimes have been developed to describe the fluid film lubrication in the context of joint articulation. In 1986, Dowson and Jin developed the micro-elasto-hydrodynamic lubrication regime, describing that, due to the elastic nature of the contacting cartilage surfaces, surface asperities were smoothed at a macro-level during articulation, allowing the maintenance of the fluid film

(Dowson and Jin, 1986). If the lubricant is viscous in nature and cannot be squeezed out of the contact area instantaneously after loading, squeeze film lubrication may operate so that the fluid pressure can maintain the separation of two articulating surfaces (Mow and Ateshian, 1997). In fact, fluid film lubrication can be seen in all synovial joints, with the synovial fluid behaving as the fluid lubricant. Due to the fact that the two surfaces do not abrade each other, very low friction and low wear can be achieved.

Boundary lubrication

When the combined roughness of the opposing bearing exceeds the thickness of the fluid film, surface load is supported by surface-to-surface contact at their asperities (Wright and Dowson, 1976). However, the articulating surfaces of the joint are adsorbed by a monolayer or multilayer of lubricant which prevents direct contact between the two surfaces and hence minimises the friction between them. This is boundary lubrication. The lubricants that have been proposed to be responsible for boundary lubrication in cartilage include synovial fluid components such as hyaluronic acid and lubricin (Section 4.2.3), and surface amorphous phospholipids. Three saturated phospholipids, dipalmitoyl phosphotidylcholine (DPPC), phosphatidylethanolamine and sphingomyelin, and also the unsaturated phosphatidylcholines have been identified that may be acting as boundary lubricants for articular cartilage (Sarma *et al*. 2001; Chen *et al*. 2007).

The most superficial layer of articular cartilage known as the lamina splendens is acellular and measures 4 to 8 microns in thickness and consists of collagen. Under boundary lubrication conditions, this thin layer is responsible for reducing friction. Jay (1992) summarised the two functional molecular domains of the boundary lubricants, which are surface-binding and repulsive force-generating. For articular cartilage, the main repulsive force between the two articulating surfaces may derive from the so-called “repulsive hydration force” which is thought to be the only repulsive force capable of withstanding the pressures of normal joint function (Israelachvili, 1985).

Mixed lubrication

When the lubrication film breaks down due to extreme loading or intermittent motions, boundary lubrication becomes functional to minimise friction and wear of the contacting surfaces.

The three aforementioned distinct lubrication regimes also exist in engineering bearings, an illustration is given in Figure 1.19. However, the extraordinary lubrication mechanisms of articular cartilage cannot be matched by engineering methods, and this led to the proposal that two very distinct mechanisms also operate, weeping lubrication and biphasic lubrication.

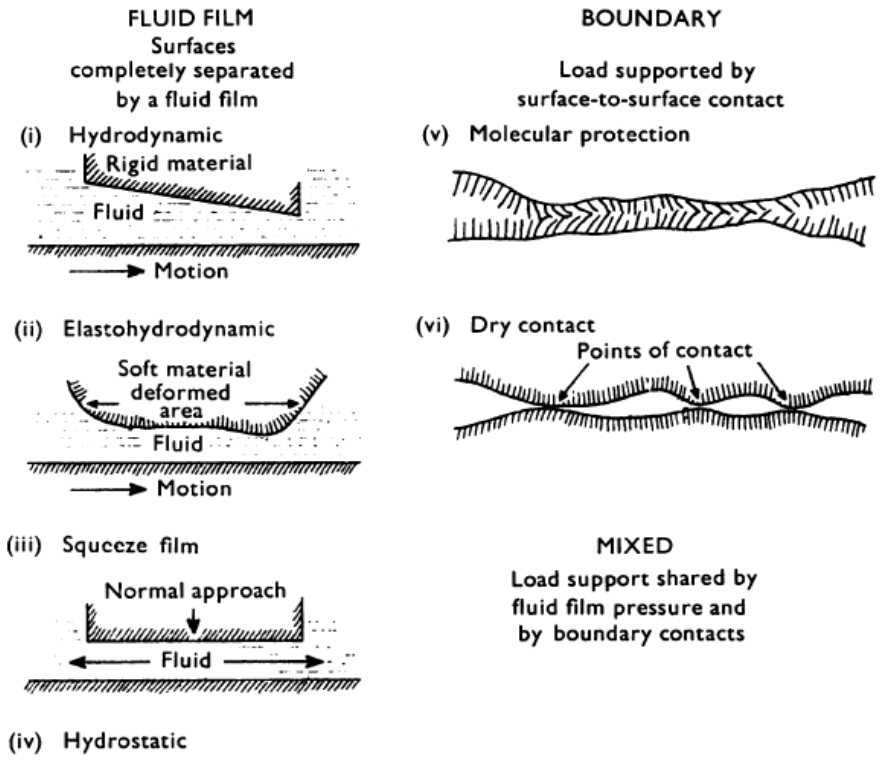

Figure 1.19 An illustration of the three major engineering lubrication mechanisms (Wright and Dowson, 1976).

Biphasic lubrication

Lewis and McCutchen (1959) postulated the term “weeping lubrication”, which was later modified into “self-pressurised hydrostatic lubrication mechanism” by McCutchen, to describe the flow of interstitial water out of cartilage to lubricate the articulating surface when under loading. However, several questions cannot be properly answered by this weeping lubrication, for example, why does the water flow into the contact surface rather than flowing away. Therefore, the weeping lubrication theory has been replaced by the biphasic lubrication mechanism.

Originating from the self-pressurised hydrostatic lubrication mechanism proposed by McCutchen (1959) and the biphasic theory proposed by Mow *et al*. (1980a), the term “biphasic lubrication” was coined by Forster and Fisher (1996), who reported that the effective coefficient of friction between cartilage and cartilage was maintained at a very low level as long as the fluid phase of the cartilage carried a high level of load. Unlike fluid film, boundary, and mixed lubrication, biphasic lubrication is a regime which describes the lubrication mechanisms at a microstructural level that is concerned with the inherent structure of articular cartilage. As discussed in Section 1.1.3.1, the ECM of articular cartilage consists of two phases: fluid phase and solid phase based on the biphasic theory. When load is applied, the fluid tends to be exuded through the ECM and generates interstitial fluid pressurisation, which can reduce the loads that the solid phase is exposed to. Because the friction between the cartilage surfaces mainly results from the interactions of their solid phases, the interstitial fluid pressurisation can minimise the friction and wear of the bearing surfaces until the fluid is completely extruded out of the contact region, after which the load will be transferred into the solid phase of the articular cartilage.

1.1.4 Cartilage wear and degradation

Wear is the removal of material from a surface and is caused by the mechanical action between two surfaces in contact. There can be two different types of mechanical wear experienced in articular cartilage, which are termed as interfacial wear and fatigue wear, respectively.

Interfacial wear

Interfacial wear of articular cartilage results from the direct contact and friction of the two load-bearing surfaces, especially when they are undergoing degeneration or impairment. As discussed in Section 1.1.3.2, it is the hydraulic permeability and diffusive drag of the solid phase which determines the fluid flow inside the cartilage. Hence, if the normal ultrastructure was changed or damaged , articular cartilage would become more permeable and the fluid from the lubricant film would easily leak through the cartilage surface, thereby increasing the probability of direct contact between asperities.

Changes to the normal articulating surface may also break down the boundary repellent mechanism and result in tissue adherence. Consequently, a tear could occur after repeated sliding between the two surfaces, and this is termed as adhesive wear. In some cases, an over-accumulation of wear debris due to degeneration can scrape the articulating surface, and cause another form of wear which has been termed as abrasive wear (Dowson and Wright, 1981).

Fatigue wear

Fatigue wear is independent of the lubrication phenomenon and of the contacting area (Mow and Huiskes, 2005). It occurs when the microscopic damage within the cartilage accumulates to a severe extent. This microscopic damage is caused by cyclic stresses and strains that are generated within the cartilage, and either the tensile faliure of the collagen network, or the decreased stiffness and increased tissue permeability due to PG loss, or the

failure of stress-relief due to insufficient fluid redistribution resulting in fatigue wear (Broom, 1986).

Cartilage degeneration

Wear is the most common appearance of the degenerated articular cartilage. Many factors such as collagen-proteoglycan matrix changes are associated with this progressive failure of cartilage tissue. Normally, aging is the main cause of degeneration. With increasing age, adult cartilage can show loosening of the collagen network and loss of PGs, and eventually the biomechanical properties of articular cartilage start to become impaired. At the nanometer level, studies of the surface topography have shown that the collagen fibrils in degenerated cartilage combine with each other into larger bundles which orientate in certain direction. This could be the result of loss of GAGs which make the directed movement of collagen fibrils more easy (Imer *et al*., 2009).

There are several conditions under which the pace of degeneration would be accelerated. For example, high contact pressures between the articular surfaces over a long eriod of time can reduce the probability of fluid film lubrication, allow for continued tissue damage, and also increase the risk of early degenerative arthritis. Pathological causes such as osteoarthritis can also lead to degeneration of articular cartilage (Zazirnyi, 1999). Even though the understanding of pathological loss of cartilage is still limited, matrix metalloproteinases (MMPs) are now recognised to be involved in the degeneration process of cartilage, and many relevant MMP inhibitors such as the antibiotic doxycycline are under clinical trial to prevent the degeneration process of cartilage (Cawston and Wilson, 2006; Burrage and Brinckerhoff, 2007).

Differences between the tibial and femoral cartilage

A study by Colombo *et al*. (1983) showed a significant difference in the incidence and severity of the lesions between tibial and femoral cartilage, 12 weeks post-meniscectomy. This might be explained by the knee joint geometry. As shown in Figure 1.3, the femoral condyles will change position during flexion and extension of the knee, hence the contact areas shift over the time. In contrast, the tibial cartilage has a relatively fixed contact region to bear load (Weidow *et al*., 2002; Yildirim *et al*., 2007). Weidow *et al*. (2002) studied the morphological changes associated with cartilage wear on the resected parts of human knee joints, and produced a grading map of cartilage destruction and bone attrition on both the tibial and femoral surfaces (Figure 1.20). However, it is still worthwhile to investigate the mechanisms which lead to the differences between the two cartilages, especially when under the same loading and friction conditions.

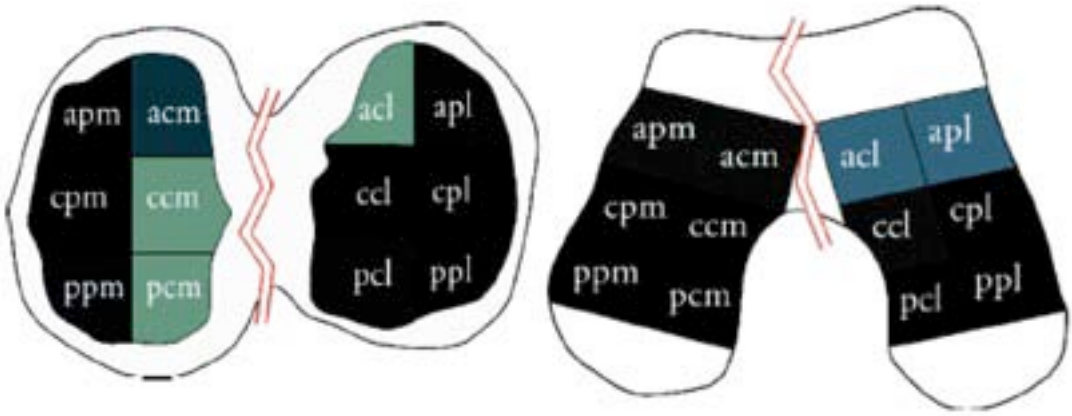

Figure 1.20 Grading maps of the severity of cartilage destruction on (a) tibial plateau surface; and (b) femoral condyle surface. The darker the area, the more severe cartilage wear has been observed. *apm*: anterior-peripheral-medial; *cpm*: central-peripheral-medial; *ppm*: posterior-peripheral-medial; *acm*: anterior-central-medial; *ccm*: central-central-medial; *pcm*: posterior-central-medial; *acl*: anterior-central-lateral; *apl*: anterior-peripheral-lateral, *etc*.. (Weidow *et al*., 2002)

1.2 MRI of the Knee

Nuclear magnetic resonance (NMR) technology derives from the pioneering work of Bloch *et al*. (1946) and Purcell *et al*. (1946). In the early 1970s, magnetic resonance imaging (MRI) was reported for the first time (Lauterbur, 1973). The basic physical principle of MRI is to acquire images of radiofrequency (RF) pulse-excited hydrogen atomic nuclei in a powerful magnetic field. The brightness and darkness shown on MR images are relative to the spatially localised signal intensities, which depend on several indices such as NMR tissue characteristics and the proton density of the tissue. With the advance of MRI technology, new techniques such as ultra-high field MRI and open-access “real-time” interventional MRI (Figure 1.21) have emerged and been applied in a wide range of clinical and scientific research. The diagnostic performance of MRI in knee disease such as OA has been shown to be promising (Menashe *et al*., 2012).

Figure 1.21 The GE 0.5 Tesla Open-access interventional MRI scanner with a 56 cm gap between magnets (Williams and Logan, 2004).

1.2.1 MRI of the meniscus

Magnetic Resonance Imaging (MRI) has been performed to evaluate the knee meniscus since the 1980s. Reicher *et al*. (1985) reported a high correlation of

MRI and arthroscopic findings in 10 of 11 patients of clinically suspected meniscal tears. Forty-nine patients underwent 0.3 Tesla MRI in a study by Reicher *et al*. (1986), and results showed the capability of MRI in depiction of meniscal tears and implied the potential of MRI to be used as a preoperative evaluation tool. Lotysch *et al*. (1986) performed 1.5 Tesla MR imaging on 88 knees of patients with suspected meniscal injuries. For the first time, the authors studied the internal signal of menisci and found no consistent correlation between intrameniscal signal and meniscal injury. They also developed a grading system to improve the specificity of MRI in the diagnostics of meniscal lesions. This diagnostic system was proved useful (Stoller *et al*., 1987) and was further improved by Crues *et al*. (1987). Noto *et al*. (1986) surgically produced vertical and horizontal meniscal tears on immature porcine knees and demonstrated the surgically generated lesions on 1.5-Tesla MR images.

As one of the most sophisticated medical imaging techniques, MRI became more and more important in clinical diagnostics of various knee meniscal variants (*e.g*., discoid meniscus) (Ryu *et al*., 1998) and lesions such as meniscal extrusion (Costa *et al*., 2004), tears (De Smet *et al*., 1993), cysts (Campbell *et al*., 2001) and meniscocapsular separation (De Maeseneer *et al*., 2002). Before and after meniscal surgery, MRI is also the most common examination to evaluate menisci (Ciliz *et al*., 2008; Wasser *et al*., 2011). The normal meniscus has low signal on all MR imaging sequences during routine clinical MR imaging. The criteria of diagnosing a meniscal tear on MR images is either abnormally high signal within the meniscus on at least one image that extends to the articular surface, or abnormal meniscal morphology (De Smet *et al*., 1993).

Not only does MRI serve as a powerful diagnostic tool, it has also been used in anatomical studies in establishment of standard diameters, morphology and movement of the knee meniscus. Stone, *et al*. (1994) measured the volume of 33 menisci from cadaver knees using MRI, and re-measured the menisci

using a water volume displacement method after excision. The results showed that MRI was precise and repeatable but not accurate in the *in vivo* measurement of meniscal volume. Erbagci, *et al*. (2004) performed 174 MRI scans using a 1 Tesla scanner, and reported data on normal human meniscal dimensions measured from MRI. Vedi, *et al*. (1999) did the first study in vivo of meniscal movement in normal knees using an open MR scanner. They reported the significant changes in meniscal movement and vertical height between loading and non-loading condition. Several studies using either low field MR scanners (0.18-0.5 Tesla) or high field MR imaging system (3 Tesla) have also reported significant changes in meniscal shape and signal intensity under weight-bearing condition (Boxheimer *et al*., 2004; Mastrokalos *et al*., 2005; Tienen *et al*., 2005; Stehling *et al*., 2011).

MRI has also proved its value away from the conventional diagnostic radiology setting. It has provided a tool for non-invasive quantitative characterisation of the meniscal tissue. Tsai, *et al*. (2009) measured the MR spin-spin relaxation time T2 value in the healthy knee menisci, aimed to enable assessment of biomechanical changes and degradation of menisci in terms of MR T2 value changes in future. Bolbos, *et al*. (2009) assessed the reproducibility of the measurements of $T1\rho$ relaxation time in the meniscus and its adjacent cartilage with acute anterior cruciate ligament (ACL) injuries at 3.0T MRI. $T1\rho$ mapping techniques allow quantitative evaluation of meniscal matrix in patients with ACL injuries. The authors found that the T1p values in meniscus are lower than those of the articular cartilage.

General MR imaging protocols employ an Echo Time (TE) of between 9 to 20 ms. Using this range of TE, the normal knee meniscus appears homogeneously dark, in other words, there is a very low or no signal in the image, irrespective of the pulse sequences being used. This is due to the fact that meniscus tissue has a very short T_2 relaxation time, which means that the meniscal signal completely decays before the signal acquisition. To highlight

the meniscus, a technique called Ultra-short TE (UTE) can be used, typically employing a TE of between 0.08 to 0.2 ms, which is capable of demonstrating the menisci with a much brighter signal (Gatehouse *et al.*, 2004). Omoumi, *et al*. (2010) optimised imaging sequences such as T2 SE and Ultra-short TE with fat saturation in a series of 3.0T MRI scans of cadaveric human menisci, and concluded that the optimal TE for visualisation of the meniscal infrastructure ranged from 3 to 6 ms.

To date, ultra-high-field (UHF, ≥ 7 Tesla) MRI of the knee has been increasingly attracting scientific interest, in both the research domain using laboratory systems and the clinical application using whole-body systems. Some pioneer studies of *in vivo* ultra-high-field MRI of musculoskeletal system have shown the advantages of using higher magnetic field strength: higher intrinsic signal to noise ratio (SNR), higher spatial resolution, higher contrast between tissues (Pakin *et al*., 2006; Regatte *et al*., 2007). Robinson, *et al*. (1988) performed 4.7 Tesla MRI on porcine knees to acquire high resolution MR image of separate knee joint components. The results showed the potential of using UHF MRI to investigate the structures of excised knee menisci and cartilage. However, the *in vivo* UHF MRI of human subjects has its limitations. Increase in the field strength up to UHF level would also increase risk of radio frequency burns in the patient. Currently, the highest static magnetic field strength approved by The Food and Drug Administration (FDA) is up to 8T for applications in human adults (http://www.fda.gov/cdrh/d861.html).

Clinically an intrameniscal high signal could be treated as tear, mucoid degeneration, or vascularity (Aichroth *et al*., 1992; Takeda *et al*., 1998). It can be of significant value to develop methods that can investigate the internal structure of meniscus, and hence can differentiate abnormalities from normal structure and characterise meniscal lesions. In addition, in the field of biological and medical engineering, an understanding of the biomechanical and tribological properties of the knee meniscus and cartilage (*e.g*., contact

stress and friction of the articulating surfaces) and their correlation with tissue degeneration and degradation such as wear and tear are important in research and development of therapies for knee diseases.

To detect and characterise meniscal lesions, and to investigate tissue structural changes as a consequence of mechanical or tribological experiments, a non- invasive and high-resolution imaging technique is needed. However, to date, only a couple of research publications addressed the issue of high-resolution MRI mapping of intrameniscal structure (Wang *et al*., 2010; Omoumi *et al*., 2010).

1.2.2 MRI of the articular cartilage

Cartilage MRI has been widely studied for decades as a promising imaging modality to diagnose osteoarthritis (OA) and other diseases. Clinical scoring systems, such as WORMS (whole-organ MRI scoring system), which are based on MRI has also been established to assist diagnosis (Disler *et al*., 1996; Peterfy *et al*., 2004; Crema *et al*., 2011). Cartilage MRI studies involve various aspects of the tissue, from component distribution to biomarkers of disease/degeneration and morphological quantification of tissue changes.

Fragonas *et al*. (1998) studied the correlation between biochemical composition and MRI appearance of articular cartilage with and without loading, and found that MR appearance correlated with collagen content of cartilage. Keenan *et al*. (2011) used 3.0T MRI to study the sGAG content in human cartilage by age, and found that sGAG content decreased significantly with age by a combination of measurement of cartilage T2 and $T1\rho$ relaxation time. Mosher *et al*. (2010) carried out a post-activity MRI study and reported a measurable decrease in T2 value and thickness of knee cartilage after running. As one of the newly emerging MRI techniques, sodium MRI of cartilage showed good feasibility and reproducibility in determination of changes in fixed charge density (FCD) as a result of proteoglycan (PG) loss (Shapiro *et al*., 2002; Wheaton *et al*., 2004; Newbould *et al*. 2012). Stahl *et al*. (2007) conducted a follow-up study of MRI-derived parameters such as T2

relaxation time and cartilage thickness of tibio-femoral joint in patients with OA. By comparison with subjects without OA, they suggested that changes in T2 relaxation time and morphology of cartilage might be useful as an indication of early OA.

Laboratory MRI has also been extensively studied in characterisation of cartilage properties. Nugent *et al*. (2010) characterised ex vivo-generated bovine and human cartilage using MRI and other methodologies, and demonstrated the ability of MRI to investigate the maturation of cartilage tissue at any point of development. Lin *et al*. (2011) and Reiter *et al*. (2012) studied bovine cartilage samples at 9.4 Tesla and analysed MR parameters T1, T2, magnetization transfer (MT) ratio and magnetization transfer rate (k_m) using novel mathematical approaches. The results of these studies showed good sensitivity of MR-based biochemical tissue characterisation, thus demonstrating MRI to be a promising tool for non-destructive evaluation of natural or engineered cartilage tissue.

1.3 Project Aims and Objectives

Rationale

The knee is one of the most vulnerable joints to both trauma and the development of degenerative lesions. Damage to the meniscus and articular cartilage in the knee joint, either through trauma or degenerative processes, can lead to loss of function. This may compromise the tribological function and stability of the joint. This has led to the development of in vitro models to investigate the biomechanics and tribological response of cartilage and meniscal tissues. In high-volume laboratory studies of cartilage tribology, it is important to measure cartilage loss after experiments. In order to understand the relationship between the structure and function of the meniscus in health and disease, it is essential to interrogate the internal structural components of the meniscus, in addition to its gross morphology.

A new approach for non-destructive investigation, morphological observation and quantification of damage in cartilage and meniscal tissues is required. Advances in MRI technology may provide this solution, particularly ultra high field and high field MRI scanners which have already been used in recent in vitro studies of cartilage.

Aims and Objectives

The aims of this project were to optimise protocols for MRI of menisci and articular cartilage in the knee in order to gain an increased understanding of their structure, and to detect and quantify morphological changes.

The major objectives of this study are listed as below.

1. To develop a porcine medial knee joint model for friction simulator testing.
2. To create cartilage damage/wear models for MRI study.
3. To develop imaging protocols on a 9.4 Tesla and 3.0 Tesla MRI systems to study knee meniscus architecture and to quantify cartilage defects.
4. To interpret meniscal MRI findings by comparison with histological staining.
5. To develop MRI 2D-profile and 3D-surface methods for cartilage wear quantification, and to compare and validate these two methods at both 9.4 Tesla and 3.0 Tesla MRI.

Chapter 2 General Materials and Methodologies

This chapter describes the general materials, equipment, and experimental techniques commonly used throughout this PhD thesis work.

2.1 Materials and Instruments

2.1.1 Phosphate buffered saline

Phosphate buffered saline (PBS) was used for hydration, rinsing and storage of the specimens because it is isotonic and non-toxic to cells. PBS was prepared by dissolving ten PBS tablets purchased from MP Biomedicals (UK) in one litre distilled water. The constituents of the PBS tablets are shown in Table 2.1.

Table 2.1 Formulation of PBS tablets (by MP Biomedicals)

Component **Inorganic Salts**	**mg/litre**	**Mol. Wt.**	**Mol. (mM)**
Potassium Chloride [KCl]	200.00	74.55	2.68
Potassium Phosphate Monobasic [KH_2PO_4]	200.00	136.09	1.47
Sodium Chloride [NaCl]	8000.00	58.44	136.89
Sodium Phosphate Dibasic [Na_2HPO_4]	1150.00	141.96	8.10

2.1.2 PMMA bone cement

Polymethyl methacrylate (PMMA) bone cement, from Acrylic Dentrue Materials, was used for fixing cartilage-bone specimens in jigs for the friction simulator. It was purchased from WHW Plastics (Hull, UK) in the form of a powder (Cold Cure) and a liquid monomer (Rapid Repair Liquid), which were prepared as per the manufacturer's instructions, with a powder to liquid ratio of 2:1. The mixing and curing of the cement was carried out in a fume cupboard.

2.1.3 Serum

A 25% (v/v) calf serum PBS solution was used as the lubricant when running the friction simulator tests due to its similar protein concentration (16-18 mg/ml) to normal synovial fluid (approximately 20 mg/ml) (Wang *et al*., 1998). Newborn calf serum was purchased from Harlan Bioproducts for Science (Catalogue number BT-9501-500), and the PBS solution was prepared as described in section 2.1.1.

2.1.4 Dissection instruments

A size 4 scalpel handle, single-use scalpel blades, dissecting scissors, scissor punches, standard forceps and clamps were used for cutting soft tissues. A specially made clamp set was used to mount and fix the porcine femur and tibia as shown in Figure 2.1. A hacksaw was used to cut the bony component of the porcine knee.

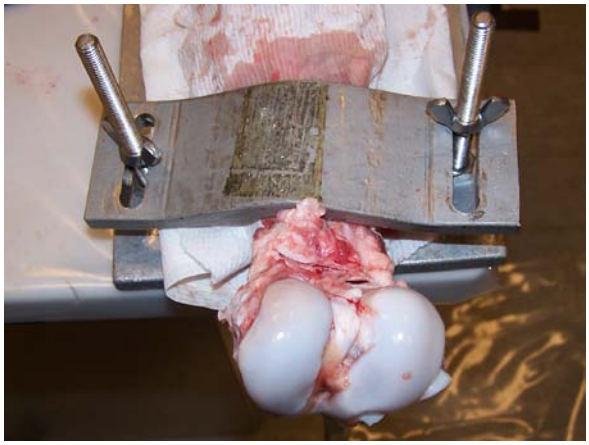

Figure 2.1 Photo of the specially made clamp set for mounting and fixing the porcine femur or tibia during the cutting of bony components.

2.2 Harvesting of animal specimens

The animal tissue specimens used throughout this study were harvested from freshly dissected porcine legs (Figure 2.2). The porcine legs were obtained from healthy Large White pigs (approximately 6 months old) from a local

abattoir (J.P. Penny's, Rawdon, Leeds) between 24 to 48 hours after slaughter. The average weight of the pigs was approximately 80 kg.

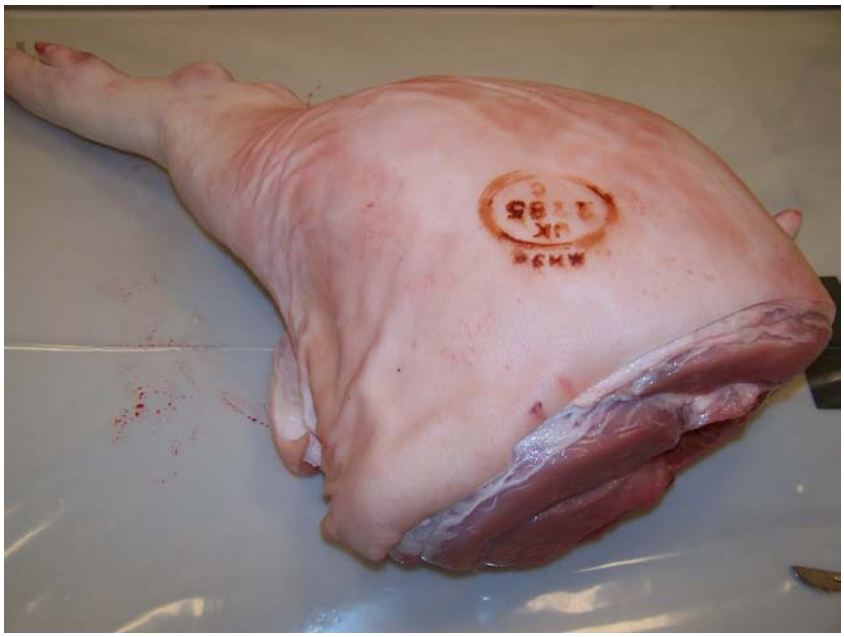

Figure 2.2 Photo of a porcine leg delivered from the local abattoir between 24-48 hours after slaughter. The average weight of the pigs was approximately 80 kg.

2.2.1 Harvesting of porcine knee for tribological experiments

The muscles surround the joint were removed to reveal the knee joint capsule. The capsule was carefully opened and all the ligaments and tendons were cut to separate the femur and tibia. The femur and tibia could only be used if the medial tibiofemoral articulating surface showed no visible damage or signs of degradation such as darkening or swelling.

The femur was clamped on the dissection table with the articulating surface facing upwards (Figure 2.1). The medial condyle specimen was harvested by making a cut at the inter-condylar notch in an approximately sagittal plane, the cartilage surface lining on the medial condyle was kept intact. Details will be described in Section 3.2.1.

The radius of the specimen was assessed using a series of CAD templates of known radius between 20 to 31 mm (Figure 2.3). The bony part of the medial condyle specimen was then cut into a stem with a width of approximately 20 mm.

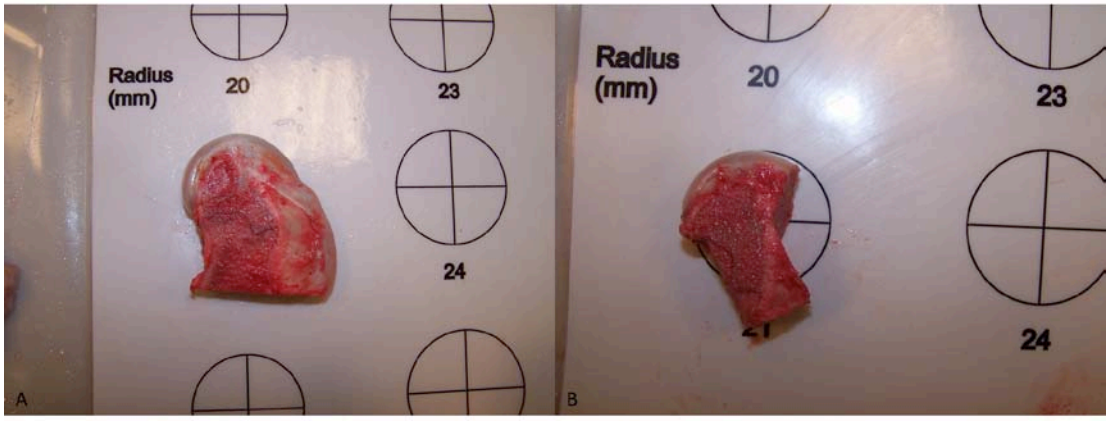

Figure 2.3 Photos show trimming of condyle specimen guided by CAD templates of known radius between 20-31 mm. (A) Femoral condyle was matched to the CAD templates to measure the radius of the flexion facet. (B) The condyle was further cut into a specific shape to fit into the pendulum friction simulator.

The tibial bones were fixed to the clamp, with the medial side facing upwards. A cut beneath the plateau with a sagittal cut between the medial and lateral sides of the surface was made to harvest the tibia specimen (Figure 2.4). Details will be described in Section 3.2.1.

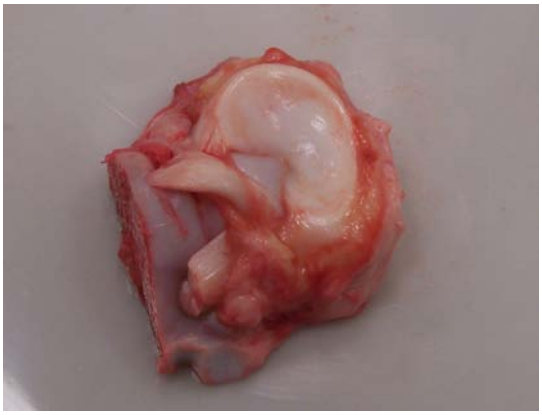

Figure 2.4 Porcine medial tibial plateau with meniscus attached intact.

In the development of the partial meniscectomy model, the following landmarks of the medial meniscus were indentified: anterior and posterior horns, the junction of anterior and middle thirds of meniscal tissue, the radial width of the middle third, and the inner 40% of the radial width of the middle third. A series of scissor punches were used to remove the inner ring of meniscal tissue. The resection started from the junction of the anterior and middle thirds, to the end of the anterior two thirds of the posterior third. The anterior third and one third of the posterior section, which connected the posterior horn was kept intact. Sudden changes in contours or leaving a residual flap at either end were avoided (Figure 2.5, 2.6).

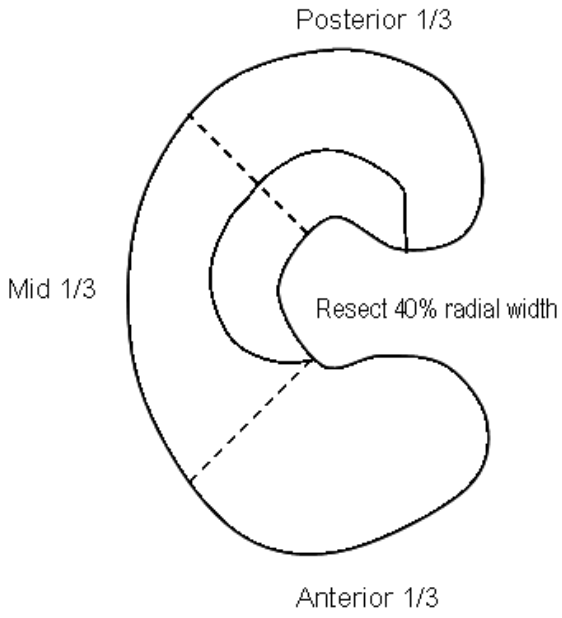

Figure 2.5 Schematic diagram of resection of the "inner section" of the meniscus.

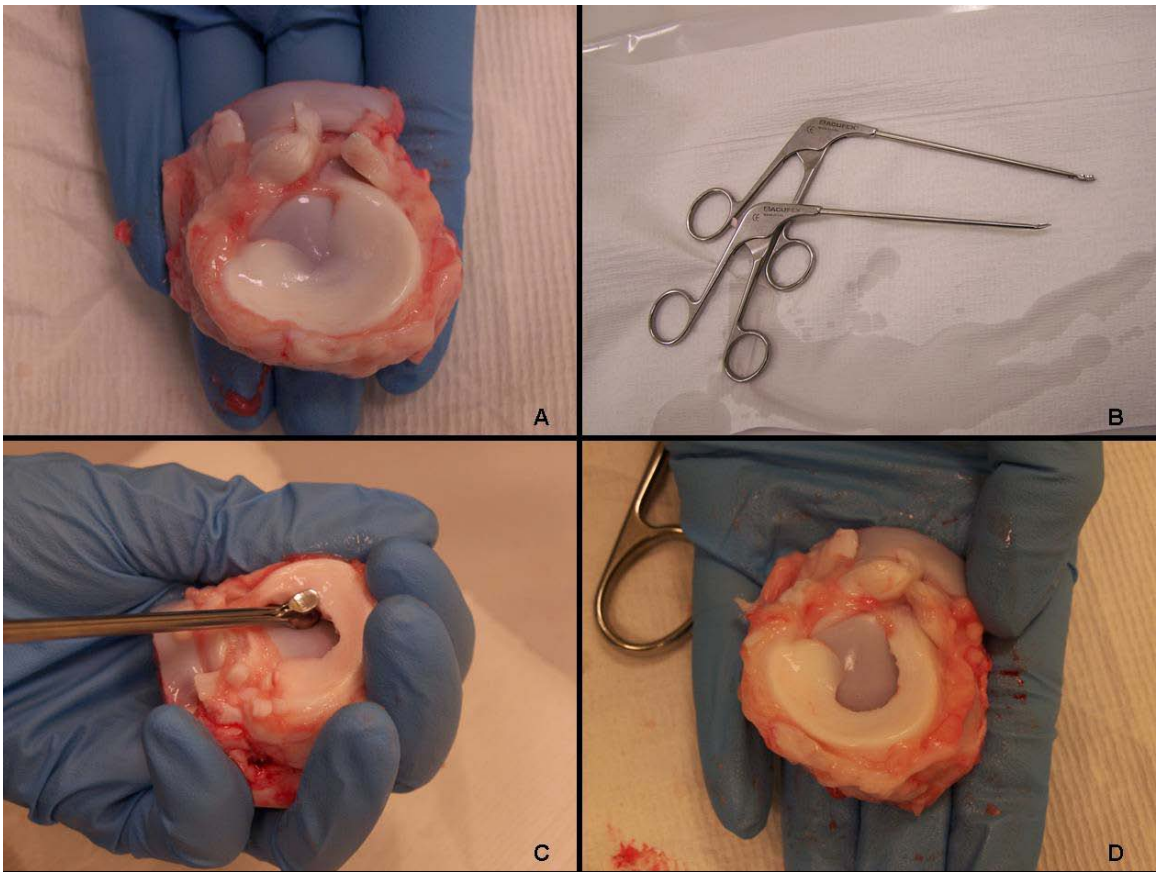

Figure 2.6 Development of the partial meniscectomy model for tribological experiments. A) Intact porcine medial meniscus and tibial plateau. B) Scissor punches. C) Removal of inner third of meniscal tissue. D) Completed partial meniscectomy model.

The condyle and tibia samples harvested from the same joint were wrapped in PBS-soaked tissue and put in a reasealable plastic bag with labels, and stored at -20 ˚C.

2.2.2 Harvesting of porcine medial meniscus for MRI

The porcine medial menisci were harvested from the same animal legs as described in 2.2.1. In total 24 medial menisci with no visible defects were carefully harvested using a scalpel and forceps, leaving the whole meniscal tissue including part of the anterior and posterior horns with adherent capsular soft tissues. The dimension of each meniscus was measured using a steel ruler.

Two axially oriented lines were drawn on the superior surface of four medial menisci. The distance between the two lines was approximately 5 mm. Four small cuts were carefully created at both ends of the lines (on the inner and outer edges of tissue) using scalpel blades (Fig 2.7). These defects served as markers for registration of MR images and images of stained histological sections.

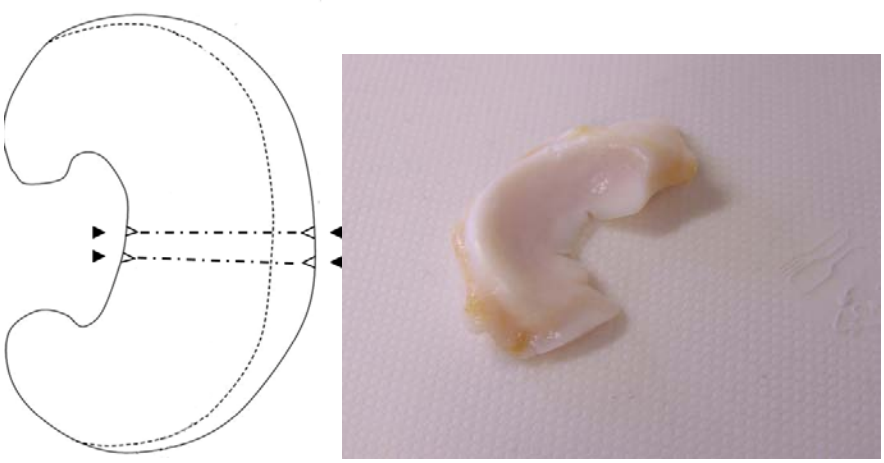

Figure 2.7 Creation of markers on the meniscus. The left drawing showed the cuts on the inner and outer edges. The right photo showed the sample with markers.

Lesions resembling longitudinal tears were created on two of the menisci immediately after dissection using a No.11 scalpel blade. The menisci were wrapped in PBS soaked paper tissues and stored at -20ºC until 6 hours before MRI scans. The completion of harvesting all 24 menisci samples spanned a period of 18 months to coordinate the availability of MRI scanners. All menisci were subject to MRI scanning within one month of harvesting.

2.3 Experimental Methods

2.3.1 Pendulum friction simulator testing

Pendulum friction simulator

All of the simulation tests of cartilage wear were performed using a pendulum friction simulator (Simulation Solutions, UK) (Figure 2.8). It is a single-station servo-hydraulic machine, controlled by a computer via a graphic user interface, which can apply a dynamic loading and motion cycle similar to that of the knee. The set-up procedure for the pendulum friction simulator is presented in the following paragraph.

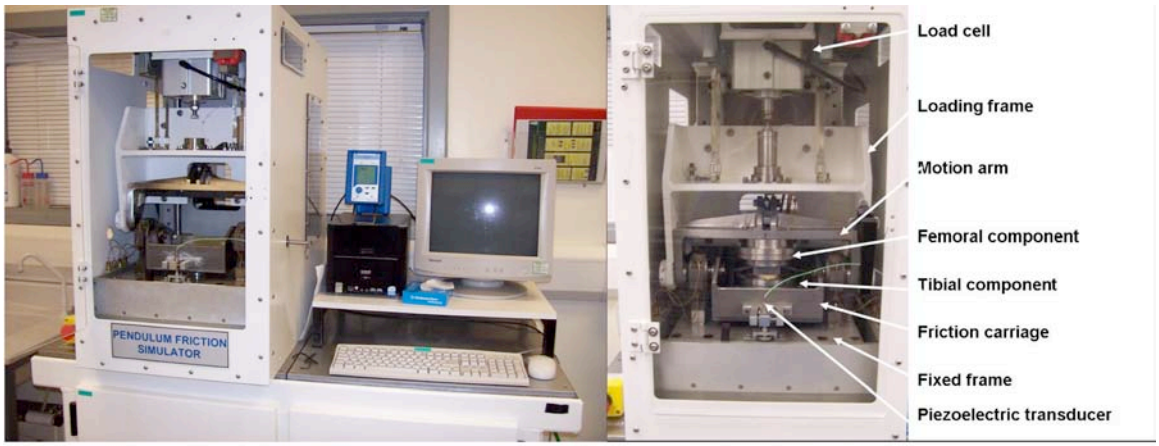

Figure 2.8 Images of the ProSim friction simulator.

Fixturing of specimens

The porcine medial knees harvested as described in section 2.2.1 were used as tibiofemoral compartment models in the pendulum friction simulator testing. A series of jigs were used to set up specimen components (Figure 2.9). The delrin fixtures were used to temporarily hold the femoral condyle specimen in the femoral holder (Figure 2.10). When the optimal specimen position was obtained, *i.e.*, the crown of the condyle specimen matched the inside arc of the fixture and the height was adjusted to be within the desired range (for porcine specimen: 19-23 mm), a long flat-faced screw was used to maintain this position. Correct positioning of condyle was critical for correct operation of the pendulum friction simulator.

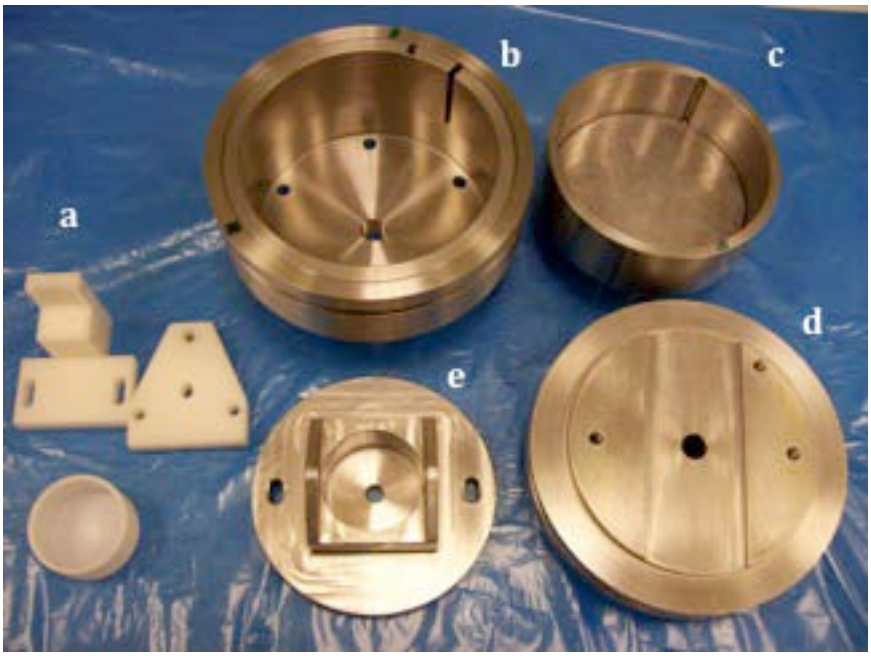

Figure 2.9 Jigs for friction simulator testing. (a) Delrin fixtures and pot. (b) Tibial base component with clamping ring in place. (c) Tibial specimen holder with flat stainless steel plate in place. (d) Femoral base component. (e) Femoral specimen holder.

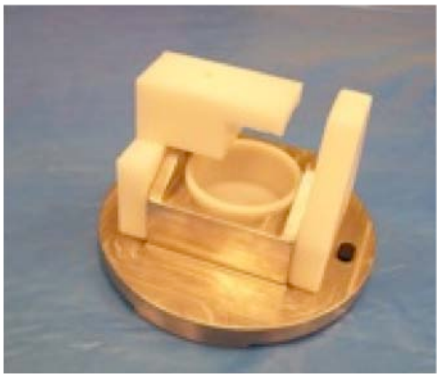

Figure 2.10 Femoral specimen holder with delrin jig attached.

The femoral compartment was then set up in the following way. PMMA bone cement was prepared as described in Section 2.1.2. It was quickly injected into the delrin pot and left to set for 15-20 minutes. When the bone cement was fully hardened, the delrin fixtures with the long flat-faced screw were removed, while two screws were placed through holes in the femoral specimen holder to prevent any micro-motion of the specimen during the test. In the meantime, a second quantity of bone cement was prepared and left to

partially cure to a paste for five minutes and then it was pasted around the specimen (Figure 2.11A).

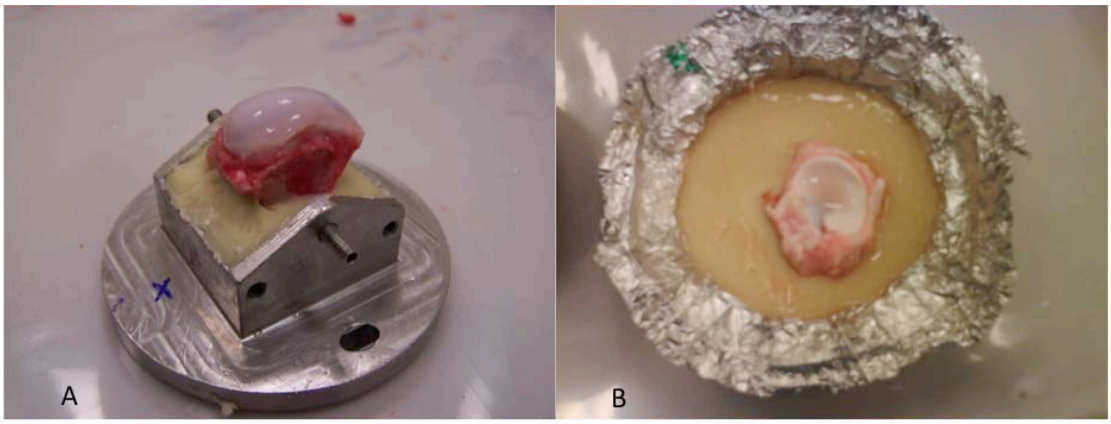

Figure 2.11 Porcine medial knee model potted in jigs separately, ready for friction simulator testing. A) Femoral condyle. B) Tibial plateau with the meniscus.

After the femoral condyle component was set up, it was fixed in the friction simulator. The tibia holder (Figure 2.9c) was covered with a piece of aluminum foil to prevent leaking of lubricant. The tibial specimen was then placed freely in the specimen holder in the simulator, and it was allowed to spontaneously move into a natural articulating position when it was contacted by the condyle under the weight of the bulkhead. A permanent marker was used to draw an outline of the base of the tibial specimen onto the specimen holder. The condyle component and tibial component were disassembled, and the tibial specimen and its holder were then transferred to the fume cupboard. PMMA bone cement was prepared and injected around the tibial specimen, which was pre-positioned according to the outline drawn.

Details of model development and set-up for friction simulator testing will be described in Chapter 3.

2.3.2 Magnetic Resonance Imaging

All cartilage and menisci samples were scanned using a 9.4 Tesla laboratory NMR system and a 3.0 Tesla clinical MRI scanner described below. All samples were subject to MRI scanning within one month from harvesting. After thorough defrosting, PBS soaked paper tissues were removed.

The 9.4 Tesla NMR system

Figure 2.12 The 9.4 Tesla Bruker Avance™ II 400MHz laboratory NMR system.

The ultra high field 9.4 Tesla Avance™ II 400MHz NMR system used in this study as shown in Figure 2.12 was from Bruker Company (UK). Only one sample was scanned each time to minimise the influence of magnetic field inhomogeneity. The cartilage sample (femoral condyle and tibia) was always positioned in the specimen holder with the articulating surface facing laterally. The meniscus specimen, with supporting pads made of polyester foam material, was put into a specimen holder/tube (diameter= 25 mm) as shown in Figure 2.13. The specimen holder was sealed with a lid. All samples were

scanned at a consistent temperature of 22 ± 0.6 ºC.

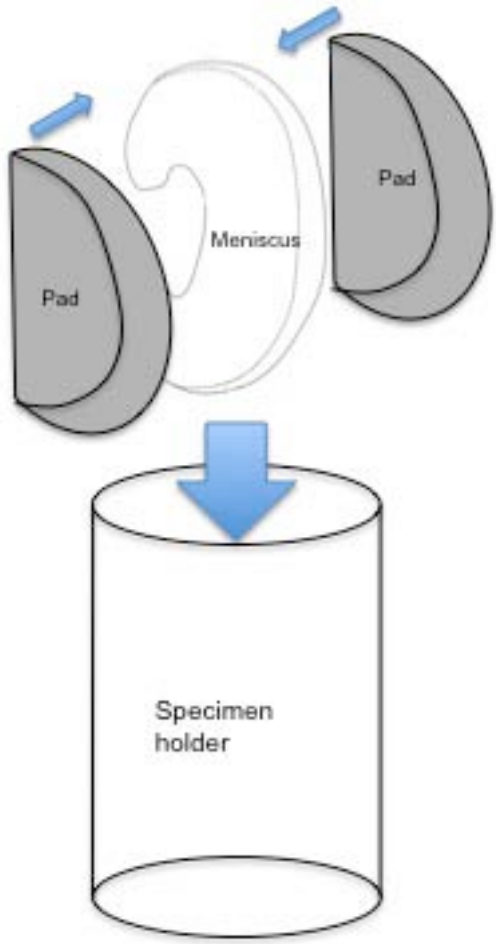

Figure 2.13 Illustration of meniscus sample preparation for the 9.4T MRI. The meniscus was positioned vertically into the specimen holder, with two foam pads supporting the sample.

Details of imaging protocol development will be discussed in Chapter 5.

The 3.0 Tesla MRI scanner

The clinical MRI scanner used in the study was a 3.0 Tesla Siemens Magnetom Verio system, which was located in the Leeds Musculoskeletal Biomedical Research Unit (LMBRU). The transportation of porcine samples between the University and hospital strictly obeyed the Standard Operation

Protocol (SOP.09.9) of the Institute of Medical and Biological Engineering, University of Leeds.

The condyle and tibia samples from the same knee were put in a 25mm diameter specimen holder in a manner such that the two samples did not overlap each other. Twelve cartilage samples from the positive control group were placed in six holders and arranged in a honeycomb-like array using tapes. Using the same method, an array of six samples from Pycnometer validation study was also prepared. This allowed acquisition of MR images of multiple samples during one scan (Figure 2.14). The array of samples was placed on the patient table with the tubes in the direction of the main magnetic field direction (B_0).

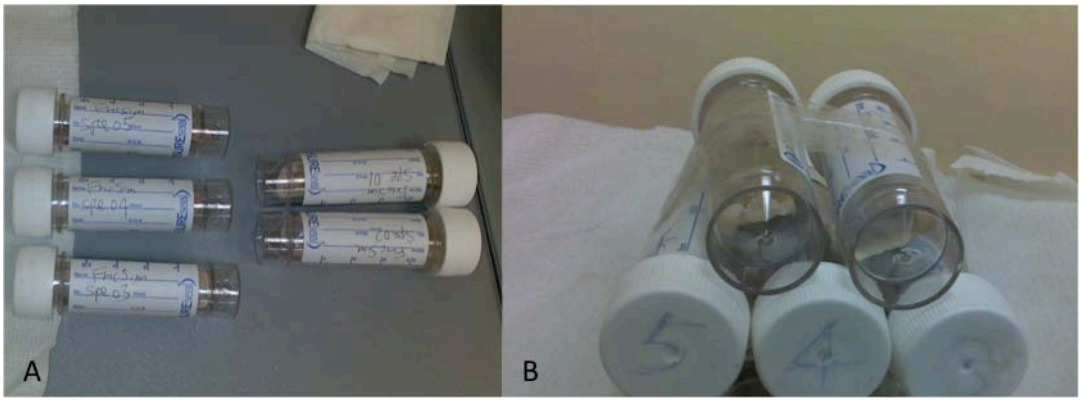

Figure 2.14 An example of sample preparation for 3.0T MRI study of porcine cartilage samples. Samples were arranged in a honeycomb-like array, and they were scanned together during 3.0T MRI studies.

One porcine medial meniscus was scanned at 3.0 Tesla MRI to investigate the ability of mid-field MRI of demonstrating intrameniscal structures. The meniscus sample was immersed in 0.9% (w/v) sodium chloride solution and sealed in the 25mm diameter tube. The reason for using sodium chloride solution was that the meniscus sample could not generate sufficient MR signals for the 3.0T scanner, and due to the limitation of the size of the loop

coils no extra tubes could be added to enhance the signal. The tube was placed vertically on the patient table. Two four-channel loop “surface” coils were used for imaging (Figure 2.15).

Figure 2.15 Photo of setting up of a 3.0T MRI scans of porcine meniscus sample. The two four-channel loop surface coils were overlapped and with their loops surrounding the sample holder to achieve best image quality.

2.3.3 Post-acquisition MR image analysis

The signal-to-noise ratio (SNR), contrast-to-noise ratio (CNR) and relative contrast (ReCon) of meniscal MR images were measured using the Analyze^{TM} software (Mayo Clinic, USA). A square region (size 20×20 voxels) of the typical intrameniscal high signal area was selected, and the mean value of the signal intensity was calculated as SI_{HIGH}. Another square region (size 20×20 voxels) of the intrameniscal low signal area was selected, and the mean value of the signal intensity was calculated as SI_{LOW}. The largest possible region outside the meniscus in the image background was also

selected, and the standard deviation of the background noise intensity was calculated as $Noise_{SD}$ (Figure 2.16). The measurements were calculated using the following equations (1-3):

$$SNR = \frac{SI_{HIGH}}{Noise_{SD}} \quad \text{(equation-1)}$$

$$CNR = \frac{SI_{HGIH} - SI_{LOW}}{Noise_{SD}} \quad \text{(equation-2)}$$

$$ReCon = \frac{SI_{HIGH} - SI_{LOW}}{SI_{HIGH} + SI_{LOW}} \quad \text{(equation-3)}$$

For each image sequence, the six best images were chosen for SNR measurement, and the mean value of SNR, CNR, ReCon with standard deviation were calculated.

To demonstrate the definition of acquired images, equation 4 was used:

$$\text{Image definition (ID)} = \frac{1 \times 10^9 \mu m^3}{Voxel \quad volume} \quad \text{(equation 4)}$$

In the meniscus MRI, the mean value of the ID of different imaging sequences was calculated and compared.

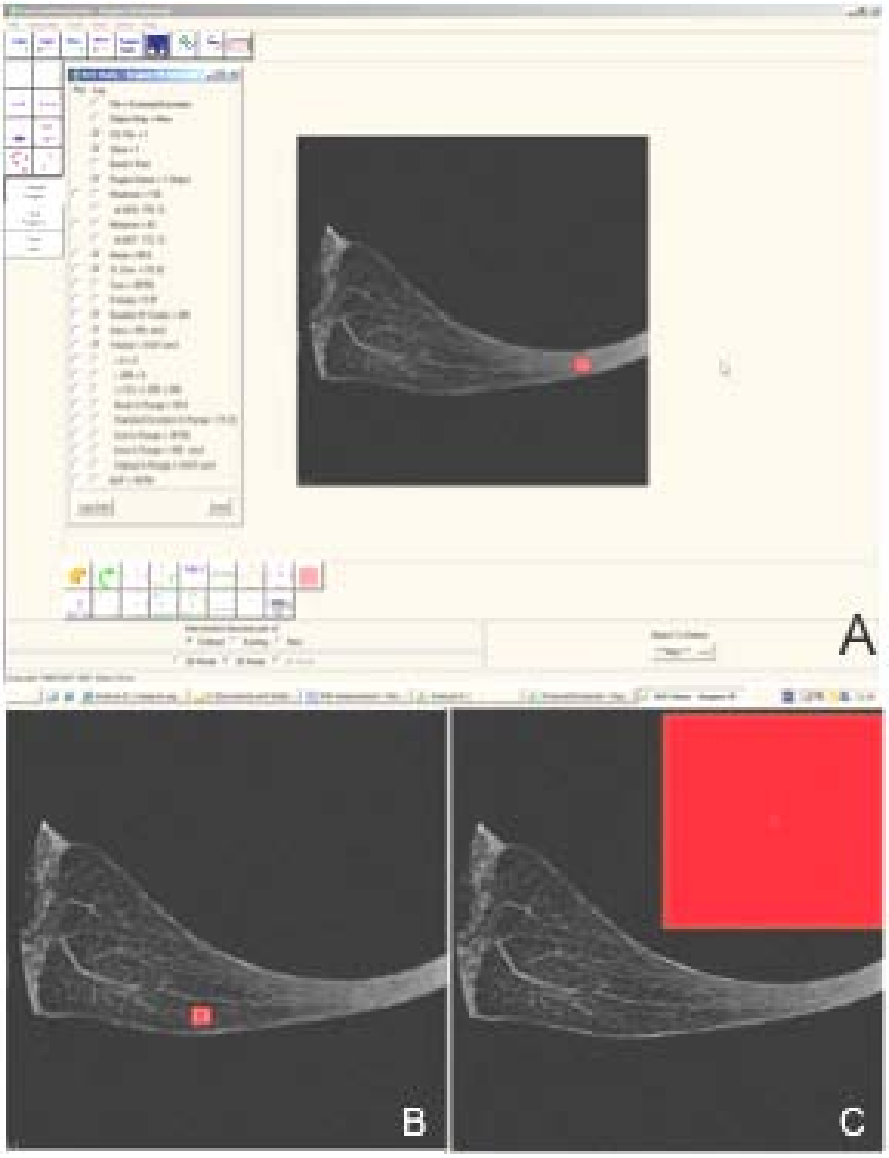

Figure 2.16 An example of SNR and ReCon measurement of meniscal MR images using the Analyze™ software. The red boxes show the region selection.

2.3.4 Cartilage wear quantification

MRI-based 3D volume measurement

Two MRI-based methods, a MATLAB™ 2D profile method and an ITK-SNAP 3D surface reconstruction method were used to study cartilage wear volumes as described in Section 4.3.3.

Validation using pycnometer

To validate the MRI wear volume quantification method, an AccuPyc 1330 Pycnometer-based method was developed. The AccuPyc 1330 is a gas expansion pycnometer used for accurately measuring the volume of solids (Figure 2.17).

Figure 2.17 Photo of the AccuPyc 1330 Pycnometer.

The pycnometer device required its holder to be at least two-thirds full to obtain and accurate volume reading. The standard sample holder used in this study had a 10 cc capacity. Because the cartilage samples were relatively small, with an average volume of less than 0.1 cc, additional fillers were added to the sample holder to meet the requirement. Fillers included two calibration stainless steel spheres (approximately 3 cc each), and an additional large cartilage piece harvested from fresh porcine knee.

Two separate measurements were made in each experiment. Firstly, the fillers was measured and recorded as datum Volume-1 (Figure 2.18, A). Secondly, a cartilage sample was put together with the fillers and measured as Volume-2 (Figure 2.18, B). The volume of cartilage sample could be calculated by subtracting Volume-1 from Volume-2.

The reason to introduce an additional cartilage piece is that an average 10 minutes measurement duration and the air flow nature of gas pycnometer

introduced unavoidable tissue dehydration. By pressing the small cartilage sample onto a large cartilage piece to form a larger piece, the influence of tissue dehydration could be reduced, and therefore more reliable volume readings could be produced. The filler cartilage was only used once, *i.e*., for each measurement, a fresh filler cartilage piece was applied.

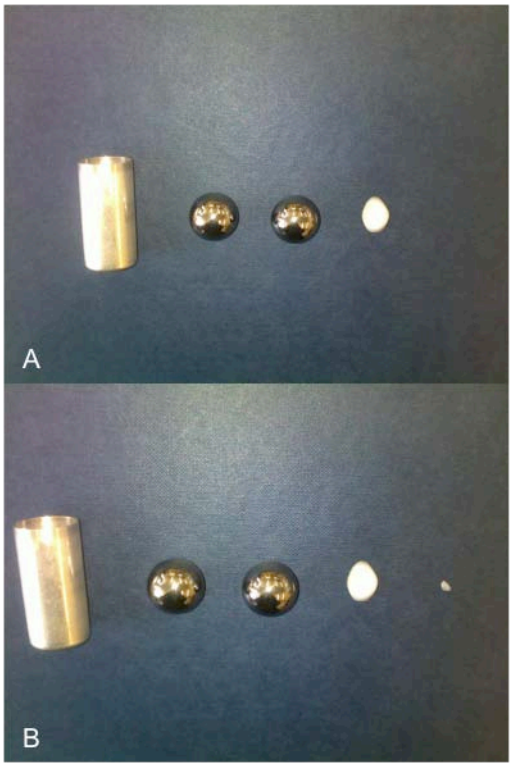

Figure 2.18 Sample preparation for pycnometer measurements. A) Measurement of fillers. From left to right: 10cc sample holder, two spheres, and a filler cartilage. B) Measurement of fillers plus cartilage sample. From left to right: holder, two spheres, filler cartilage, and cartilage sample.

2.3.5 Histological staining and microscopy

Four porcine meniscus samples with markers that had been analysed by MRI as described in section 2.2.2, were subjected to histological examination in order to compare the intrameniscal structures demonstrated on MRI and histologically stained sections. Histological staining techniques used in this study included Sirius red and haematoxylin and eosin (H&E). Tissue sections were also assessed for collagen IV expression using immunohistochemistry.

An approximately 5 mm wide block was cut from the meniscal tissue using a disposable scalpel blade. The cut strictly followed the markers to ensure accurate comparison between MRI and histology at the same position (Figure 2.19).

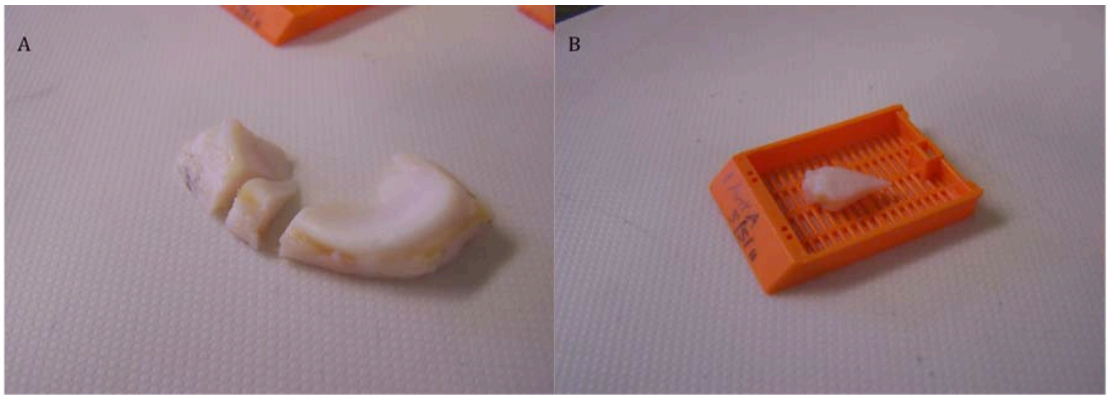

Figure 2.19 Dissection of meniscal tissue for histological staining. A) A block of tissue was cut following the previously made marks. B) The excised block was placed into a small plastic cassette (Histosette®) for dehydration.

The excised tissue block was placed into a small plastic cassette (Histosette®) prior to dehydration using an automatic tissue processor. The automatic tissue processor immersed the tissue block in several liquids in the following order: 70% (v/v) alcohol for 1 hour, 90% alcohol for 1 hour, 100% alcohol for 2 hours 20 minutes, 100% alcohol for 3 hours 20 minutes, 100% alcohol for 4 hours 20 minutes, xylene for 1 hour, xylene for 1 hour 30 minutes, xylene for 2 hours, molten paraffin wax for 1 hour and 30 minutes, molten paraffin wax for 2 hours, and molten paraffin wax for another 2 hours. Following processing, the tissue block was placed in a wax block mould and covered in molten wax. The mould was removed when the wax had thoroughly solidified, and the wax embedded block was sectioned at 6 µm thickness using a microtome. The sections were transferred to a warm water bath at 40 °C, and then collected onto Superfrost Plus microscope slides, fixed and dried. The slides were de-waxed by immersion in two containers of xylene for 10 minutes each time, and were then rehydrated in three containers of 100% alcohol for 2, 1 and 1

minute respectively, followed by dipping in 70% alcohol for 30 seconds and rinsed in running tap water for 5 minutes.

The Sirius Red and H&E staining technique involved immersion of the slides in pre-made solutions. Chemicals and reagents used to make these solutions are listed in Table 2.2.

Table 2.2 Chemicals and reagents used together with UK suppliers

Chemical/Reagent	**Supplier**
Xylene	Genta Medical
Ethanol	Thermo Fisher Scientific Ltd.
Scott's tap water	Thermo Fisher Scientific Ltd.
Eosin	VWR International
Haematoxylin	Thermo Fisher Scientific Ltd.
Sirius red	Raymond A Lamb Ltd
DPX mountant	Thermo Fisher Scientific Ltd.

Staining: Sirius Red

The 0.1% (w/v) Sirius red solution was made by dissolving 0.1 g Sirius red into aqueous saturated picric acid solution using a magnetic stirrer. Slides were immersed in the Sirius red solution for one hour, followed by immersion in 70% ethanol for 5 seconds, 100% industrial methylated spirits for 5 seconds, 100% industrial methylated spirits for 2 minutes, 100% industrial methylated spirits for 3 minutes, clean xylene for 10 minutes, and clean xylene for another 10 minutes.

Staining: Haematoxylin and Eosin

Slides were immersed into Haemotoxylin for 1 minute, Scott's water for 3 minutes, 1% (w/v) Eosin for 3 minutes. Running tap water was used to wash slide between each of the abovementioned steps. The same dehydration procedure was applied as described in Sirius red staining, i.e., immersion in ethanol gradient (70% and 100%) and clean xylene.

After the staining procedure, the slides were mounted using DePex mountant and then covered by glass cover slips. An Olympus BX51 microscope (Olympus, Japan) was used to fulfill bright-field microscopy of the stained slides (normal Koehler illumination for H&E stained slices, and normal Koehler illumination and polarized light for Sirius red stained slides). Photographs of microscopy images were captured digitally using attached software.

Collagen IV staining

Collagen IV staining is an immunoperoxidase labeling technique which is highly specific for localization of blood vessels in porcine meniscus. The principle is that collagen IV presents in the basal laminar surrounding endothelial cells and can be used as a target antigen for identification of blood vessels in tissue matrix.

The section of fresh porcine meniscus was fixed in a pre-made zinc fix solution for 16 hours, embedded into paraffin wax and then sectioned, placed on slides. The slides were placed into slide holders and immersed into dewax xylene for 10 minutes, xylene for another 10 minutes, 100% ethanol for 3 minutes, 100% ethanol for 2 minutes, 100% ethanol for 2 minutes, 70% (v/v) ethanol for 2 minutes, running tap water for 3 minutes. Antigen retrieval was carried out using Proteinase K (Dako Cytomation, UK) for 20 minutes. The slides were then immersed in 3% (v/v) hydrogen peroxide in phosphate buffered saline (PBS) for 10 minutes at room temperature, running tap water for 3 minutes, circled around using a hydrophobic marker, and washed using

Tris Buffered saline (TBS). 25 μl dual endogenous enzyme block from the Envision kit was added to slide incubate for 10 minutes before repeated TBS washed for two times. The antibody was applied at 1:50 dilution and incubated for 1 hour at room temperature. 20 μl of labeled polymer-HRP from the Envision kit was then added. This was left to incubate for 30 minutes at room temperature in the dark before repeating the duplicated washing procedure using TBS containing 0.05% (w/v) Tween 20 for 10 minutes each, and another two times of TBS for 10 minutes each. 15 μl of substrate chromagen from the Envision kit was added to incubate for 10 minute at room temperature before the slides were washed four times using distilled water. The slides were immersed in haematoxylin for 10 minutes, 70% (v/v) ethanol for 5 minutes, 100% ethanol for 1 minute, 100% ethanol for 2 minutes, 100% ethanol for 3 minutes, clean xylene for 10 minutes, clean xylene for another 10 minutes. The slides were mounted using DPX mountant and air dried for 4 hours before being viewed on the light microscope under normal Koehler illumination.

Chapter 3 Simulation of Cartilage Wear and Damage

3.1 Introduction

It has been known that the meniscus provides many important functions within the knee joint such as load transmission and redistribution of load to reduce contact stresses in articular cartilage, and it protects the underlying cartilage. Since the 1970's, studies have revealed that partial and total removal of the menisci has different degrees of effect on knee degeneration (Johnson *et al*., 1974; Cox *et al*., 1975; McGinty *et al*., 1977; Wilson *et al*., 2003). A retrospective study showed that 39% patients after partial meniscectomy suffered less degenerative changes of the knee than those who had a total meniscectomy (Andersson-Molina *et al*., 2002). Therefore, partial meniscectomy, rather than total meniscectomy would be firstly considered when meniscal repair is thought to be unachievable to preserve the normal meniscus tissue as much as possible. A methodology of *in vitro* determination and measurement of the loss and damage to articular cartilage following loss or damage to the meniscus would be of value in the biotribological and biomechanical study of the knee.

A bovine medial knee model was developed by McCann *et al*. (2009) for the pendulum friction simulator testing. It demonstrated through an *in vitro* investigation the tribological effects of meniscectomy while keeping the natural anatomy of the joint, and showed that removal of the meniscus led to direct degradation and wear on cartilage in a short term. However, the size of this bovine model exceeded the capacity of the magnet bore of the laboratory MRI scanner. To assess the capability of MRI in morphological quantification of naturally occurred cartilage wear and damage, a new *in vitro* medial knee model was needed to meet the following criteria: contain whole medial tibiofemoral compartment; can be tested in the pendulum friction simulator; the post-simulation femur and tibia samples can be investigated in the laboratory MRI without cutting of cartilage surface.

The objectives of experimental investigation in this chapter were to develop an *in vitro* porcine medial knee compartment model and to simulate wear and damage to articular cartilage following meniscectomy, which was then quantified using MRI.

3.2 Materials and Methods

3.2.1 Development of porcine models

Medial femoral condyles and medial tibial plateaus were harvested from healthy right porcine legs as described in Chapter 2. After careful removal of surrounded muscles, the articulating angle (θ) of porcine femur and tibia was determined to be approximately 30 degree (Figure 3.1). The knee capsule was then removed to reveal the femoral condyles, menisci and tibia plateau.

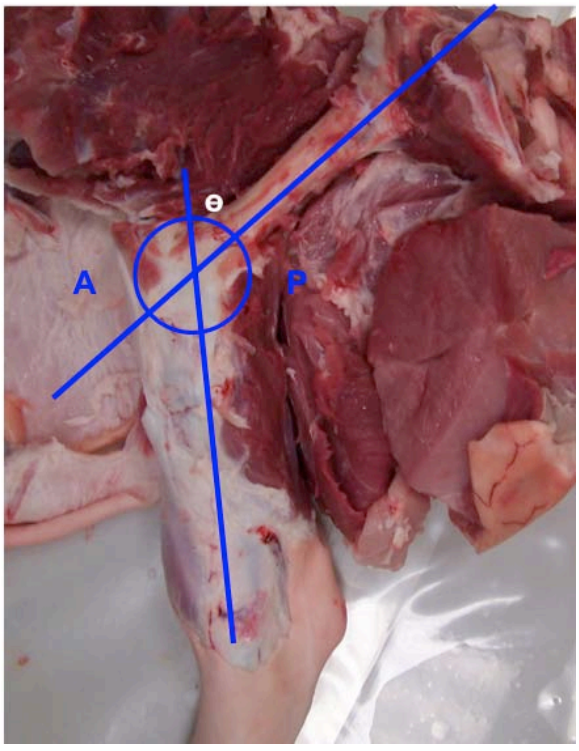

Figure 3.1 A photograph of a right porcine leg with muscles removed from femur. The articulating angle (Θ) of femur and tibia was approximately 30 degree. A: anterior, P: posterior.

The medial femoral condyle was harvested with the intact cartilage crown from the grooves to posterior end of condyle. The radius of the specimen was assessed using a series of CAD templates of known radius between 20 to 31 mm. The bony part of the medial condyle specimen was then cut into a stem with a width of at least 20 mm (Figure 3.2).

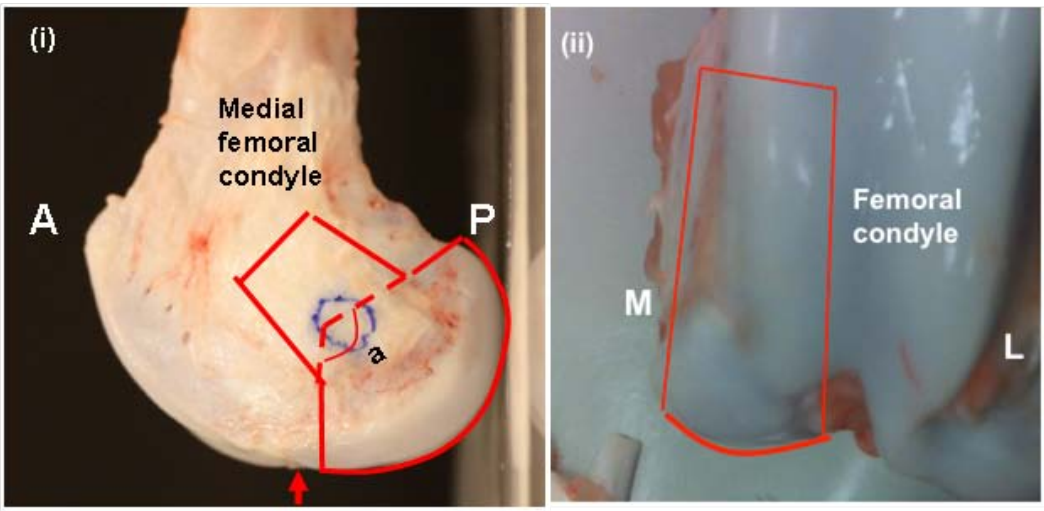

Figure 3.2 Harvest of porcine medial femoral condyle for testing on the pendulum friction simulator. (i) The lateral view of condyle. Red solid lines represent the lateral cut. The arrow shows the groove, angle a > 90 degree.

Due to skeletal immaturity of pigs used in the study, the porcine bone was still soft. In addition, the bone had a growth/epiphyseal plate (Robinson *et al*., 1988; van Mourik *et al*., 2001; Bauer *et al*., 2006; Sergerie *et al*., 2009). The follow-up MRI showed that the epiphyseal plate of condyle was located right at the neck of the bone stem, which was prone to be fractured during the friction simulator testing. Therefore, the bony stem was cut as thick as possible and yet could also fit into the jig (Figure 3.3).

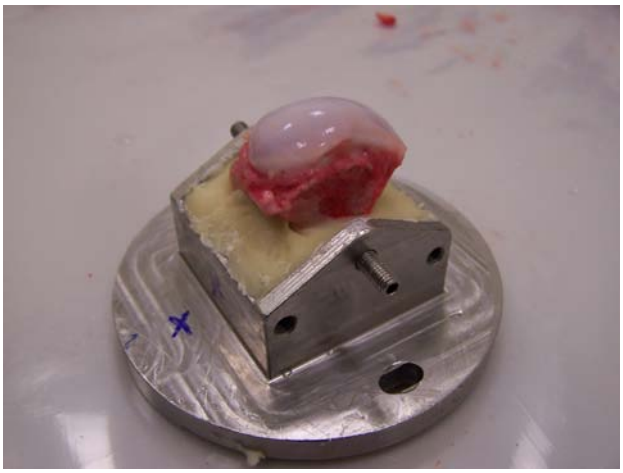

Figure 3.3 Photo of trimmed femoral condyle specimen had been set up into the jigs using screws and bone cements. The whole cartilage crown on the condyle was preserved and been kept hydrated before friction simulator testing.

Unlike bovine tibia, the porcine bony tibia plateau had greater slope cranially, and had a much rounder shape laterally. To determine the tibia part for the friction simulator testing, two cranial cuts and two lateral cuts of the bone were studied in trial friction simulator tests (Figure 3.4).

The tibial bony surface was cut complete beneath the medial tibial surface as thinly as possible (less than 2 mm thick), using a hacksaw. The meniscus and its meniscal horns on the tibial surface were kept intact for negative control experiments, or were carefully removed without damaging the tibial articulating surface for positive control experiments. Other soft tissues such as fat were removed carefully using a scalpel blade. PBS was used to hydrate the specimens throughout the dissection procedure.

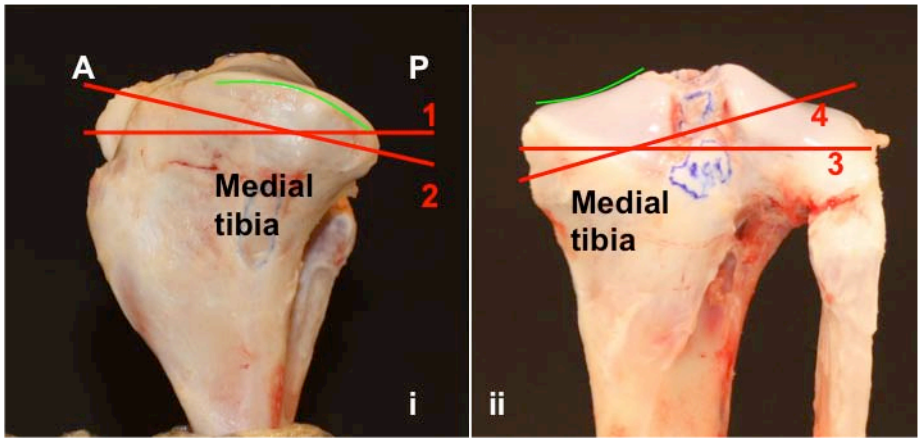

Figure 3.4 Illustration of dissection of porcine tibia plateau (without meniscus). The green lines demonstrate the curving feature of the tibial surface. Four red solid lines demonstrate the four different ways of bone cutting. A: anterior, P: posterior. i) Illustration of sagittal cuts, line 1: "horizontal cut" which was perpendicular to the tibial longitudinal axis; line 2: "tangential cut" which was parallel to the tangential line of the top crown of the tibia plateau. ii) Cranial cuts, line 3: "horizontal cut" perpendicular to the tibial longitudinal axis; line 4: "tangential cut" which was parallel to the tangential line of the bottom concave of the tibia plateau.

During the trial tests, the tangentially cut tibia base prevented abrupt movement of femoral condyle, which happened when the other cut was applied. Without the stabilisation of capsule and ligaments, the slope of the plateau resulted in lateral movement of the tibial component within the friction simulator during test. The situation was worse when a meniscectomy model was used, which lacked the support of the meniscus. The influence of the slope was minimised by cutting the bone parallel to the tangent line of the tibial curves, both cranially and laterally. Therefore, in the preparation of tibia plateau for friction simulator test, care was taken to cut the specimen cranially and laterally as following tangential lines.

The partial meniscectomy model was developed as described in Section 2.2.1.

During the dissection process, all of the articular cartilage surfaces were kept hydrated using PBS solution. The samples were wrapped in PBS-soaked

tissue immediately after dissection and put in reasealable plastic bags with labels and stored at -20 ˚C.

Determination of centres of rotation

The general methods of fixturing of specimens and setting up of simulation tests were described in Section 2.3.1. Correct positioning of the femoral condyle during specimen fixturing was critical for correct operation of the pendulum friction simulator. A delrin fixture with a desire height, *i.e*., the centre of its inside arc was 72.83 mm apart from the base, which matches exactly the distance between the center of rotation of the motion arm and the base, was used as a guide when potting the femoral condyle sample. By matching the crown of condyle to the inside arc of the delrin fixture, the centre of rotation of the condyle was matched with the centre of rotation of motion arm.

During the setting up of simulator, it was also critical to align the centres of rotation of the femoral component and friction simulator. After fixturing the condyle and tibia using bone cement, the condyle component was fixed to the motion arm of the simulator, with the tibial holder placed in the tibial base of the friction carriage. The condyle and tibia were allowed to come into contact. The height of tibial holder was adjusted within the base to allow an alignment rod to be inserted through the centre of the friction simulator. This procedure ensured the centres of rotation of the femoral component and friction simulator were aligned.

3.2.2 Development of friction simulation protocol

Determination of simulator profiles

The load cell was pulled down to contact the motion arm firmly. These two parts were responsible for applying the load and the flexion-extension motion

to the knee. A customised program was run on the controlling PC to set up parameters such as loading and flexion-extension angle (Figure 3.5).

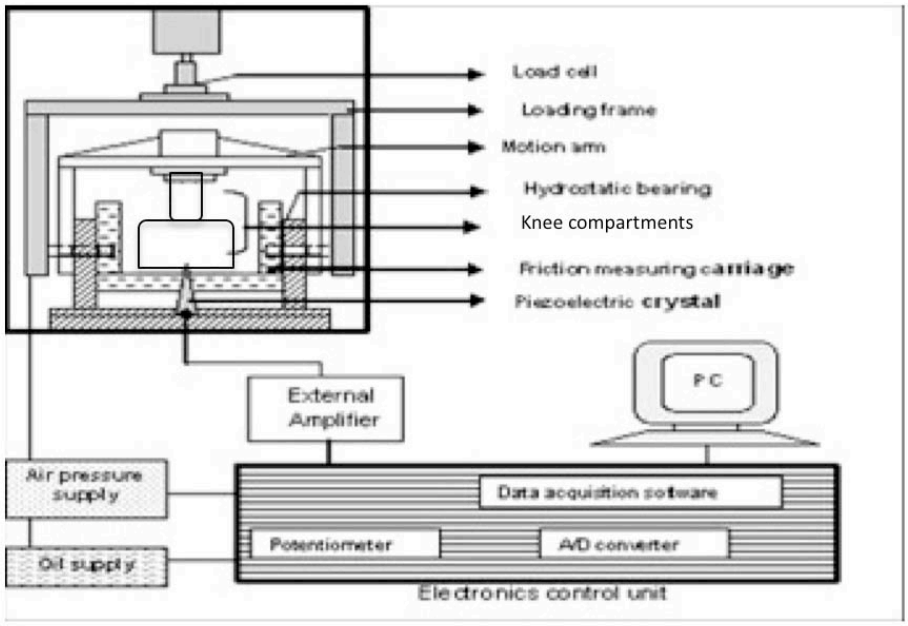

Figure 3.5 Schematic representation of the friction simulator hard- and software.

Derived from the British Standards (BS ISO 14243-3:2004) for knee gait profiles for simulator, the load profile was simplified to a single peak profile as shown in Figure 3.6. The maximum flexion-extension angle was set to be 23 degrees due to the limitation within the machine. The motion profile of flexion-extension is shown in Figure 3.7.

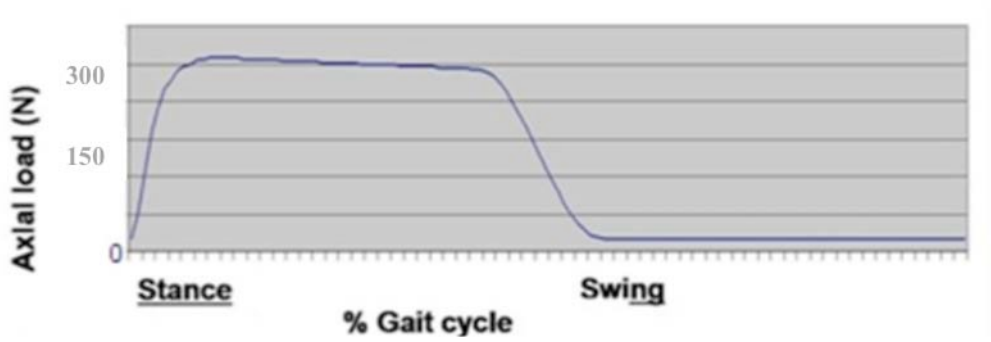

Figure 3.6 The single peak loading profile used during friction testing.

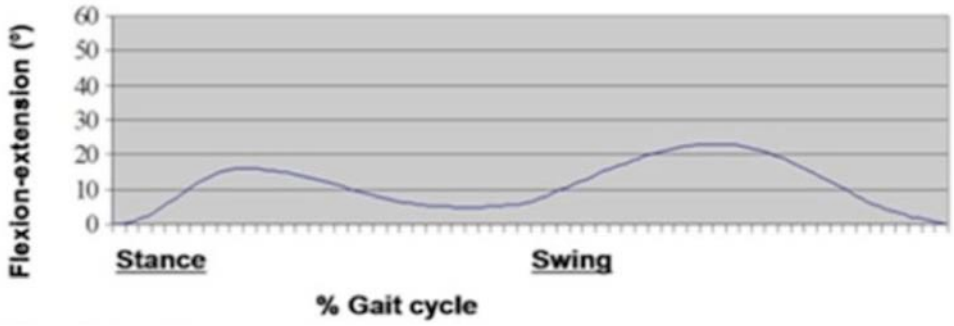

Figure 3.7 The motion profile used during friction testing.

The average weight of pigs used in this study was approximately 80 kg. Since there were no specific studies on porcine knee contact forces to date, the peak load acting through a porcine knee joint was calculated based on two studies of other animal species (Table 3.1), and trial friction simulator tests were carried out applying two different dynamic axial forces.

Table 3.1 Reported tibiofemoral joint peak loads in animals

Authors	Animal specie	Activity	Tibio-femoral joint load (body-weight multiples)
Taylor (2004)	Sheep	Level Walking	2.25
Simon (1970)	Sheep	Standing	0.63
	Cow	Standing	0.7
	Dog	Standing	0.36

The trial test group one (Test-1) used a peak load calculated based on a ovine joint load study reported by Taylor *et al*. (2006). The peak load in the ovine knee was found to be 2 times bodyweight. Because only the medial compartment was tested in this study, and the peak axial force loading through medial compartment was approximately 60% of the full knee joint load for human (Baliunas *et al*., 2002). Therefore, the peak load applied in T-1 was 940 N (80kg×2×9.8×60%).

The trial test group two (Test-2) used a peak load calculated according to Simon's study on bovine joint (Simon, 1970). The peak load applied in Test-2 was 330 N, since the peak load in bovine knee was approximately 70% of its body weight, and approximately 60% of the full knee joint load goes through medial knee (80kg×9.8×70%×60%).

Data collection

Each test was run for 3,600 cycles at 1 Hz to simulate continuous walking for a period of one hour. Data points were recorded once every 20 cycles. The real-time coefficient of friction (f) was calculated by using the following equation

$$f = \frac{T}{R_1 \times W} \qquad (1)$$

Where R_1 is the radius of the femoral condyle, T is the real-time frictional torque measured by the simulator, and W is the applied load.

During each gait cycle, two hundred and fifty six data points were recorded. Throughout these studies, the reading was recorded during the high-load, high-velocity portion of the cycle, as depicted by the shaded region in Figure 3.8. The same data point was analysed in all tests for consistency.

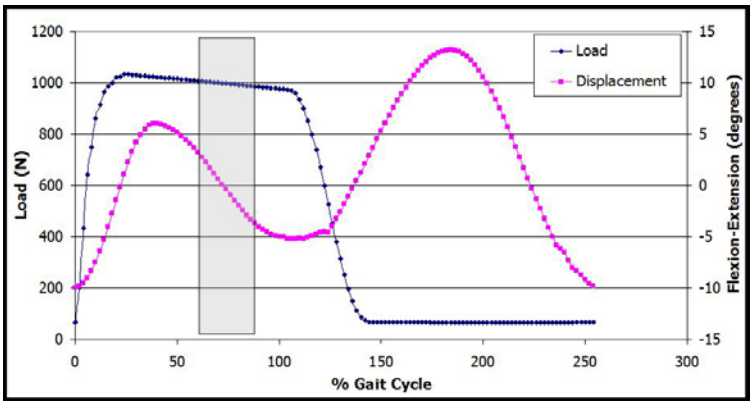

Figure 3.8 The loading and motion profiles of a demand gait cycle. The shaded area indicates the region of high load and high velocity where data was collected.

After being ran for 3,600 cycles at 1 Hz, equivalent to one hour of walking, the trial test T-1 was proven to be applying too high axial force on the porcine model since all of the articulated cartilage was totally rent or worn out in meniscectomy groups (Figure 3.9). The consequent cartilage wear/damage model was not common in most clinically reported cases. In contrast, tests with the dynamic profile with 330N peak load generated moderate wear on the articular surfaces on both femur and tibia. Therefore, only samples post tests with 330N peak load were used in follow-up MRI studies.

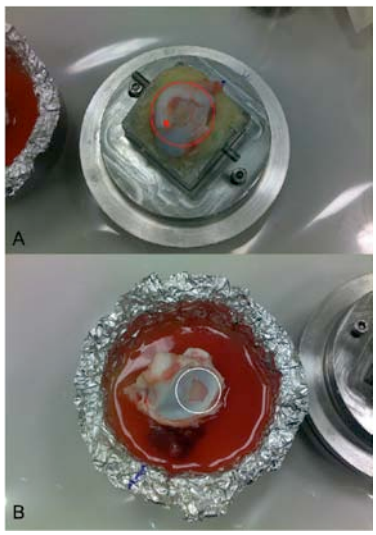

Figure 3.9 Photographs of samples after a 3,600 cycle 900 peak load friction simulator test. Photo A showed the femur and B showed the tibia (without meniscus). Serious cartilage damage could be seen on the articulating surfaces (circled areas).

3.2.3 Calibration of friction simulator

The calibration of pendulum friction simulator was carried out on a monthly basis. The calibration included two parts, load cell calibration and frictional torque calibration. In the calibration of load cell, a transducer indicator was used to measure the real force transmitted through a standard bearing (a metal-on-ceramic femoral head and acetabulum). The calibration constants could be computed by relating the real force against the desired force. The friction torque calibration was done using a standard frictional torque calibration arm, on which a set of weights (0.51 kg each) was put on and taken off in order. All the calibration procedures were completed on the friction simulator computer utilising the automatic calibration functions.

3.2.4 Design of simulation study

After determination of approach of sample preparation, setting of load profile and calibration of simulator, three groups of porcine models were created. Eighteen healthy animal legs were evenly and randomly assigned to the with-meniscus group, total meniscectomy group, and partial meniscectomy group, i.e., each group was assigned six porcine joints. The with-meniscus group served as negative control group for this study, which used natural medial compartment containing intact condyle, meniscus and tibial surface. The total meniscectomy group was the positive control group, which was used to simulate the total meniscectomy situation – the medial meniscus was removed using a scalpel, therefore, the femur articulated directly with the tibial plateau.

The partial meniscectomy group was created as described in Section 2.2.1. Due to the complexity of geometry of the model, the initial objective of testing partial meniscectomy models on the pendulum friction simulator was to

investigate the feasibility of the test. Each simulator test ran for one hour at 1 Hz, i.e., 3,600 cycles, to simulate one hour of activity of the pig.

After the friction simulator testing, the samples were checked immediately before being further trimmed into a smaller section (<20 x 20 x 50 mm^3) to fit into the 25 mm diameter holders for MRI scans. Samples with visible wear were carefully cut with the whole worn area preserved. They were wrapped in PBS soaked paper tissues and stored at -20ºC until 6 hours before MRI scans.

3.2.5 Contact stress measurement

Attempts were made to measure the contact stress between the bearing surfaces in the friction simulator using the pressure sensitive Fuji film (PressureX film, USA). The surfaces of femoral condyle and tibia plateau were sealed with cling film to prevent the influence of any possible fluid on the Fuji film. A set of strips of Fuji film was carefully placed on the femoral condyle to cover the entire articular surface (Figure 3.10, A).

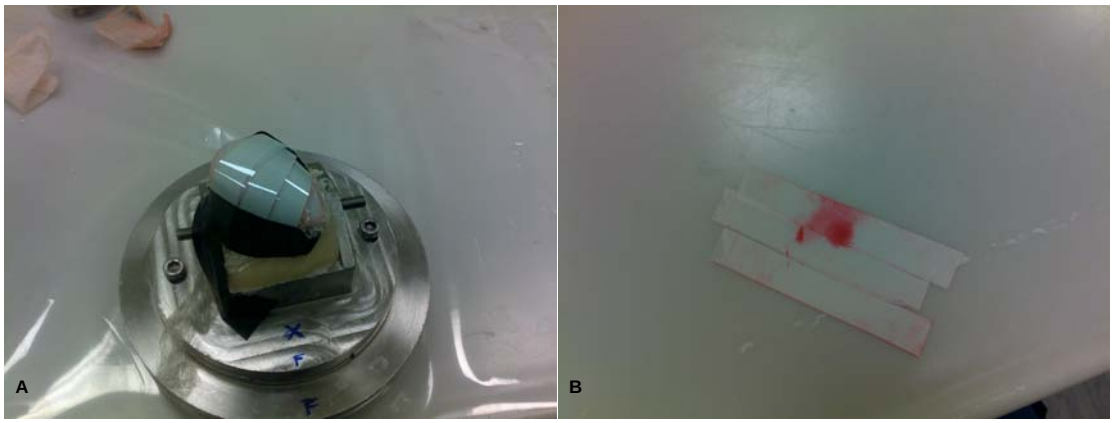

Figure 3.10 Contact press measurement of porcine medial knee model. A) The articulating surface of condyle was covered by 3 strips of pressure sensitive Fuji films. The films were kept in position by a black tape. B) The post-test strips were laid flat in their original order. The pink marks showed the contact area, the darker the pink was, the higher the contact pressure was applied.

A static load of 330N was applied for 15 seconds after the setting up of specimen and friction simulator. The Fuji film strips were then removed from sample and placed on a flat surface in the original order (Figure 3.13, B) and the densest part of the pink mark on the film was scanned in an X-Rite™ Spectrodensitometer.

3.2.6 Cartilage wear quantification

After the friction simulator testing, the samples were checked immediately. No visible wear could be found on the cartilage surface of with-meniscus samples. An MRI scan of the post-testing with-meniscus sample also demonstrated no defects of cartilage. The total meniscectomy samples, however, showed obvious damage and loss of cartilage on the articulating surface of both femoral condyle and tibia plateau after friction simulator testing. The partial meniscectomy samples were not proceeded with MRI scans due to the failure of friction simulator tests. Therefore, twelve cartilage samples (femur and tibia) from six total meniscectomy models were scanned on 9.4 Tesla and 3.0 Tesla MRI. For each cartilage sample, four scans were performed at both 9.4T and 3.0T. For each scan, four repeat measurements were performed using the 3D surface reconstruction method for wear quantification study as described in section 2.3.4. In total, 384 measurements were performed in this study as described in Section 4.3.3.

3.3 Results

3.3.1 Generation of cartilage wear

For the with-meniscus and the meniscectomy groups, tests in the pendulum friction simulator were completed without obvious system failure or abnormality. However, during the testing of partial meniscectomy models in the pendulum friction simulator, some abnormal motions of femoral condyle were observed. In most of tests, the condyle pushed the remaining meniscus aside and dropped down onto the tibial cartilage surface. This caused abrupt

drop-down motion of the simulator motion arm and the tibial base was pushed towards the left wall of the simulator. Therefore, only the with-meniscus and the meniscectomy groups had completed the simulation tests.

3.3.2 Wear measurement

The average wear was 10 mm^3 on the femoral condyle and 4 mm^3 on the tibia plateau as shown in Figure 3.11. It should be noticed that the average wear volume demonstrated in the figure was calculated from five meniscectomy models (specimen 01-05.) The wear volume of specimen 06 was excluded because it underwent an extra 3,600 cycles of friction simulator testing prior to MRI scans. However, as a severer wear model the specimen 06 was still used in the MRI study of friction simulator-tested samples in Chapter 4.

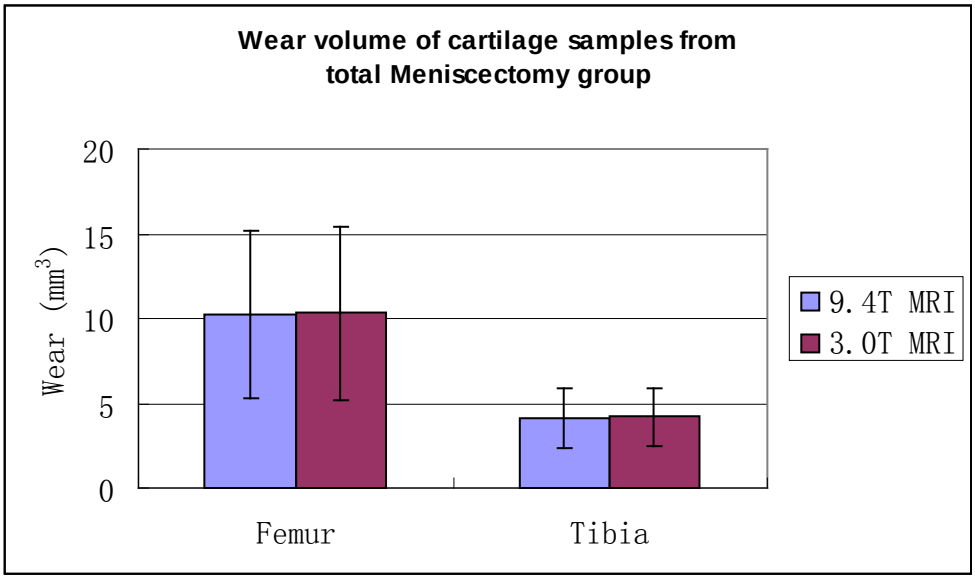

Figure 3.11 Volumes of cartilage defects of meniscectomy samples, measured using 3D surface reconstruction method on 9.4T and 3.0T MRI. Data presented as the average volume ±95% confidence intervals (n=5).

3.3.3 Contact pressure measurement

The X-Rite^{TM} spectrodensitometer measured average density of a fixed window which is a circle area of a diameter of approximately 5mm. The pattern of pink marks differed among the three groups (Figure 3.12). However, the pink mark area on most of the post-testing Fuji film was smaller than the measurement window due to the size of porcine model. This could lead to underestimated contact stress reading by counting in the surrounding white area which had null reading value. Therefore, the contact measurement data was not presented in the result section.

Figure 3.12 Photographs of the Fuji films after a static load of 330N was applied for 15 seconds on three models. (A) Model with intact meniscus, the contact area lay on the meniscus. (B) Model without meniscus, the density of central contact area increased remarkably. (C) Model with the inner 1/3 meniscus removed, the pink marks showed that the tibiofemoral articulation include cartilage-cartilage contact and contact between femoral cartilage with the remaining meniscus.

3.3.4 Friction measurement

The readings acquired during pendulum friction simulator tests of all three groups were recorded. However, mal alignment of the femoral condyle and tibia plateau was possible to occur during tests due to the impingement of geometrical complexity of porcine half knee models, particularly the partial meniscectomy and total meniscectomy models. These could result in incorrect friction measurement. Details will be discussed in Section 3.4. Therefore, the friction simulator readings were not included in this thesis due to less of evidences that these readings were reflecting the pure coefficient of friction (COF) between articular surfaces.

3.4 Discussion

During the testing of partial meniscectomy models in the pendulum friction simulator, some abnormal motions of femoral condyle were observed. In most of tests, the condyle pushed the remaining meniscus aside and dropped down onto the tibial cartilage surface. This could possibly be a result of higher mobility of medial meniscus after dissection. It would be worthy to mention that the outer region of porcine meniscus is much thicker than the inner region. Therefore, the superior articulating surface of the meniscus became medially-laterally discontinuous after resection of over 30% of the inner tissue. This sudden change in contours could directly result in any abnormal motions during the friction testing.

However, the methodology of generation of the in vitro partial meniscectomy model was promising. The partial meniscectomy model was designed in cooperation with Dr Ram Venkatesh who was a consultant Orthopaedic surgeon of Leeds Musculoskeletal Biomedical Research Unit, using the same surgical kits that used in Arthroscopic treatment of knee joint. Together, a series of in vitro meniscal tear models had also been created for the further Tribological study (Figure 3.13).

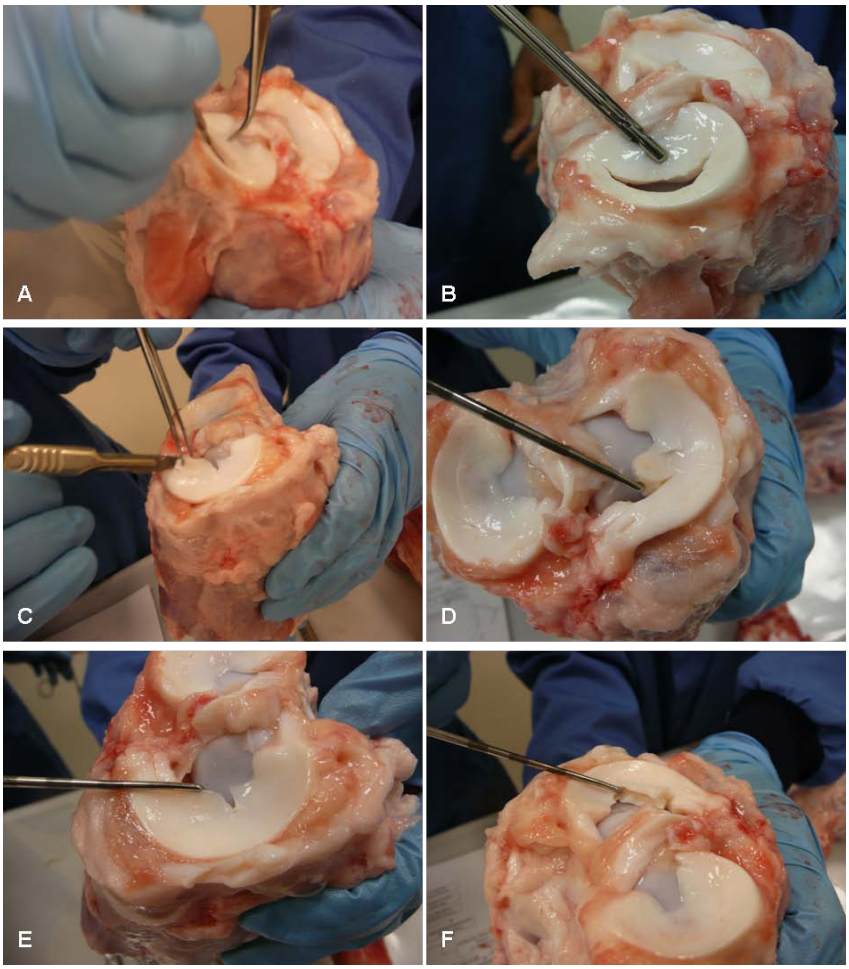

Figure 3.13 Laboratory development of *in vitro* meniscal tear models. (A-B) longitudinal tear; (C-D) flap tear; (E) radial tear; (F) horizontal tear. The tears was created using a scalpel blade and tweezers.

The readings recorded during the pendulum friction simulator testing were not included in this thesis due to several concerns. First of all, the loading profile of pendulum friction simulator testing of porcine specimen lacked direct reference. When designing the loading protocol, no related data was available for porcine models. On the presumption that the pig has similar physiological force transition rate through the knee as other animals such as sheep and cow, two different peak loads were calculated as described in section 3.2.2. The technology applied by Taylor *et al*. (2006) in the determination of tibio-femoral contact force allowed free movement of sheep, thus it has the advantage in the simulation of *in vivo* loading condition. However, the loading force calculated according to Taylor's results was proven to be too high for porcine models. This could possibly be the result of significant inter-model

difference. The sheep used in Taylor's study was musculoskeletally mature animal (two years old). In addition, the sheep was more active in contrast to the pig. Thus the loading force used in this study was calculated based on the bovine data reported from Simon (1970). However, it was still uncertain that the calculated peak load was of physiologically relevant to porcine knee. This could result in additional loading on the porcine model and invalidate the experimental reading.

In addition, the possibility of sample malalignments within the simulation system could not be excluded in this study, particularly the tests of partial meniscectomy and total meniscectomy group. The pendulum friction simulator determines friction torque within the system by measuring the anterior-posterior forces transferred between the fixed frame and the carriage. Malalignments could directly result in internal/external rotation and adduction/abduction (Werner *et al*. 2005), which added unexpected rotation torques on to the friction carriage of the simulator. As a consequence, the transducer could not measure the genuine coefficient and the reading could not be referred as the COF of the articulating surfaces. In this study, the new porcine half knee model kept the entire medial tibiofemoral compartments. Comparing to the previous bovine half knee models, the porcine model had a more irregular bony tibial plateau to articulate the femoral condyle. Though efforts were made to ensure that femur and tibia were articulated in physiologically relevant regions, it was difficult to eliminate the subtle malpositioning of samples, which could result in malalignment load distribution and additional rotation torques within the simulation system. The average reading recorded during the friction simulator testing of the negative control group (with intact meniscus) was 0.03 ± 0.01 (n=6), which was similar to the average COF value reported by McCann *et al*. (2008) using a bovine model. This result to some extent demonstrated the important role of knee meniscus in the joint stabilisation and force distribution.

In conclusion, under a half joint articulation condition with proper lubrication environment, this study successfully created cartilage wear models for the follow-up MRI quantification studies. The introduction of full-scale medial porcine tibiofemoral model without capsule and ligaments to the pendulum friction simulation system was, however, not successful in friction measurement due to the geometrical constraint within the system. The complexity of porcine knee geometry and immaturity of porcine tissue discovered in this study should be considered in the future studies when new whole knee friction simulation systems are available. Using this porcine medial knee model, *in vitro* partial meniscectomy surgery was successfully performed, and a series of meniscal damage/post-meniscectomy models were also laboratorially created, which could be widely applied in the future.

Chapter 4 MRI Quantification of Cartilage Wear

4.1 Introduction

Quantitative morphological Magnetic Resonance imaging of articular cartilage represents not only an efficient diagnostic modality but also a powerful research tool in experimental intervention studies for its non-invasiveness, relatively high precision, high accuracy and 3D delineation capabilities. The spatial resolution, signal-to-noise/ contact-to-noise ratio and acquisition time are crucial parameters in quantitative MRI. In the set-up of an MRI scan, it is noticeable that these imaging parameters are interdependent, *i.e*., improvement of one parameter may require sacrifices of other parameters (Eckstein *et al*., 2006). Koo *et al*. (2005) studied factors such as intra- and inter-observer conditions, which might influence reproducibility and accuracy in quantitative cartilage MRI, and suggested a rule-based approach to improve the reproducibility of MRI cartilage measurement. Studies of Eckstein (2011) and Roemer, *et al*. (2011) suggested MR imaging sequences for cartilage quantitative studies such as cartilage loss measurement, and the spin echo sequences were argued to be not accurate enough for cartilage wear quantification due to issues such as losing MR signal at thin cartilage areas. For physiological safety considerations, most of the current clinical MRI systems are mild-field (0.5 to 3 Tesla). Using these systems, a 250-μm image resolution can generally be achieved (Oei *et al*. 2003; Gold *et al*., 2004; Bencsik *et al*., 2007; Griffin *et al.*, 2008).

An early study of the capability of MR systems in the assessment of cartilage volume and thickness was reported by Sittek *et al.* (1996). They used a low-field (1.0 Tesla) clinical MR system to image one fresh cadaveric knee joint, within 24 hours of explantation following the death of a male individual. The results showed high accuracy in the calculation of cartilage thickness. McGibbon and Trahan (2003) conducted a primary study of MRI measurement of focal cartilage defects, and suggested that 3D GRE imaging sequences could be superior to 2D sequences in the accuracy of

measurement of cartilage defect. Hunter *et al*. (2010) studied human central medial femoral knee cartilage thickness in OA patients with a high risk of rapid medial tibio-femoral progression intervals for the purpose of establishing an imaging biomarker for disease modification in a short time interval.

To date, ultra high field NMR systems (over 7 Tesla) have been utilised in cartilage MRI studies and demonstrated their capability of generation of high quality images with high SNR/CNR and excellent spatial resolution in the order of tens of micrometres (Nieminen *et al.*, 2001; Wang, *et al*., 2008). Overall, advanced modern MRI technology has provided a promising option for quantitative assessment of cartilage status and it would have a great value in high-volume studies of cartilage biotribology and biomechanics.

The specific aim of this project is to develop and verify MRI cartilage wear quantification protocols on an ultra-high field 9.4 Tesla laboratory MRI system and a high field 3.0 Tesla clinical MRI system, using two customised image-based wear volume quantification methods.

4.2 Materials and Instruments

4.2.1 Friction simulator-tested samples

After the friction simulator testing, the porcine femoral and tibial cartilage samples from the meniscectomy group were cut to a smaller size retaining the contacting surface, the size of which was approximately 30 mm in length, 20 mm in width, and 10 mm in depth. This was to fit the cartilage samples into the specimen holder for the 9T MRI scanner as described in Chapter 2.3.2. The cut cartilage samples were wrapped in PBS soaked paper tissues and stored at -20ºC until 6 hours before MRI scans.

4.2.2 Samples for validation study

To validate the MRI wear volume quantification method using Pycnometer, six healthy porcine knees were prepared as described below.

The medial femoral condyle was dissected and cut into the size fitting 9T MRI in the same way as the samples from friction simulator testing. A small piece of cartilage was excised from the articular surface of the condyle using a scalpel blade (Figure 4.1). The small cartilage piece and the remaining major cartilage sample were wrapped in PBS soaked paper tissues and marked separately before storing at -20ºC. The major cartilage sample was thoroughly defrosted for 6 hours before MRI scans.

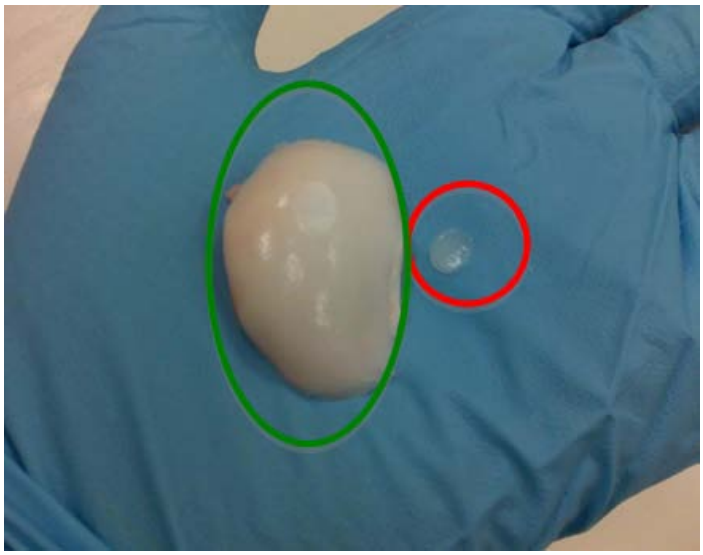

Figure 4.1 Sample preparation for Pycnometer validation study. The small cartilage piece (highlighted by red circle) was for Pycnometer measure, while the remaining sample (highlighted by green circle) was for MRI wear quantification.

4.2.3 MRI scanners

All cartilage samples from both the friction simulator tested group and the Pycnometer validation group were scanned using a 9.4 Tesla Avance^{TM} II 400MHz NMR system and a 3.0 Tesla Siemens Magnetom Verio system. The clinical MRI scanner used in the study was a 3 Tesla Siemens Magnetom Verio system, which located in the NIHR Leeds Musculoskeletal Biomedical Research Unit. The transportation of porcine samples between the university and hospital strictly obeyed the Standard Operation Protocol (SOP.09.9). All samples underwent MRI scanning within one month from the harvest. After thorough defrosting, PBS soaked paper tissues were removed.

4.2.4 Pycnometer

To validate the MRI wear volume quantification method, an AccuPyc 1330 Pycnometer was used. The AccuPyc 1330 is a gas expansion Pycnometer for accurately measuring the volume of solids. A detailed description of Pycnometer validation method was given in Section 2.3.4.

4.3 Methods

4.3.1 MRI of cartilage at 9.4 Tesla

The 2D SE sequence that was used in the previous study (Wang *et al*., 2008) could not provide decent MR images with a slice thickness less than 1 mm. In addition, two-dimensional sequence was not suitable for post-acquisition 3D image analysis. Therefore, the focus of this study was on the other two 3D imaging sequences. Two most commonly applied Musculoskeletal MR imaging sequences, 3D FLASH, and 3D FISP, were studied prior to formal MRI scans of samples.

Two freshly dissected porcine femoral condyles and tibia plateau were cut into the size fitting 9.4T MRI in the same way as the samples from friction simulator testing. A small piece of cartilage was excised from the articular surface of the condyle and tibia using a scalpel blade. Only one sample was scanned each time to minimise the influence of magnetic field inhomogeneity. The cartilage sample (femoral condyle and tibia) was always positioned in the specimen holder with the articulating surface facing laterally. The above-mentioned two defect samples were scanned using 3D FLASH, and 3D FISP, respectively.

The 3D FLASH and 3D FISP sequences both showed high capability of imaging cartilage MRI with good SNR and CNR. In contrast, 3D FISP sequence was superior in terms of shorter acquisition time and fewer image artifacts (Figure 4.2). A series of flip angle of 3D FISP MRI was applied when scanning the same specimen (ranging from x to y). The results showed that best CNR could be achieved at 15 degree of flip angle (Figure 4.3). The optimised parameter settings of 3D FISP MRI of porcine cartilage specimen was finally determined as shown in Table 4.1.

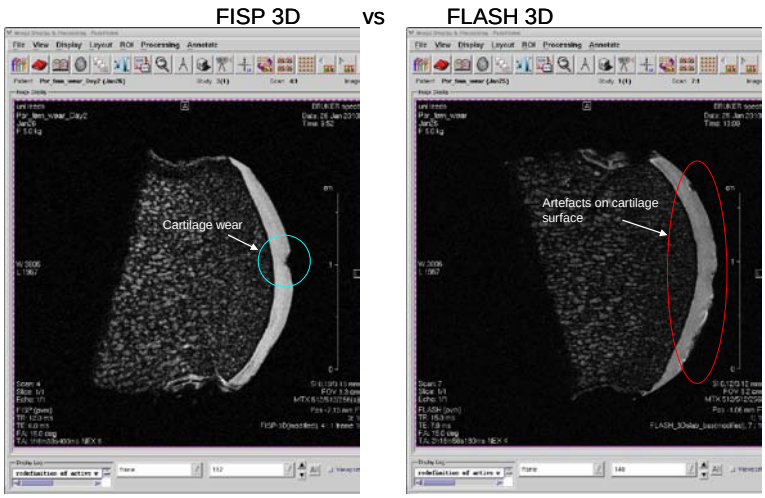

Figure 4.2 Imaging sequence comparison for *in vitro* MRI of porcine medial femoral condyles at 9.4T. The FISP 3D image showed good surface-air contrast with limited artefacts on the cartilage surface. The FLASH 3D image could be affected by artefacts shown in the right image.

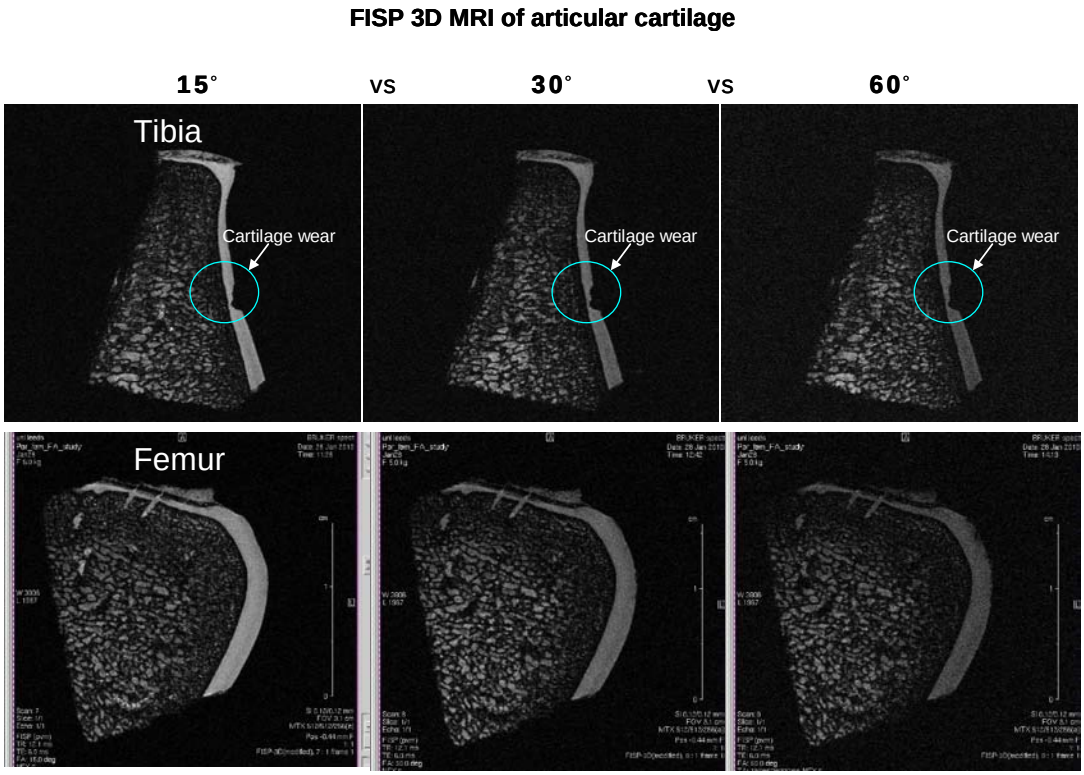

Figure 4.3 FISP 3D MRI of porcine medial tibia and femoral condyle with different settings of flip angle at 9.4T. Optimised image contrast had achieved at 15 degrees flip angle setting.

Each of the specimens was repeatedly scanned four times using the same imaging protocol at 9.4T MRI. To determine the repeatability of 9.4T MRI, the specimen holder was taken out of the magnet and put back in between the repeat scans of the same sample. Therefore, twenty-four 9.4T MRI scans were taken for the validation group study (6 specimens x 4 repeat scans of each), and forty-eight scans done for the friction simulator tested samples (12 specimens x 4 repeat scans).

Table 4.1 Parameter settings of quantitative morphological MRI of cartilage at 9.4T

Echo Time (TE)	6 ms
Repetition Time (TR)	12 ms
FOV	30×30×30 mm
Voxel Size	117×117×234 µm
No. of Average	3
Bandwidth	50 KHz
Flip Angle (degree)	15
Slice orientation	Transverse
Scan Duration	7 m 26 s

4.3.2 MRI of cartilage at 3.0 Tesla

To scan the friction simulator tested cartilage samples, the condyle and tibia samples from the same knee were put in one 25mm diameter specimen holder so the two samples did not overlap each other. Twelve cartilage samples were put in six holders and arranged in a honeycomb-like array using tapes. This allows acquisition of MR images of 12 samples in one scan (Figure 4.4). Using the same method, six samples prepared for Pycnometer validation study were put into five specimen holders and made of a honeycomb-like phantom using tapes.

The phantom of sample was put on the patient table with the tubes in the direction of the main magnetic field (B_0). An 8-element transmit/receive coil was used for imaging. To determine the repeatability of 3.0T MRI, the phantom was twisted clockwise for a random angle in the interval of repeat scans.

Figure 4.4 Photo of 3.0T MRI scan of multiple cartilage samples. Twelve samples were put into 6 holders and arranged in a honeycomb-like array and fixed in a 8-element knee coil, which made it possible to scan multiple samples in one time.

An optimised parameter settings of 3D DESS MRI of porcine cartilage specimen was applied as shown in Table 4.2. Four MRI scans of validation group samples were taken at 3.0T, and another four scans were taken for the study of friction simulator-tested samples.

Table 4.2 Parameter settings of MRI of cartilage at 3.0T

Echo Time (TE)	4.7 ms
Repetition Time (TR)	16.3 ms
In-plane FOV	120×120 mm
In-plane Voxel Size	310×310 μm
No. of Average	1
Flip Angle (degree)	25
Slice orientation	Transverse
Scan Duration	10 m 9 s

4.3.3 MRI quantification of cartilage wear

4.3.3.1 Preparation of image data

The 9.4T images were suitable for direct wear quantification without any processing. The 3.0T images, however, needed segmentation before quantification studies. This is because at 3.0T, multiple samples were scanned at the same time, thus on each 3.0T MR image there were multiple objectives. It was preferred that on each image there was only one object for wear quantification, thus all 3.0T MR image stacks were segmented using Analyze™ prior to quantification of wear volume as shown in Figure 4.5, B.

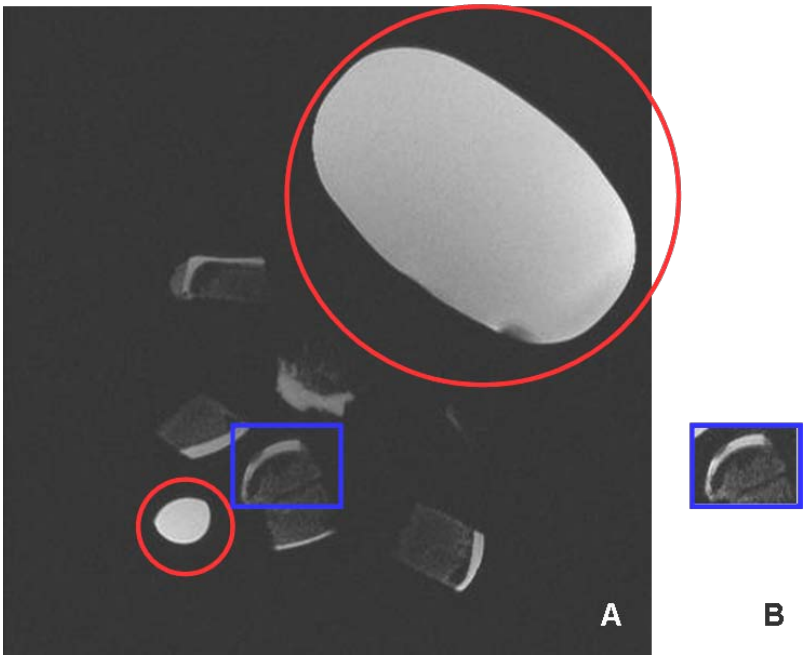

Figure 4.5 An MR image extracted from 3.0T MRI of cartilage samples. (A) Image showed multiple samples. The objects highlighted by red circle were 0.9% (w/v) sodium chloride solution which was used to enhance the MR signal. The blue square highlighted a femoral condyle. (B) The femoral condyle was segmented using Analyze™ for wear quantification.

Two MRI-based wear quantification methods, a MATLAB™ 2D profile method and an ITK-SNAP 3D surface reconstruction method, were used in this study for comparison.

4.3.3.2 The 2D profile method

The 2D profile method was adapted from previous studies (Wang *et al.*, 2008; McCann *et al.*, 2010). It required the observer to load one slice of MR images at a time, to perform curve fitting on the cartilage surface to determine the area of cartilage wear using a MATLAB^{TM} code. Since the voxel dimension was known, the volume of worn cartilage was calculated for each slice (Figure 4.6). The overall volume of cartilage wear was calculated by adding up the results of all slices.

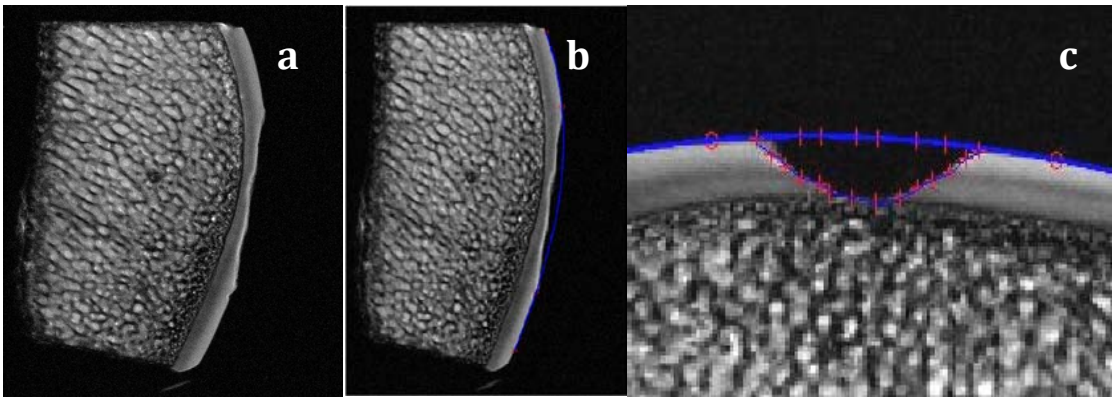

Figure 4.6 MRI quantification of cartilage wear using a 2D profile method. a) A representative 2D MR image slice shows visible wear on the bovine femoral cartilage surface; b) A curve-fitting done by a MATLAB^{TM} code; c) Wear region definition for wear volume quantification.

4.3.3.3 The 3D surface reconstruction method

A customised ITK-SNAP programme with a second graphical user interface (GUI) allowed the user to calculate the whole wear volume of a specimen at one time.

Major features of this 3D method include reading, reconstructing, segmenting the MR image volume in a 3D manner. The ITK-SNAP prompted the user to reconstruct the 3D volume of MR images, a '*.xyz' file was generated when the user manually selected the wear region on the 3D volume. The original '*.xyz' file was translated into a '*.r' file for image regression using R program,

and a new '*.xyz' file was generated. This new '*.xyz' file was loaded into the ITK-SNAP to generate a virtual 3D surface which simulated the unworn cartilage surface and it was located on the worn surface. The volume of worn cartilage could be calculated using the GUI. An example of the 3D volume measurement is shown in Figure 4.7.

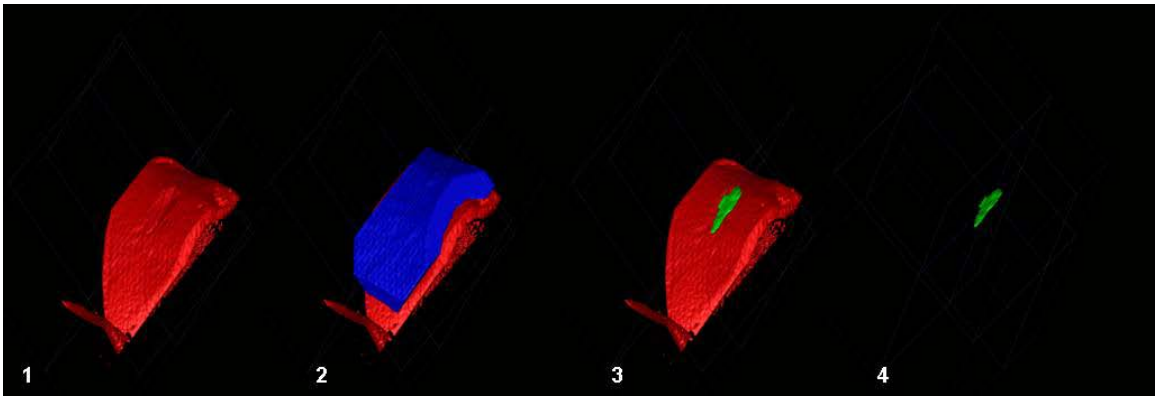

Figure 4.7 Illustration of a 3D wear volume measurement. 1) Reconstruction of worn cartilage surface. 2) A virtual 3D surface was generated on the worn surface, 3-4) The 3D wear volume was extracted and could be calculated.

4.3.3.4 Study design

In the study of validation group, both the 2D profile method and 3D surface method were applied on all sample images (9.4T and 3.0T). Through out the whole study, each specimen was scanned for four times, and four repeat measures were done for each scan. Therefore, for each specimen from validation group, 64 measures were done as outlined in Table 4.2. In total, the validation study of all 6 samples took 384 measures. The counterpart of each cartilage sample was repeatedly measured for four times in a Pycnometer as described in Section 2.3.4.

Table 4.3 MRI wear quantification study design of specimen number one of the validation group.

	Specimen	MRI	Repeat of MRI scan	Method of Measure	Repeat of Measure	Total number of measures
Validation Study	1	9.4T	x4	Surface 3D	x4	16+16+16+16 =64
				Profile 2D	x4	
		3.0T	x4	Surface 3D	x4	
				Profile 2D	x4	

In the study of friction simulator-tested group, only 3D surface method was used. Twelve cartilage samples (femur and tibia) were scanned for four times both at 9.4T and at 3.0T, and four repeat measures were done for each scan. Therefore, 32 measurements were done for each sample, since 16 measurements (4 scans × 4 repeat measures) were done at 9.4T, and another 16 measurements were done at 3.0T. In total, 384 measurements were done for 12 cartilage samples from simulator-tested group.

4.4 Results

The cartilage defect was visible on both 9.4T and 3.0T MRI. Representative MR images of cartilage samples at 9.4T and 3.0T were shown in Figure 4.8.

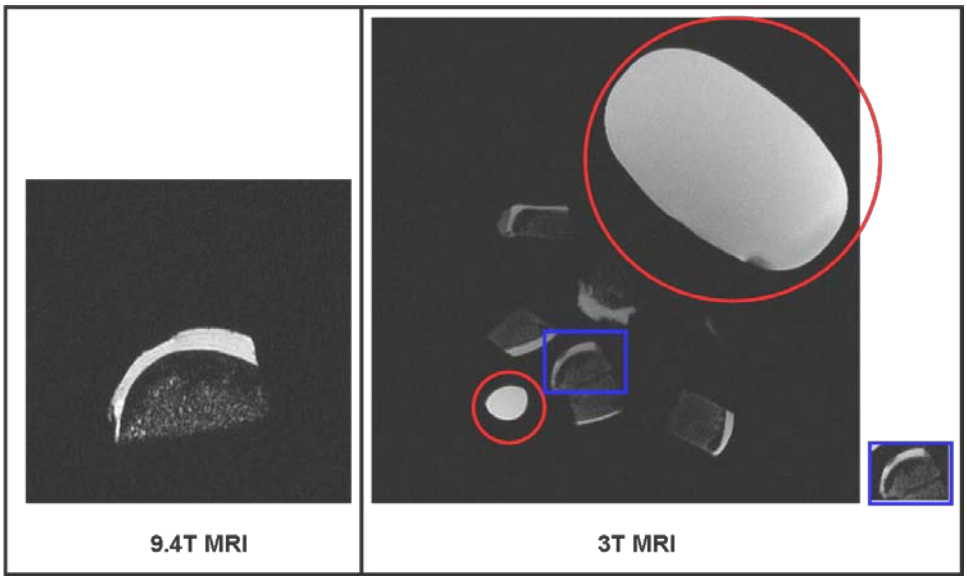

Figure 4.8 Representative image slices of quantitative morphology MRI of cartilage at 9.4T (left image) and 3.0T (right image). The objects highlighted in red circles were bags of 0.9% (w/v) sodium chloride solution. The 9.4T MR image had obvious superior spatial resolution (8.5 pixels per mm) and contrast to the 3.0T MRI (3.2 pixels per mm), though cartilage defect was visible on both images.

4.4.1 Validation Group

4.4.1.1 Wear measurement on 9.4 Tesla MR Images using 3D surface method

The average volume of cartilage wear of specimens from validation study, measured on 9.4T MRI using 3D surface reconstruction method is shown in Figure 4.9 and 4.10. In Figure 4.9, data was presented as the average of each four repeat measurements of a same scan.

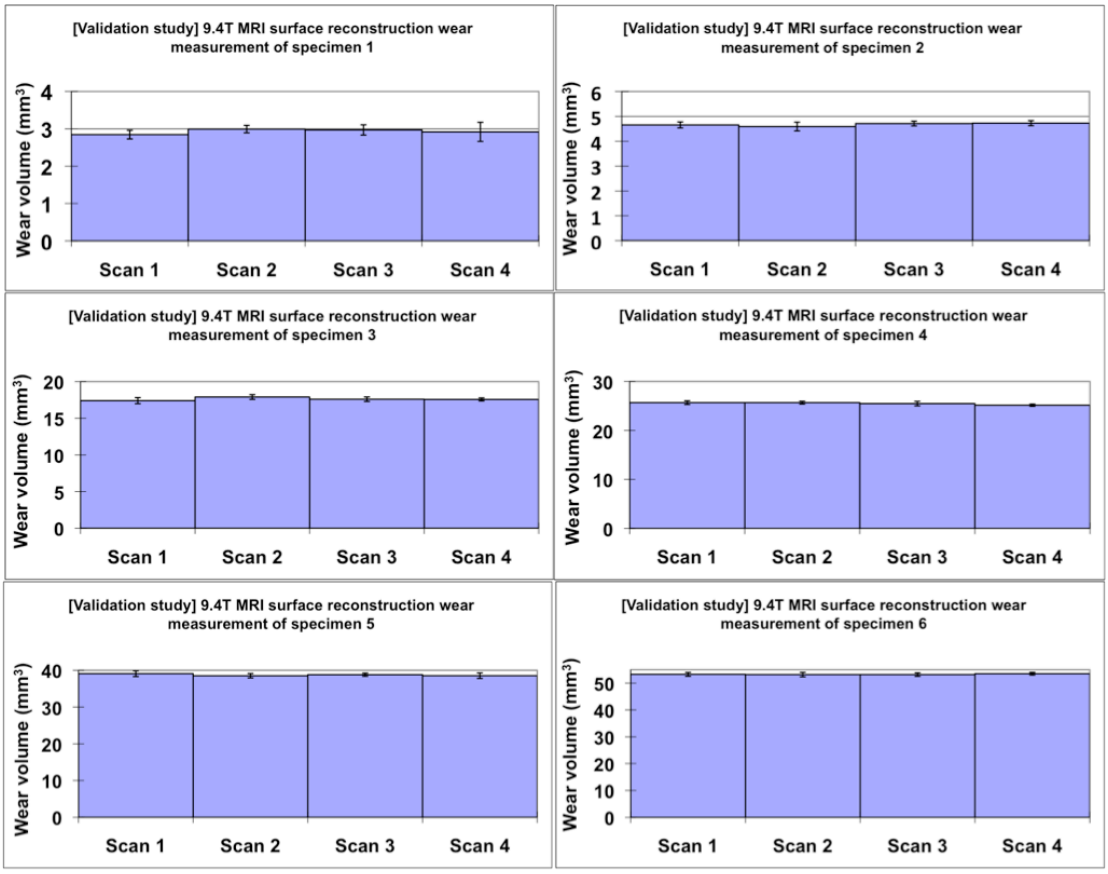

Figure 4.9 Volumes of cartilage defects of 6 validation samples, measured using 3D surface reconstruction method on 9.4T MRI. Data presented as the average volume ±95% confidence intervals (n=4 repeat measurements using same image). N.B., the scale of wear volume axis varies among individual charts.

The coefficient of variation (CV) of each four repeat measurements using the same MRI scan is shown in Table 4.4. The 3D surface reconstruction method showed low variation in wear measurement if the same 9.4 Tesla MRI scan was used, with an average CV = 2%.

Table 4.4 Coefficient of variation of measurement using 3D surface reconstruction method on 9.4T MRI, among repeat measurements for each scan. Each MRI scan was used for four repeat measurements. The CV value in this table represent the coefficient of variation calculated among each set of 4 repeat measurements using a same MRI scan.

Coefficient of variation- among 4 repeat measurements using a same scan (9.4T MRI, 3D surface reconstruction method)				
	CV of Scan1	CV of Scan2	CV of Scan3	CV of Scan4
Spe01	4%	3%	5%	9%
Spe02	3%	4%	2%	2%
Spe03	2%	2%	2%	1%
Spe04	2%	1%	2%	1%
Spe05	2%	2%	1%	2%
Spe06	1%	2%	1%	1%

The average volume of cartilage wear measured using four repeat MRI scans is shown in Figure 4.10.

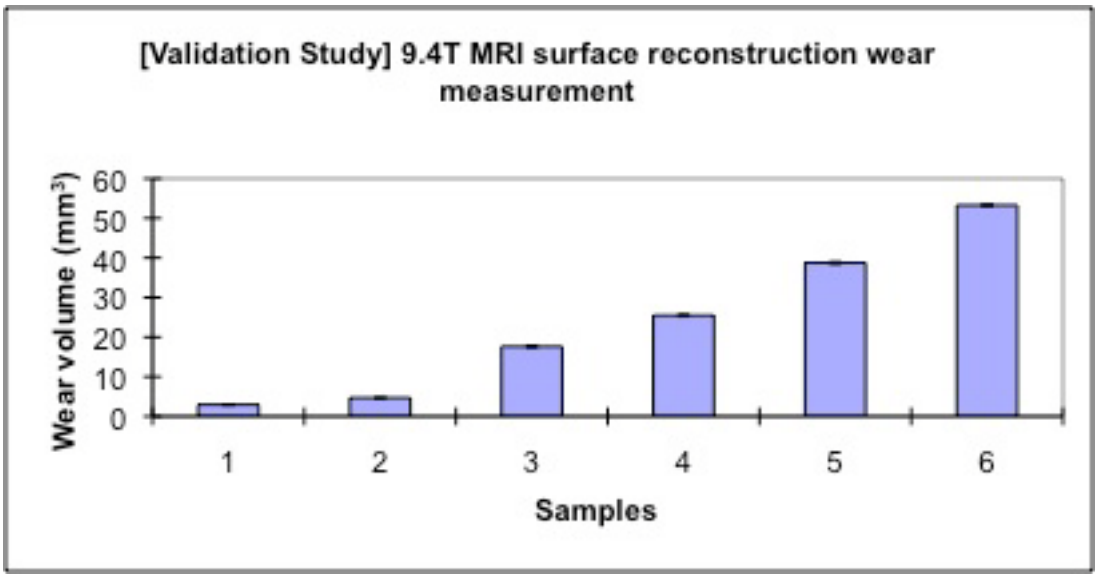

Figure 4.10 Volumes of cartilage defects of validation samples, measured using 3D surface reconstruction method on 9.4T MRI. Data presented as the average volume ±95% confidence intervals (n=4 repeat scans of each specimen).

The CV of average wear volumes of four MRI repeat scans of each specimen was shown in Table 4.5.

Table 4.5 Coefficient of variation of measurement using 3D surface reconstruction method on 9.4T MRI. The CV value in this table represent the coefficient of variation calculated among each set of 4 MRI scans of the same specimen.

Coefficient of Variation- among 4 MRI scans of the same specimen (9.4TMRI, surface reconstruction method)	
Spe01	2%
Spe02	1%
Spe03	1%
Spe04	1%
Spe05	1%
Spe06	0%

4.4.1.2 Wear measurement on 9.4 Tesla MR Images using 2D profile method

The average volume of cartilage wear of specimens from the validation study, measured on 9.4T MRI using 2D profile method is shown in Figure 4.11 and 4.12. In Figure 4.10, data was presented as the average of each four repeat measurements of a same scan. The coefficient of variation (CV) of each four repeat measurements using a same MRI scan is shown in Table 4.6. The 2D profile method showed low variation in wear measurement if the same 9.4 Tesla MRI scan was used, with an average CV = 2%.

Table 4.6 Coefficient of variation of measurement using 2D profile method on 9.4T MRI, among repeat measurements for each scan. The CV value in this table represent the coefficient of variation calculated among each set of 4 repeat measurements using a same MRI scan.

Coefficient of variation- among 4 repeat measurements using a same scan (9.4T MRI, 2D profile method)				
	CV of Scan1	CV of Scan2	CV of Scan3	CV of Scan4
Spe01	7%	5%	1%	1%
Spe02	5%	2%	3%	1%
Spe03	3%	1%	3%	1%
Spe04	1%	1%	3%	3%
Spe05	2%	3%	2%	2%
Spe06	0%	0%	0%	0%

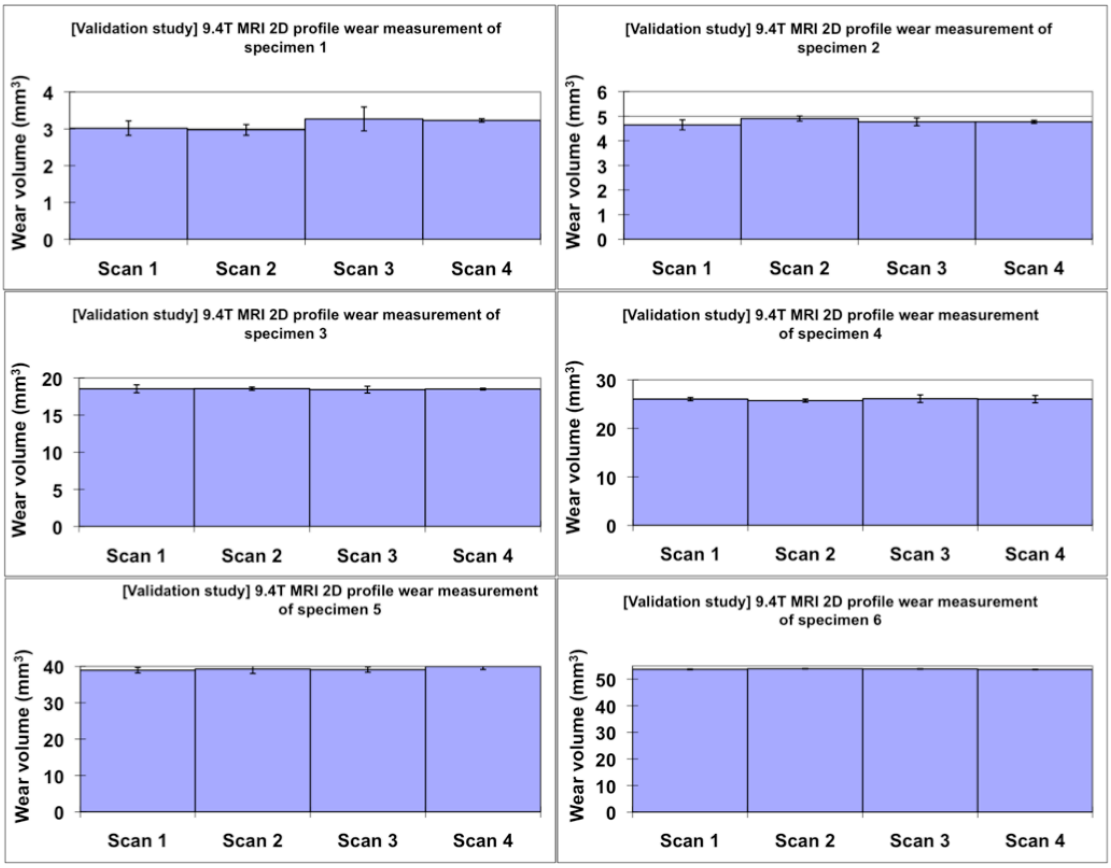

Figure 4.11 Volumes of cartilage defects of 6 validation samples, measured using 2D profile curve fitting method on 9.4T MRI. Data presented as the average volume ±95% confidence intervals (n=4 repeat measurements using same image). N.B., the scale of wear volume axis varies among individual charts.

The average volume of cartilage wear measured using four repeat MRI scans is shown in Figure 4.12.

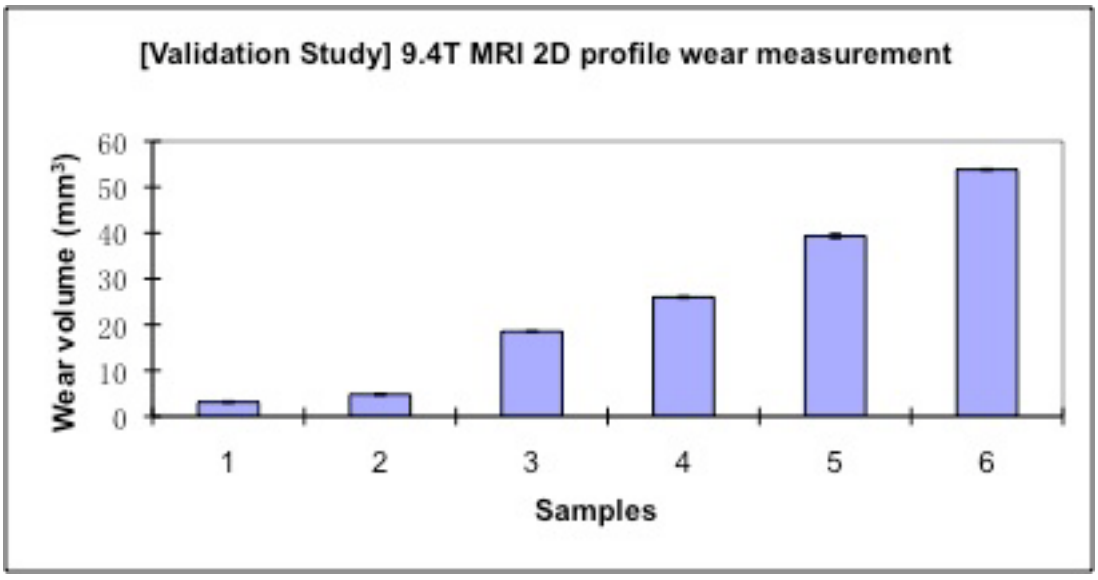

Figure 4.12 Volumes of cartilage defects of validation samples, measured using 2D profile method on 9.4T MRI. Data presented as the average volume ±95% confidence intervals (n=4 repeat scans of each specimen).

The CV of average wear volumes of four MRI repeat scans of each specimen was shown in Table 4.7.

Table 4.7 Coefficient of variation of measurement using 2D profile method on 9.4T MRI. The CV value in this table represent the coefficient of variation calculated among each set of 4 MRI scans of the same specimen.

Coefficient of Variation- among 4 MRI scans of the same specimen (9.4TMRI, 2D profile method)	
Spe01	5%
Spe02	2%
Spe03	0
Spe04	1%
Spe05	1%
Spe06	0

4.4.1.3 Wear measurement on 3.0 Tesla MR Images using 3D surface method

The average volume of cartilage wear of specimens from validation study, measured on 3.0T MRI using 3D surface reconstruction method is shown in Figure 4.13 and 4.14. In Figure 4.13, data was presented as the average of each four repeat measurements of a same scan. The coefficient of variation (CV) of each four repeat measurements using a same MRI scan is shown in Table 4.8. The 3D surface reconstruction method showed low variation in wear measurement if the same 3.0 Tesla MRI scan was used, with an average CV = 3%.

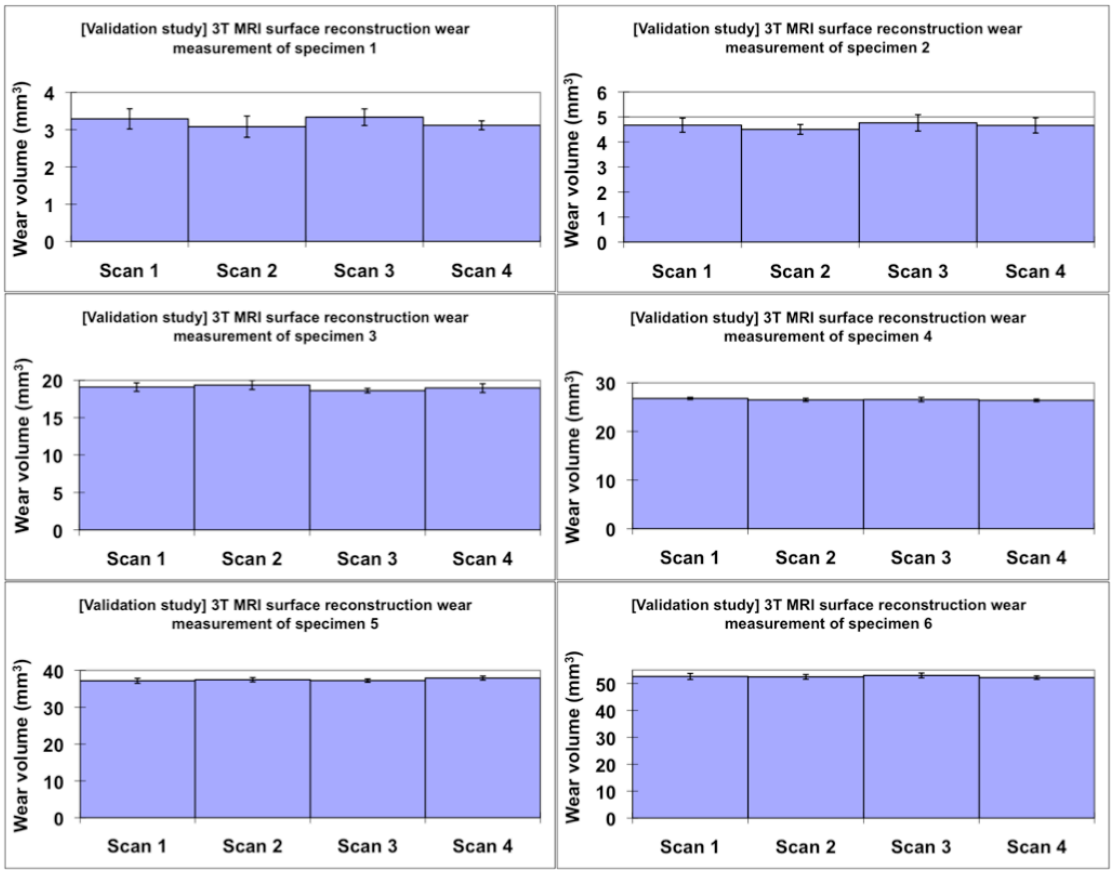

Figure 4.13 Volumes of cartilage defects of 6 validation samples, measured using 3D surface reconstruction method on 3.0T MRI. Data presented as the average volume ±95% confidence intervals (n=4 repeat measurements using same image). N.B., the scale of wear volume axis varies among individual charts.

Table 4.8 Coefficient of variation of measurement using 3D surface reconstruction method on 3.0T MRI, among repeat measurements for each scan. The CV values in this table represent the coefficient of variation calculated among each set of 4 repeat measurements using a same MRI scan.

Coefficient of variation- among 4 repeat measurements using a same scan (3.0T MRI, 3D surface reconstruction method)				
	CV of Scan1	CV of Scan2	CV of Scan3	CV of Scan4
Spe01	8%	9%	7%	4%
Spe02	6%	4%	7%	7%
Spe03	3%	3%	2%	3%
Spe04	1%	1%	2%	1%
Spe05	2%	2%	1%	1%
Spe06	2%	2%	2%	1%

The average volume of cartilage wear measured using four repeat MRI scans is shown in Figure 4.14.

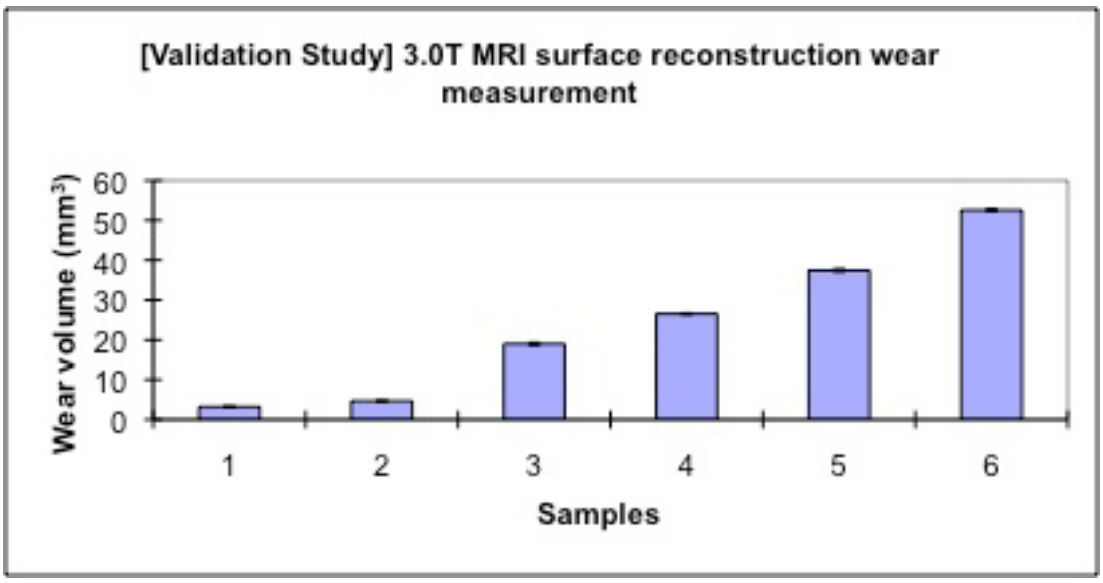

Figure 4.14 Volumes of cartilage defects of validation samples, measured using 3D surface reconstruction method on 3.0T MRI. Data presented as the average volume ±95% confidence intervals (n=4 repeat scans of each specimen).

The CV of average wear volumes of four MRI repeat scans of each specimen was shown in Table 4.9.

Table 4.9 Coefficient of variation of measurement using 3D surface reconstruction method on 3.0T MRI. The CV value in this table represent the coefficient of variation calculated among each set of 4 MRI scans of the same specimen.

Coefficient of Variation- among 4 MRI scans of the same specimen (3.0TMRI, surface reconstruction method)	
Spe01	4%
Spe02	2%
Spe03	2%
Spe04	1%
Spe05	1%
Spe06	1%

4.4.1.4 Wear measurement on 3.0 Tesla MR Images using 2D profile method

The average volume of cartilage wear of specimens from validation study, measured on 9.4T MRI using 2D profile method is shown in Figure 4.15 and 4.16. In Figure 4.15, data was presented as the average of each four repeat measurements of a same scan.

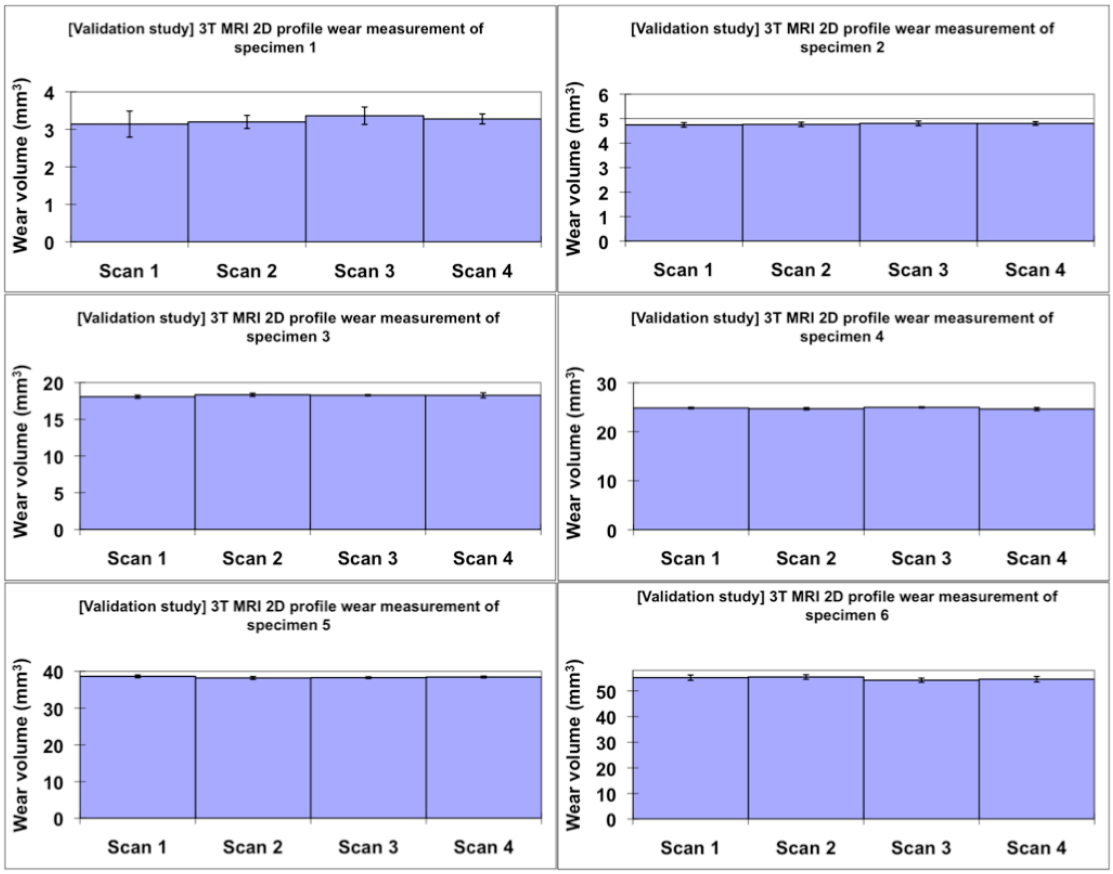

Figure 4.15 Volumes of cartilage defects of 6 validation samples, measured using 2D profile curve fitting method on 3.0T MRI. Data presented as the average volume ±95% confidence intervals (n=4 repeat measurements using same image). N.B., the scale of wear volume axis varies among individual charts.

The coefficient of variation (CV) of each four repeat measurements using a same MRI scan is shown in Table 4.10. The 2D profile method showed low variation in wear measurement if the same 3.0 Tesla MRI scan was used, with an average CV = 2%.

Table 4.10 Coefficient of variation of measurement using 2D profile method on 3.0T MRI, among repeat measurements for each scan. The CV value in this table represent the coefficient of variation calculated among each set of 4 repeat measurements using a same MRI scan.

Coefficient of variation- among 4 repeat measurements using a same scan (3.0T MRI, 2D profile method)				
	CV of Scan1	CV of Scan2	CV of Scan3	CV of Scan4
Spe01	11%	6%	7%	4%
Spe02	2%	2%	2%	2%
Spe03	1%	1%	1%	2%
Spe04	1%	1%	1%	1%
Spe05	1%	1%	1%	1%
Spe06	2%	2%	2%	2%

The average volume of cartilage wear measured using four repeat MRI scans is shown in Figure 4.16.

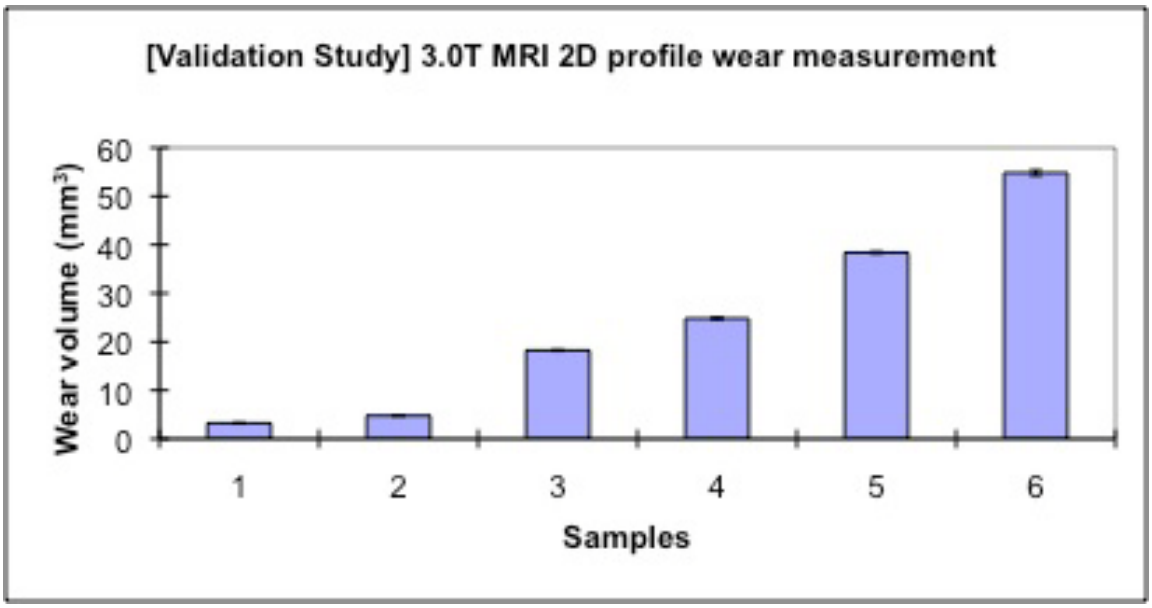

Figure 4.16 Volumes of cartilage defects of validation samples, measured using 2D profile method on 3.0T MRI. Data presented as the average volume ±95% confidence intervals (n=4 repeat scans of each specimen).

The CV of average wear volumes of four MRI repeat scans of each specimen was shown in Table 4.11.

Table 4.11 Coefficient of variation of measurement using 2D profile method on 3.0T MRI. The CV value in this table represent the coefficient of variation calculated among each set of 4 MRI scans of the same specimen.

Coefficient of Variation- among 4 MRI scans of the same specimen (3.0TMRI, 2D profile method)	
Spe01	3%
Spe02	1%
Spe03	1%
Spe04	1%
Spe05	0
Spe06	1%

4.4.1.5 Validation of MRI measurement of cartilage wear

The average volume of cartilage wear of specimens from validation study, measured on both 9.4T MRI and 3.0T MRI was compared to the Pycnometer readings of the counterpart of each specimen (Table 4.12).

Table 4.12 The average volume of cartilage wear of specimens from validation group. Data presented as the mean of 4 repeat scans ± SD (standard deviation).

	Spe01	Spe02	Spe03	Spe04	Spe05	Spe06
9.4T surface (n=4)	2.93±0.07	4.68±0.06	17.61±0.21	25.48±0.25	38.74±0.27	53.28±0.16
9.4T profile (n=4)	3.12±0.15	4.78±0.11	18.51±0.06	25.98±0.17	39.33±0.45	53.82±0.14
3.0T surface (n=4)	3.21±0.13	4.65±0.11	19±0.32	26.53±0.17	37.45±0.34	52.57±0.34
3.0T profile (n=4)	3.24±0.1	4.78±0.03	18.24±0.11	24.81±0.15	38.39±0.19	54.82±0.56
Pycnometer (n=4)	2.83±0.05	4.58±0.1	17.9±0.14	25.8±0.16	39.15±0.17	52.58±0.15

The precision and accuracy of MRI-based cartilage wear quantification methods were compared to Pycnometer measurement using Lin's concordance correlation coefficient (Lin, 2008) and coefficient of determination. As shown in Figure 4.17, four combinations of MRI and image-based volume quantification methods all represented precise and accurate agreement. The concordance correlation coefficients and R^2 values of 9.4T MRI-3D surface measure, 9.4T MRI-2D profile measure, 3.0T MRI-3D surface measure, and 3.0T MRI-2D profile measure were 0.9997 and 0.9996, 0.9994 and 0.9997, 0.9987 and 0.9979, 0.9982 and 0.9971, respectively.

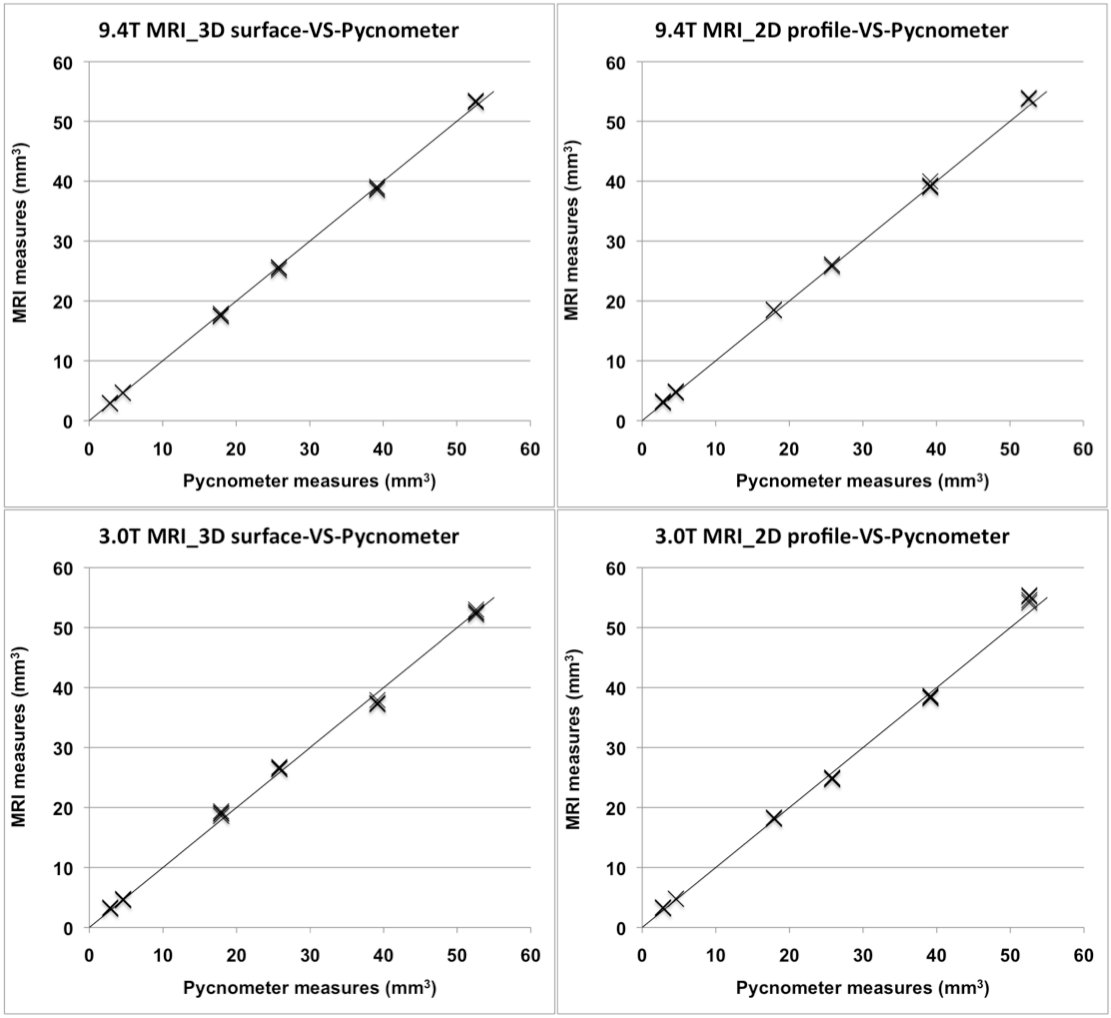

Figure 4.17 Validation of MRI quantification of cartilage loss by Pycnometer. Four separate charts showed the results of four combinations of MRI and volume quantification methods. For each sample, data presented as MRI measurements (n= 4 repeat scans) versus the mean value of Pycnometer measurement.

4.4.2 Friction Simulator-tested Group

4.4.2.1 Comparison between the with-meniscus group and total meniscectomy group

After the friction simulator testing, the samples were checked immediately. No visible wear could be found on the cartilage surface of with-meniscus samples. MRI scans of the post-testing with-meniscus sample also demonstrated no defects of cartilage. The total meniscectomy samples, however, showed obvious damage and loss of cartilage on the articulating surface of both femoral condyle and tibia plateau after friction simulator testing. Therefore, all of the samples from the total meniscectomy group were scanned on 9.4 Tesla and 3.0 Tesla MRI. The acquired MR images were analysed using the 3D surface reconstruction method for wear quantification study.

4.4.2.2 MRI wear quantification of samples underwent meniscectomy

The average volume of cartilage wear of specimens from total meniscectomy group, measured on 9.4T and 3.0T MRI using 3D surface reconstruction method is shown in Figure 4.18.

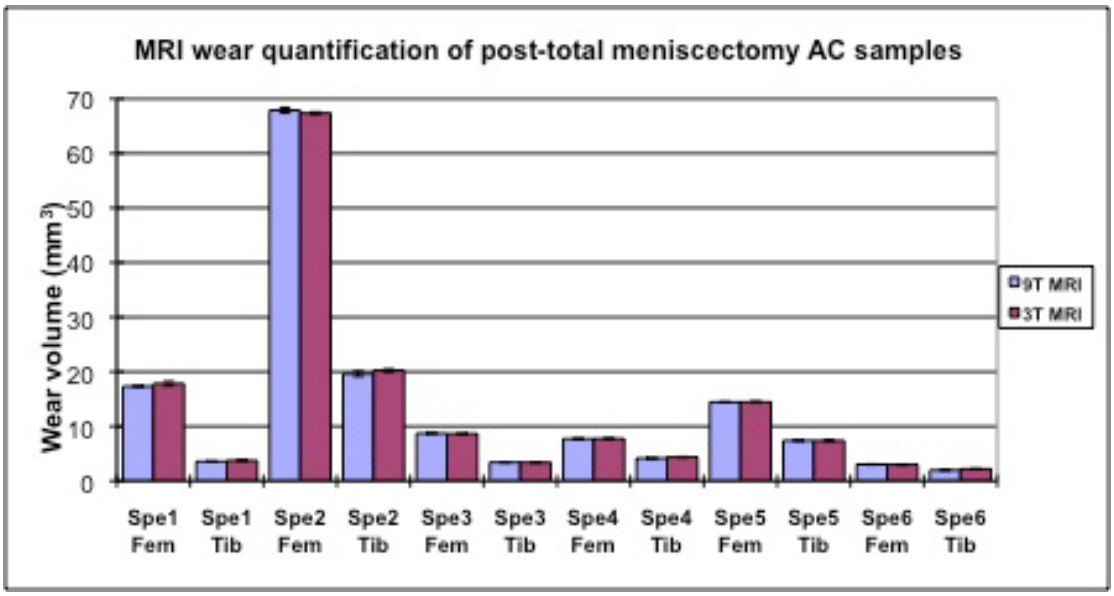

Figure 4.18 Volumes of cartilage defects of meniscectomy samples, measured using 3D surface reconstruction method on 9.4T and 3.0T MRI. Data presented as the average volume ±95% confidence intervals (n=4 repeat scans of each specimen).

A paired t-test was performed to determine if the cartilage wear quantification at 9.4T and 3.0T MRI showed significant difference. The two tail p value =0.315, providing evidence that the cartilage wear quantification based on 9.4T and 3.0T MRI had no significant difference. A 95% confidence interval about mean difference between 9.4T and 3.0T is (0.0, 0.16 mm^3).

4.5 Discussion

MRI cartilage wear quantification is a non-destructive method for quantitative assessment of cartilage wear. In high-volume studies of cartilage tribology, it was important to measure the cartilage loss after experiments. It has been shown that ultra-high field MRI was capable of providing high quality images for in vitro quantification of cartilage loss (McCann *et al*, 2009). However, the 9.4T scanner had narrow magnet bore which only allowed examination of small samples. Therefore, to exam a large range of animal/human tissues such as whole knee joint used in the biomechanical and biotribological experiments, the *in vitro* MRI cartilage wear quantification method should be also applicable on the clinical system. In this study the samples were cut into

a small size in order to fit into the 9.4T laboratory MRI system, but they were also scanned on a 3.0T clinical system for the first time. The images acquired at both 9.4T and 3.0T were used for measures of void in cartilage surface. The results were compared with the accurate volume of the cartilage pieces removed from the samples, to verify the wear quantification methods derived from MRI.

Considering the shortest dimension of the cartilage surface is in the transverse plane, the cartilage sample (femoral condyle and tibia) was always positioned in the specimen holder with the articulating surface facing laterally, with slice orientation was always set to be axial, i.e., aligned with the main magnetic field, to achieve optimal delineation (Peterfy *et al*, 2006). The influence of sample positioning in the magnet was also studied by twisting the sample during the interval between four repeat scans. The coefficient of variation among four repeat scans was reasonably low for all methods, ranged from 0 to 5%, which suggested good repeatability of MRI-based measurement methods. In the validation study only femoral condyles were used. This was because of the convex shape of condyle, from which the surface cartilage could be easily cut rather than the concave shape of tibia plateau. In addition, the porcine condyle had thicker cartilage than the tibia, which allows extraction of different amount of cartilage without damaging the whole cartilage layer.

When applying 3.0T MRI of cartilage samples, insufficient MR signal could be generated by the samples themselves. Therefore, 0.9% (w/v) sodium chloride solution was used as extra media during the scan. It could be seen on Figure 4.5 that these solutions generated very high MR signals and showed extremely bright on MR images. If the NaCl solution was put into the sample holders, the contrast of the interface between cartilage surface and solution was inferior to that of the interface between cartilage and air. In addition, the NaCl solution could also result in cartilage swelling if been allowed to contact the cartilage sample directly. Therefore, the NaCl solutions were sealed in

separate bags/tubes which boosted the signal while not influencing the natural conditions of cartilage samples.

The two MRI-based methods for the determination of cartilage wear volume were in excellent agreement with each other. The MATLAB^{TM} 2D profile method might have involved more human error than 3D surface reconstruction method, especially in the definition of wear regions. The 2D profile method required manual selections of wear regions on each image slice, though a pre-created spline curve was used as a guideline as shown in Figure 4.6. In contrast, the 3D surface reconstruction method did not require manual determination of wear regions. However, extreme care was still required when adjusting image contrast limits before the fully automatic region definition procedure. This is because the patterns of cartilage wear were noticeably different between the simulator tested-samples and manually created damage models. Unlike the manually created sample which had smooth and regular boundary of the void of cartilage, the simulator generated wear could have irregular appearance, particularly the margin of wear could have non-functional cartilage residuals attached. These cartilage residuals showed similar MR signals to healthy cartilage. If they could not be excluded from volume of healthy cartilage, the volume of worn cartilage would be underestimated. To effectively exclude the signals from cartilage residuals, determination of image contrast limit might be one of the important factors, especially for 3D surface reconstruction method, since the residuals could have different signal intensity.

The time efficiency had to be considered in the selection of measurement methods in the future study. The 2D profile quantification method required the observer to load one MR image slice at a time, and it took at least one minute to complete the measurement of one slice. In this study, 3D high resolution MRI was applied at 9.4T, which generate an image stack of 128 image slices for a small porcine cartilage sample, with detectable wear on one third of the slices. Therefore, the average time of completing a 2D profile-based

measurement was over 40 minutes. The MRI acquired at 3.0T, however, had lower spatial resolution, and on only one or two images the wear could be measurable, *i.e.*, it only take less than five minutes if using the profile-based method to measure a sample at 3.0T MRI. Unlike the 2D profile quantification method, the 3D surface reconstruction method had almost fixed time of measurement of approximately 20-25 minutes. It should be noticed that the author had practiced both methods for a long period (>6 months), therefore, the consistency of intra-observer measures could be possibly higher than that of observers who were new to the methods. In the future research, it is suggested that an inter-observer study would be of value to study the extent of human errors in the measurement. Researchers should also choose the measurement method in the context of image spatial resolution in the slice direction to achieve optimised time efficiency.

The AccuPyc 1330 Pycnometer is a helium gas displacement Pycnometer. It computed the sample volume by discharging the pressures initially observed on the sample chamber into an expansion chamber. Therefore, the device involves gas flow during the measurement and it requires the samples to be dried prior to measurement for ideal readings. However, a totally dried cartilage sample would shrink in size and had reduced volume. In this study, cartilage pieces were measured in Pycnometer in natural condition, though the consistently reduced Pycnometer readings showed unavoidable dehydration of sample among four repeat measurements. The device also requires the samples to occupy at least two-thirds of the sample chamber for an accurate measurement. The actual volume of the smallest sample chamber available was 12 cc, i.e., the samples needed to be at least 8 cc to be accurately measured, thus the two stainless steel spheres and an additional large cartilage piece were introduced. Other methods such as tap density measurement could also be used in the future studies. The tap measurement involved obtaining the tapped volume of an amount of the powder, then adding the cartilage piece under test to the pycnometric powder, followed by tapping once more (Figure 4.19). This method should be able to further minimise the sample dehydration during measurement. The reason

that this tap measurement method was not included in this study is because no pycnometric powder was available in the laboratory, and some common powders such as flour was proven to be unsuitable for the Pycnometer use after a trial test.

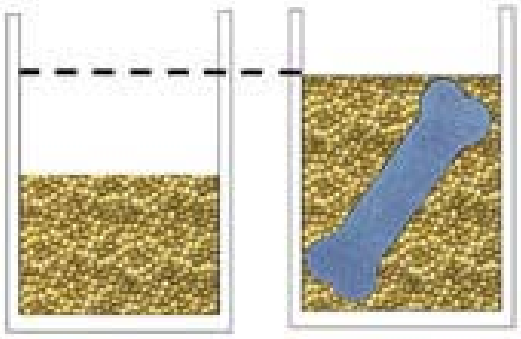

Figure 4.19 Illustration of the tap density measurement method. Website of the ceramicindustry, last accessed in Oct 2011. http://www.ceramicindustry.com/CDA/Archives/9511b4e6b7b29010VgnVCM100000f932a8c0

In conclusion, *in vitro* MRI quantification of biotribologically tested porcine cartilage samples were for the first time compared between an ultra high field 9.4T MRI system and a 3.0T clinical MRI system. The MRI was sensitive to cartilage loss at both magnetic field strengths. The two MRI-based measure methods demonstrated good consistency with very low variation, and very good agreement was also found between methods. Overall, MRI wear quantification showed excellent agreement of the precise and accurate volume measurement of Pycnometer, demonstrated that MRI was a useful tool in biomechanics and biotribology to undestructively investigate the cartilage loss as a result of physiologically relevant simulation experiment.

Chapter 5. MRI Examination of the Meniscal Architecture

5.1 Introduction

The majority of known meniscal functions such as load bearing and transmission, shock absorption and joint stabilisation are determined by the interaction between fluid phase and solid phase (Messner and Gao, 1998; Schumacher *et al*., 2005; McDermott and Amis, 2006; McDermott *et al*., 2008). The internal architecture of menisci is made of uniquely organised solid components such as fibril bundles and networks as described in section 1.1.1.1. Disruption to the architecture as a result of degradation or trauma may affect the integrity of the extracellular matrix (ECM) organisation, shear stiffness, shear stress and resistance to tensile hoop stresses. This could result in loss of function and compromise the tribological performance.

General MR imaging protocols employ an Echo Time (TE) of between 9 to 20 ms. Using this range of TE, the normal knee meniscus appears homogeneously dark, in other words, there is a very low or no signal on the image, irrespective of the pulse sequences been used. This is due to the fact that meniscus tissue has a very short T_2 relaxation time, which means that the meniscal signal completely decays before the signal acquisition. Clinically an intrameniscal high signal could be treated as tear, mucoid degeneration, or vascularity (Aichroth *et al*., 1992; Takeda *et al*., 1998). It can be of significant value to develop methods that can investigate the internal structure of meniscus, and hence can differentiate abnormalities from normal structure and characterise meniscal lesions.

To highlight the meniscus, a technique called Ultra-short TE (UTE) can be used, typically employing a TE of between 0.08 to 0.2 ms, which is capable of demonstrating the menisci with a much brighter signal (Gatehouse *et al.*, 2004). Omoumi, *et al*. (2010) optimised imaging sequences such as T2 SE

and Ultra-short TE with fat saturation in a series of 3.0T MRI scans of cadaveric human menisci, and concluded that the optimal TE for visualisation of the meniscal infrastructure ranged from 3 to 6 ms.

Ultra-high-field (UHF,≥ 7 Tesla) MRI of the knee has been increasingly attracting scientific interests, in both the research domain using laboratory systems and the clinical application using whole-body systems. Some pioneer studies of *in vivo* ultra-high-field MRI of musculoskeletal system has shown the advantages of using higher magnetic field strength: higher intrinsic signal to noise ratio (SNR), higher spatial resolution, higher contrast between tissues (Pakin *et al*., 2006; Regatte *et al*., 2007).

In the field of biological and medical engineering, an understanding of the biomechanical and tribological properties of the knee meniscus and cartilage (*e.g*., contact stress and friction of the articulating surfaces) and their correlation with tissue degeneration and degradation such as wear and tear are important in research and development of therapies for knee diseases.

To detect and characterise lesions, and to investigate tissue structural changes as a consequence of mechanical or tribological experiments, a non-invasive and high-resolution imaging technique is needed. Since a few researchers have reported the progress on MRI of intrameniscal signals (Wang *et al*., 2010; Omoumi *et al*., 2010), the essential demand of using meniscal MRI in this project is to develop an optimised imaging protocol on both 9.4- and 3.0- Tesla MRI systems, to delineate intrameniscal structure and meniscal tears in order to improve the understanding of the correlation between intrameniscal structure and meniscal functions.

5.2 Materials and Methods

5.2.1 Materials

5.2.1.1 Animal menisci samples

Porcine menisci sample was prepared as described in Section 2.2.2 and Section 2.3.2.

5.2.1.2 Human cadaver menisci samples

One formalin-prepared and one PBS-prepared human cadaver medial menisci samples from the Leeds GIFT Tissue Bank were scanned using a 9.4 Tesla MRI scanner. The human menisci were prepared at the St James Hospital. Some basic information of the cadaver menisci was shown in Table 5.1.

Table 5.1 Information of human cadaver menisci samples

Patient No.	Gender	Age	Height	Weight (kg)	Sample Condition
G21/9R	Female	44	5’2”	55	Fresh
G24/10L	Female	85	5’7”	29.21	In formalin
G27/10R	Female	88	5’6”	38.1	In formalin

They were then transported between the NMR laboratory and the hospital through the NHS transportation. Each meniscus sample was sealed in a standard 25mm sample container and was not taken out of the container during the set up for MR scanning.

5.2.1.3 The MRI scanners

Two MR imaging systems were used in this project: a 9.4 Tesla Bruker Avance^{TM} II 400MHz laboratory NMR system and a 3.0 Tesla Siemens Magnetom Verio system (at temperature of 22 ± 0.6 ºC) (Figure 5.1).

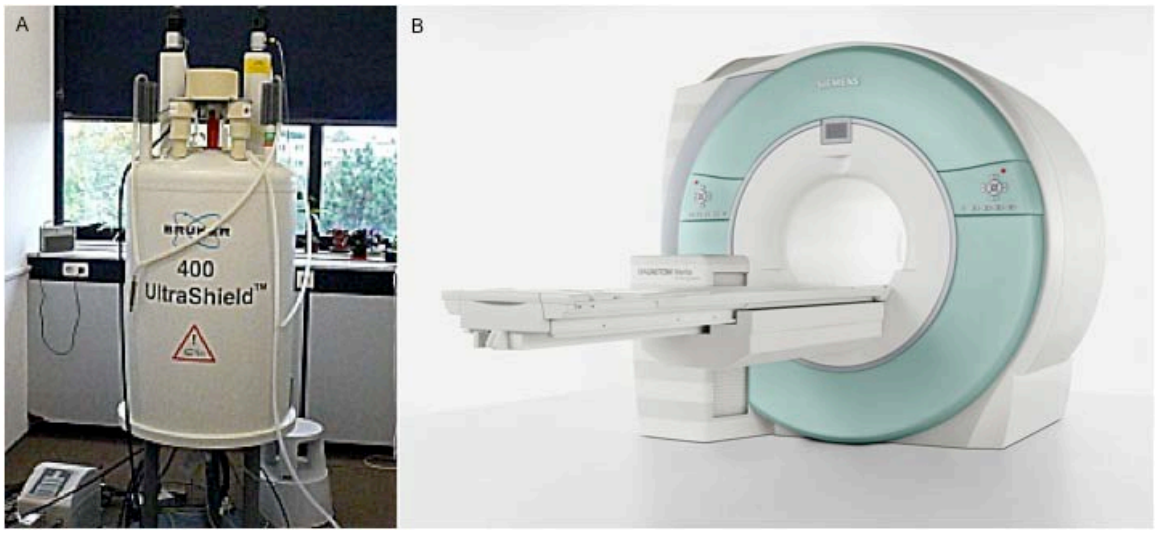

Figure 5.1 Photos of MRI scanners used in this project. A) Bruker Avance II laboratory 9.4 Tesla MRI scanner in the School of Physics, University of Leeds. B) Siemens Magnetom Verio 3 Tesla scanner in the Leeds Musculoskeletal Biomedical Research Unit, Chapel Allerton Hospital, Leeds.

5.2.2 Methods

5.2.2.1 Ultra-High-Field MRI

The 9.4 Tesla MRI has been performed on 23 porcine menisci and 2 human cadaver menisci. The following imaging protocols were modified and applied in this study: Spin Echo (SE), Fast Low Angle Shot (FLASH) 3D, and Fast Imaging with Steady-state Precession (FISP) 3D. To minimise the influence of tissue dehydration, each meniscus sample was only scanned once using one of the above-mentioned imaging sequences. Geometrically, two directions of scan were applied as shown in Figure 5.2.

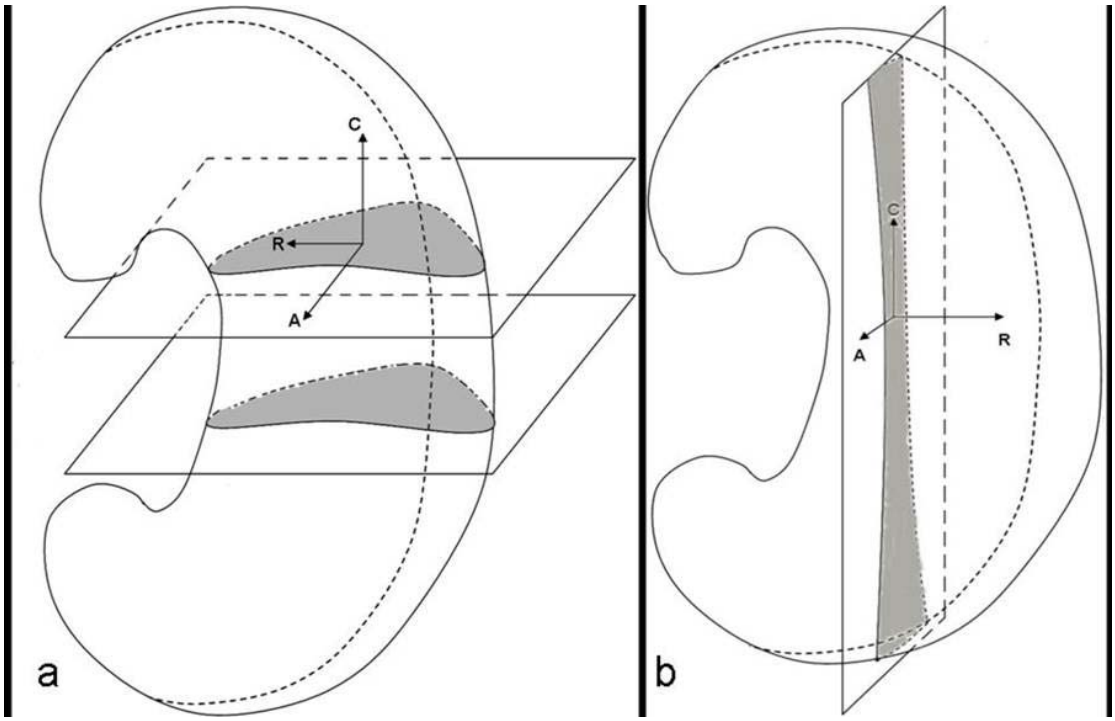

Figure 5.2 Illustration of the geometry setting of MR scans of menisci. The meniscus was put vertically in the magnet with the femoral surface towards front and the posterior horn towards the bottom. (a) Scans in the transverse orientation. (b) Scans in the sagittal orientation. (C: circumferential, R: radial, A: axial)

Meniscal MRI experiments started with a conventional Spin Echo proton-density-weighted imaging sequence, which was one of the most commonly employed imaging sequences in clinical MRI of the knee, Modified FLASH 3D and FISP 3D sequences were studied with the purpose of optimising image spatial resolution, isotropy and other indexes. The core parameter settings of representative MRI scans are shown below in Table 5.2- 5.4.

Table 5.2 Parameter settings of 9.4T Spin Echo MRI of menisci

Spin Echo (SE) of porcine medial menisci		
Echo Time (TE)	10 ms	7.9 ms
Repetition Time (TR)	1200 ms	4000 ms
FOV	30×30×10 mm	25×25×40 mm
Voxel Size	51×51×1000 µm	43×43×1000 µm
No. of Average	10	1
Bandwidth	200 KHz	200 KHz
Flip Angle (degree)	180	180
Slice orient	Transverse	Transverse
Scan Duration	1 hr 42 m	5 hr 41 m

Table 5.3 Parameter settings of 9.4T 3D FLASH MRI of menisci

3D FLASH of porcine medial menisci							
Echo Time (TE)	3.0 ms	3.3 ms	7.9 ms	7.9 ms	5.4 ms	3.7 ms	7.9 ms
Repetition Time (TR)	30.9 ms	190 ms	50 ms	100 ms	76.9 ms	280.9 ms	65 ms
FOV	3×3×3.6 cm	2.8×2.8×1.3cm	2.2×2.2×0.6cm	2.2×2.2×0.54 cm	2.2×1.4×3.2cm	2.4×2.4×1.2cm	3.3×3.3×1.65cm
Voxel Size	59×78×281 µm	55×73×203 µm	43×43×100 µm	43×43×84 µm	43×36×125 µm	23×31×187 µm	64×64×64 µm
No. of Average	4	8	8	18	7	1	15
Bandwidth	1 MHz	454.5 KHz	50 KHz	50 KHz	98.68 KHz	555.6 KHz	50 KHz
Flip Angle (degree)	30	30	30	30	30	30	30
Slice orient	Transverse	Transverse	Transverse	Transverse	Transverse	Transverse	Sagittal
Scan Duration	1 hr 41 m	10 hr 22 m	3 hr 38 m	16 hr 23 m	14 hr 41 m	3 hr 50 m	35 hr 30 m

Table 5.4 Parameter settings of the 9.4T FISP 3D MRI of menisci

FISP 3D of porcine medial menisci		
Echo Time (TE)	6 ms	6 ms
Repetition Time (TR)	12 ms	12 ms
FOV	4×4×6.4 cm	3×3×3.2 cm
Voxel Size	78×78×500 µm	59×59×249 µm
No. of Average	2	8
Bandwidth	50 KHz	50 KHz
Flip Angle (degree)	60	60
Slice orient	Transverse	Transverse
Scan Duration	13 m 37 s	55 m 2 s

5.2.2.2 Clinical MRI at 3.0 Tesla

One porcine medial meniscus was scanned at 3.0 Tesla MRI to investigate the ability of mid-field MRI of demonstrating intrameniscal structures.

The meniscus sample was immersed in 0.9% (w/v) sodium chloride solution and sealed in the 25mm diameter tube and was put vertically on the patient table. Two 4-channel loop “surface” coils were used for imaging (Figure 5.3). A series of routine clinical knee MRI protocols were applied. Without moving the sample, one standard 2D turbo spin echo (TSE) and two optimised 3D double echo steady state (DESS) and 3D FLASH scans were performed. The detailed protocols and parameter settings are shown in Table 5.5.

Figure 5.3 Photo shows the setting up of 3.0T MRI of a meniscus sample. The two 4-channel loop surface coils were overlapped and with their loops surrounding the sample holder to achieve best image quality.

Table 5.5 Parameter settings of the 3.0T MRI of porcine menisci

	2D TSE	3D DESS	3D FLASH
Echo Time (TE)	25 ms	4.7 ms	7.57 ms
Repetition Time (TR)	4930 ms	16.3 ms	20 ms
FOV	8.5×8.5 cm	5.2×10.5 cm	12×12 cm
Voxel Size	274×274×1000 µm	338×273×300 µm	234×234×500 µm
No. of Average	1	8	2
Slice orient	Transverse	Transverse	Transverse
Scan Duration	8 m 43 s	40m 49 s	22 m 18 s

5.2.2.3 Post-acquisition image analysis

The signal-to-noise ratio (SNR) and relative contrast (ReCon) of meniscal MR images was measured as described in Section 2.3.3.

5.2.3 Histology of MRI-examined samples

Four MRI-examined porcine meniscus samples with markers on the surface were fixed, dissected made into histologically stained slices by the methods described in 2.3.5. The Sirius Red, Collagen IV and H&E staining sections, and MRI findings of the same position of same samples were compared.

5.3 Results

5.3.1 UHF MRI of the meniscus

The intrameniscal structure could be observed on all 9.4 Tesla MRI of porcine menisci (Figure 5.4). The 2D Spin Echo proton-density-weighted images had less sharpness than the other two 3D protocol images, while the 3D FISP images had lowest SNR and also showed some artefacts. The 3D FLASH MRI allowed fine delineation of intrameniscal structures with limited artifact and high signal-to-noise ratio (SNR), high contrast-to-noise ratio (CNR), good relative contrast (ReCon) and high image spatial resolution (Figure 5.5). A 16-h FLASH 3D scan achieved a fine in-plane spatial resolution (43×43 μm) with the mean SNR value of 16.4 with a standard deviation of 1.34. The images from a 33-h scan have a spatial resolution of 47×47×86 μm with the mean SNR of 40.58 with a standard deviation of 1.74.

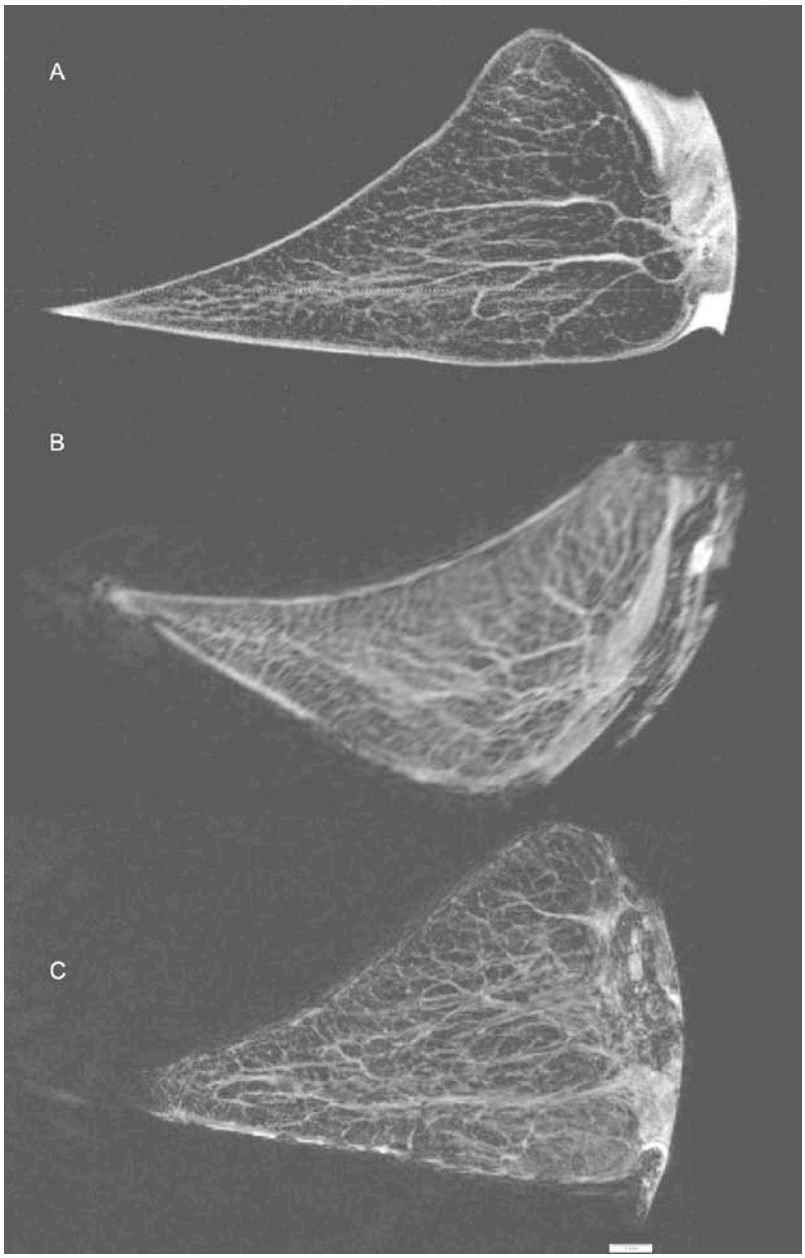

Figure 5.4 Two-dimensional image slices from 9.4T MRI of porcine menisci. A) 2D SE, spatial resolution 43×43×1000 µm, SNR 38, scan duration 5hr41m; B) 3D FISP, spatial resolution 78×78×500 µm, SNR 22, scan duration 13m37s; C) 3D FLASH, spatial resolution 43×43×84 µm, SNR 39, scan duration 16hr23s. The intrameniscal signal could be seen on all three images. The SE and FLASH had higher image SNR and sharpness than the short FISP scan, more detailed information of internal architecture could be seen on the 3D FLASH images.

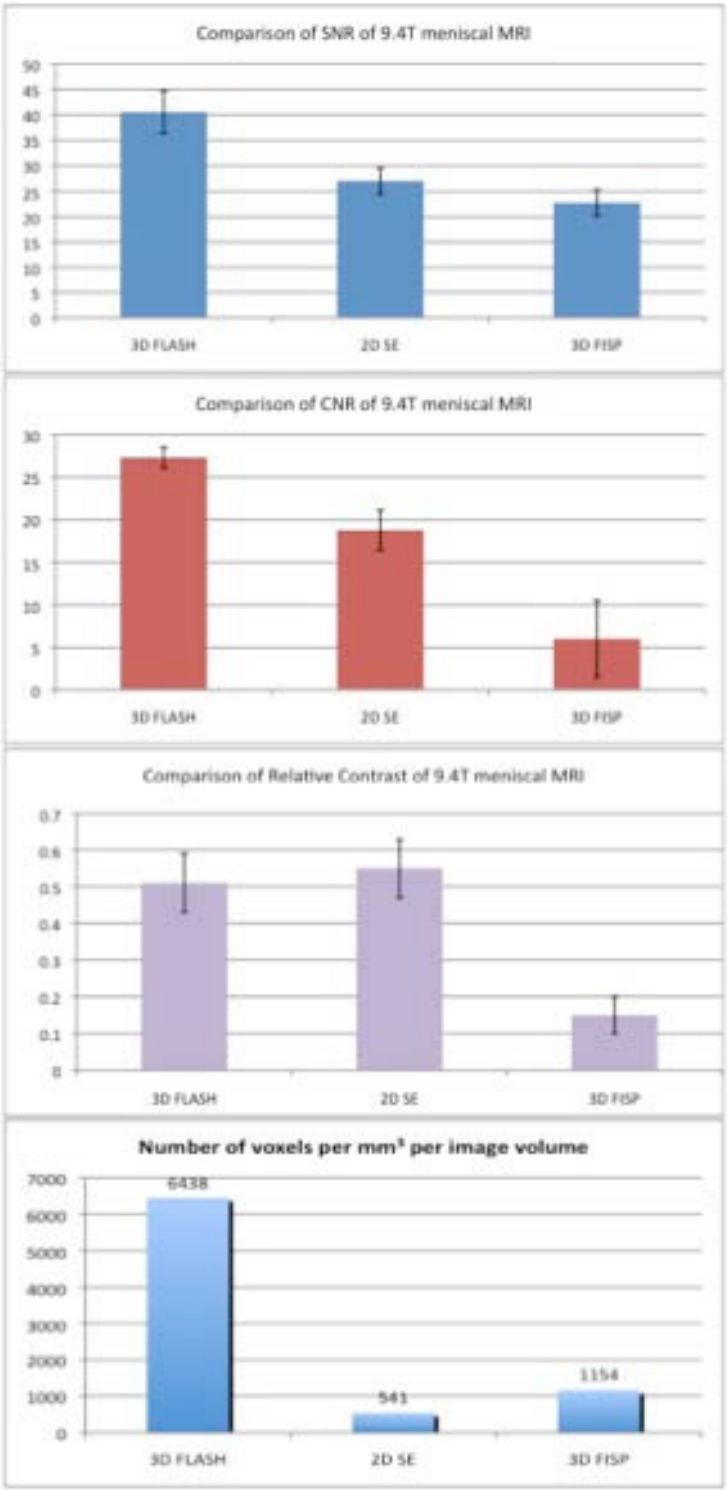

Figure 5.5 SNR, CNR, Relative contrast, and Voxel number per cubic millimeter of three MRI sequences. For SNR, CNR and ReCon, data presented as mean (n=6)±SD of six selected images from each sequence. For voxel number per cubic millimeter, the finest voxel from each sequence was used- 3D FLASH, 43×43×84 μm; 2D SE, 43×43×1000 μm; 3D FISP, 59×59×249 μm.

The 2D spin echo protocol could achieve a fine in-plane spatial resolution of 43×43 µm, however, the image slice was 1 mm thick. Attempts to reduce slice thickness down to the range of 100-500 µm were not successful because the consequent images were overwhelmed by noises. Therefore, the definition of 2D image was seriously lowered if the image depth was taken into consideration.

Since the modified FLASH 3D imaging sequences showed better capabilities of delineating intrameniscal structures compared with the other two sequences, the majority of MRI experiments were carried out based on the modified 3D FLASH imaging protocol. The ideal echo time (TE) for imaging the meniscal tissue on 9.4 Tesla was ranged between 3.0 to 9.7 ms. A 50 KHz receiver bandwidth was sufficient. However, in some cases the bandwidth was manually increased to lower the TE into the above-mentioned range. As consequence, the SNR was reduced. Adjusting other parameter settings such as use a prolonged TR could increase SNR but this could also increase acquisition time. Therefore, for each scan a specific set of parameters were applied. Some of the representative images of 3D FLASH scans were shown in Figure 5.7.

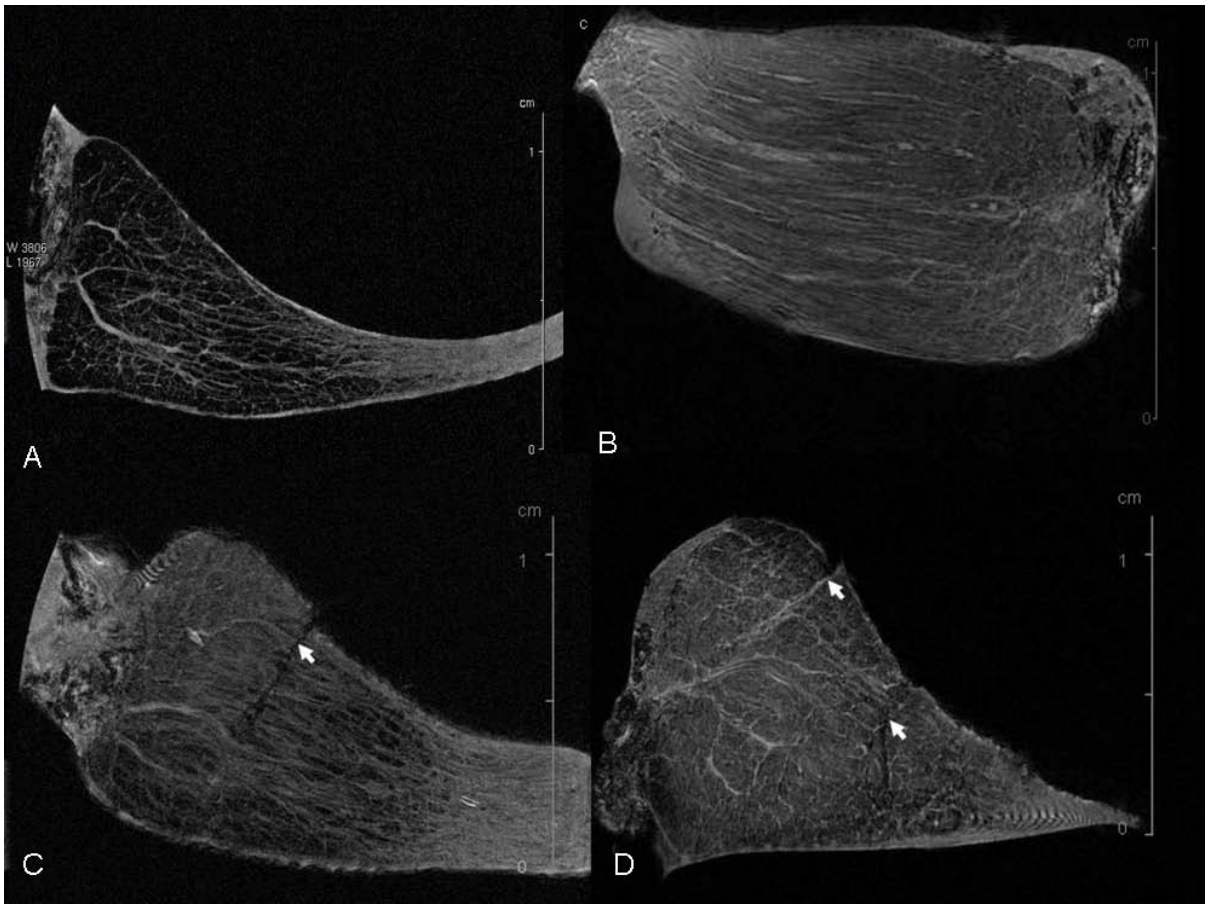

Figure 5.7 Two-dimensional MR images extracted from a series of 3D FLASH MRI scans showed the internal structure of porcine knee menisci. (A) Transverse view showed the radially arranged structure. Spatial resolution, 43×43×84 µm. (B) Sagittal view showed the circumferentially arranged structure. Spatial resolution, 59×59×312 µm. (C, D) Cross-sectional view showed tears and disruption of networks of the meniscal tissue (arrows). Spatial resolution, Image C: 43×43×125 µm; Image D: 47×47×86 µm.

To interpret the MR image findings, histological staining sections of the same sample were made after MRI. The fine network of high signal lines within the meniscal tissue (Figure 5.7, 5.8B) showed an appearance similar to the radially oriented tie fibers and the circumferentially oriented fibers that have been observed on the Sirius Red staining (Figure 5.8 A) and the H&E staining (Figure 5.8C). The Collagen IV staining revealed the distribution of most of the blood vessels. It could be seen that most of the vessels were in the inner half with a few of them stretched into the outer half (Figure 5.9A). In comparison with the Collagen IV staining, the 9.4T MR images demonstrated more structures, which showed high consistency with the fibrous architectures.

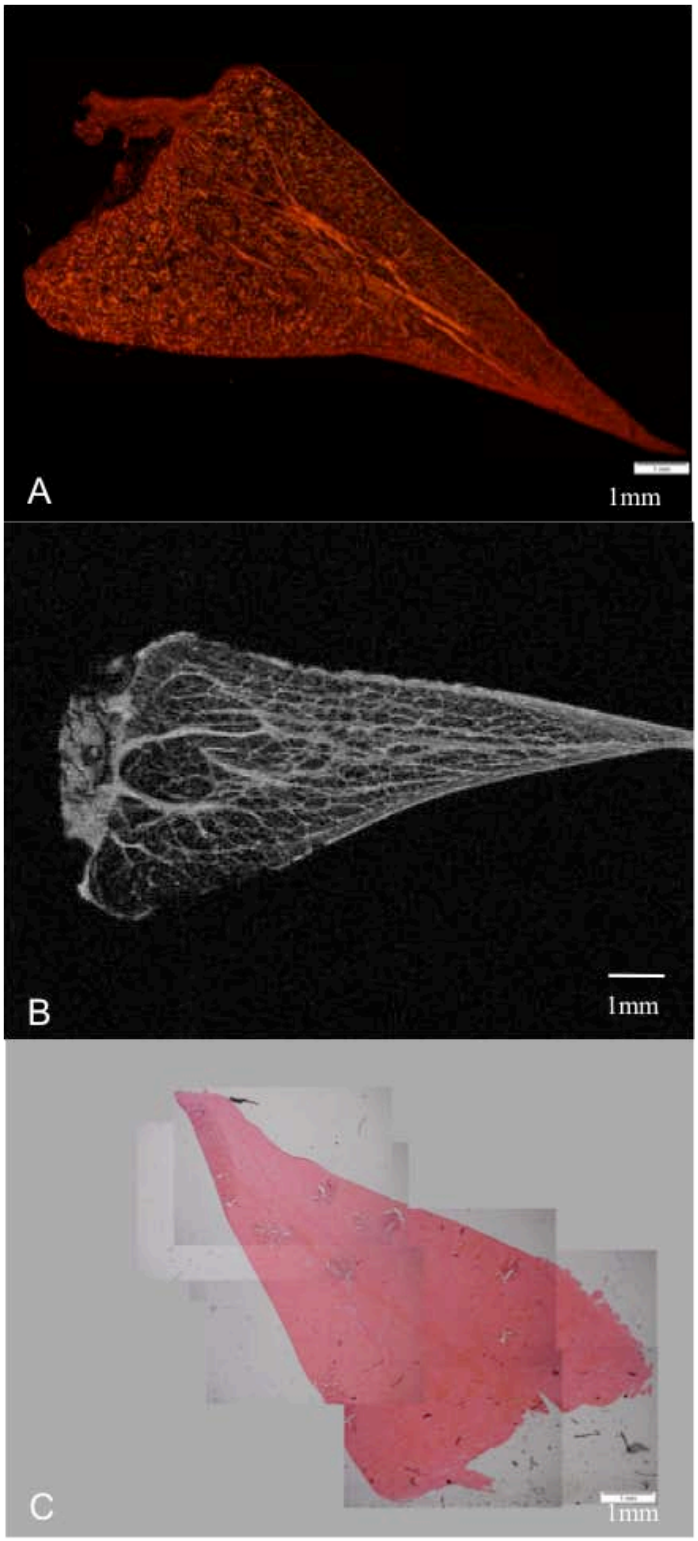

Figure5.8 Comparison between MR image and histological staining sections in fibrous architecture. (A) Sirius Red staining section, all types of collagen were stained; (B) MRI at 9.4T; (C) H&E staining section showed stain of cells and major intrameniscal architectures.

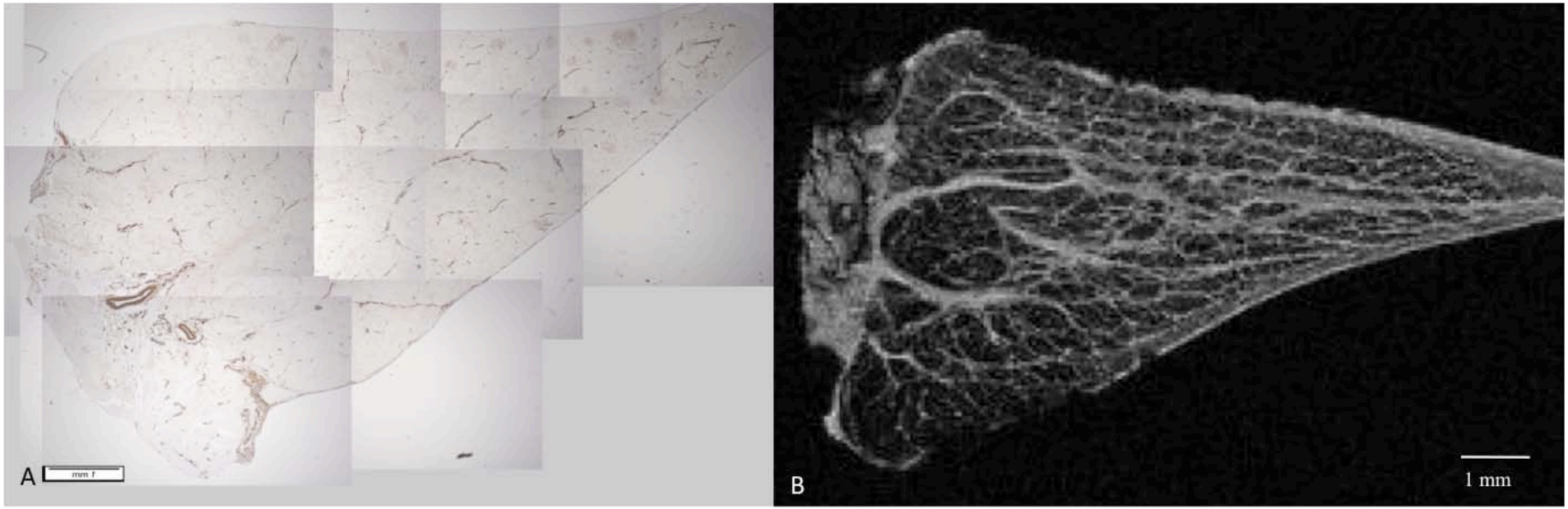

Figure 5.9 Comparison of Collagen IV staining section with MR image of the same porcine meniscal sample in blood vessel distribution. The Collagen IV immunoperoxidase labeling technique stained the collagen type IV which only presented in blood vessels in the meniscus. The stained blood vessels were sparse in the outer half, while the MR image showed obviously more structure in almost entire tissue.

To evaluate the capability of developed MRI protocol in imaging human menisci sample, two human cadaver medial knee meniscal samples were scanned using the modified 3D FLASH protocol (Figure 5.10). The scans of formalin fixed meniscus indicated the influence of formalin fixation on MR imaging. The formalin fixed meniscal tissue showed much shorter T_2 than the unfixed sample. As a result, no internal structure could be observed on MR images. The PBS immersed human meniscus showed similar high signal lines as seen in porcine menisci. In addition, these high-signal structures distributed over the entire tissue. This may further prove that the signals were from the fibrous bundles rather than blood vessels due to the fact that at least two thirds of the mature human meniscus is non-vascularised.

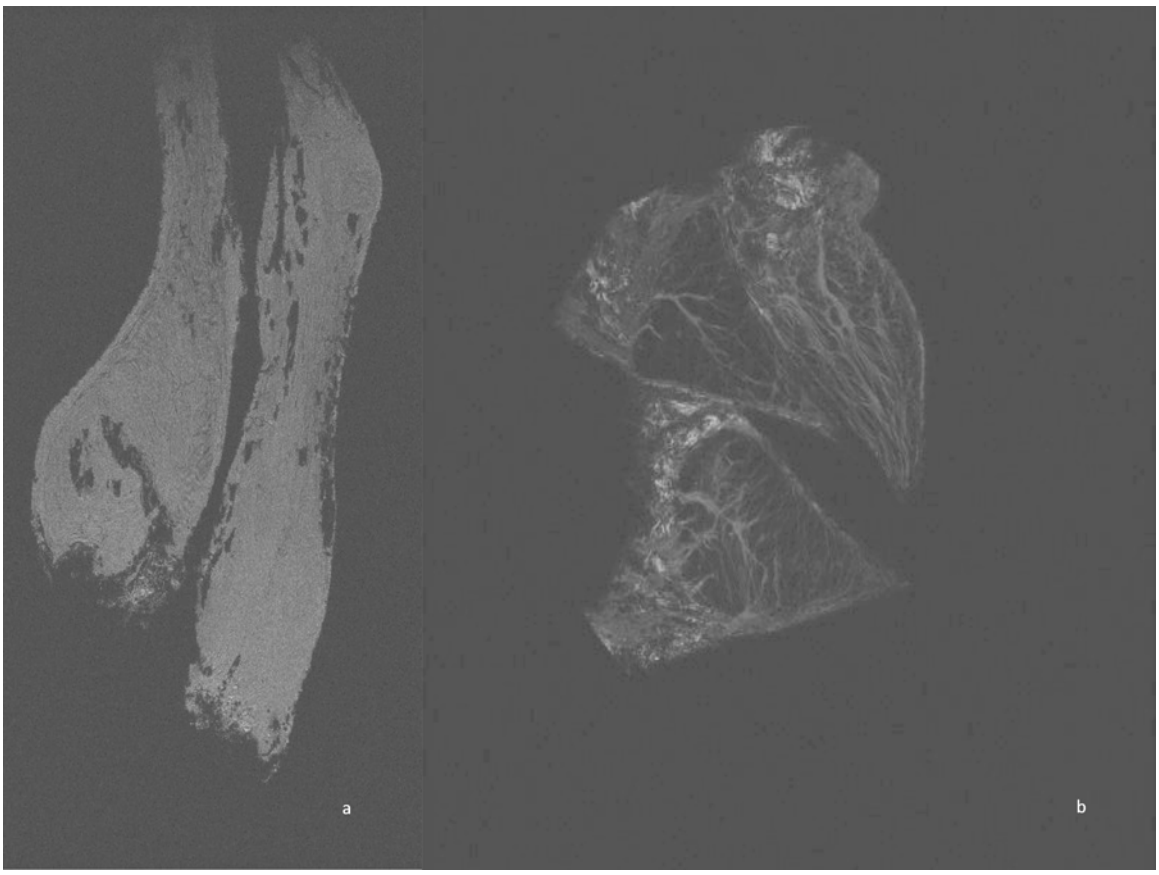

Figure 5.10 MRI of human cadaver medial menisci. a) 2D cross-sectional slice of formalin prepared meniscus, which was cut into anterior (right on the image) and posterior sections (left). b) 2D cross-sectional slice of PBS prepared meniscus, which was cut into anterior (right on the image), middle (middle), posterior sections (left).

5.3.2 MRI of menisci at 3.0T

The MRI of the porcine meniscus at 3.0 Tesla could show several major high signal lines inside the tissue (Figure 5.11). The meniscus sample could not generate enough MR signals for imaging on the 3.0 Tesla clinical scanner. To allow the use of loop surface coils, which had no spare space for extra objectives to boost signal, 0.9% (w/v) sodium chloride solution was filled in the specimen holder. The best spatial resolution had been achieved using 3D FLASH sequence. 3D FLASH images also showed better SNR and more details of intrameniscal architecture than the 2D TSE and 3D DESS scans showed similar image findings.

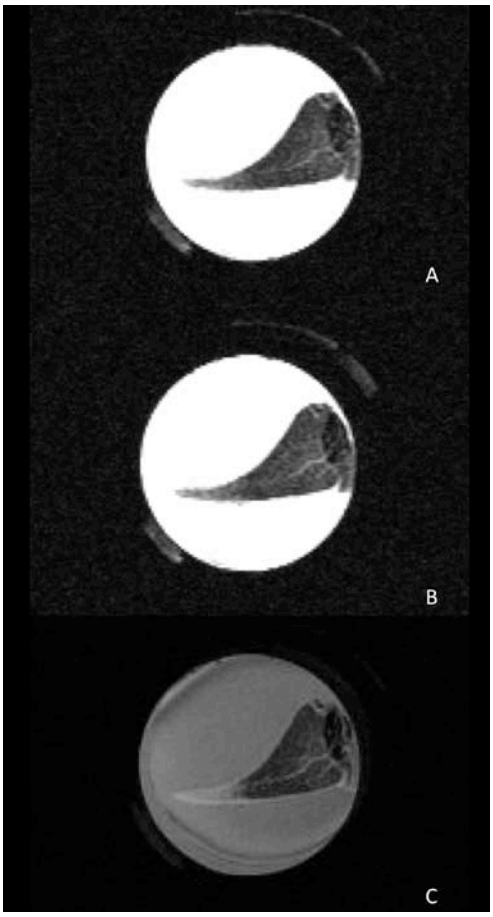

Figure 5.11 Two-dimensional MRI slices of porcine meniscus at 3.0 Tesla. The high signal surrounded the meniscal tissue was generated from sodium chloride solution. A) 2D TSE, resolution 274×274×1000 µm, acquisition time (TA) 8m 43s; B) 3D DESS, resolution 338×273×300 µm, TA 40m 49s; C) 3D FLASH, resolution 234×234×500 µm, TA 22m 18s. The FLASH 3D images showed perceivable high details and high SNR compared to the other images.

5.4 Discussion

The properties and functions of the knee meniscus have been studied for decades but have not yet been completely understood. In the field of functional meniscus biomechanics and biotribology, it is of value to be able to investigate the natural tissue matrix of the specimen after tribological experiments, in order to assess the effects of loads and motions in fundamental experiments to provide reliable reference tissue properties for tissue engineers. This may involve laboratory experiments on human or animal knee joints mimicking walking or running. These experiments can help understanding of the role of knee meniscus in the functioning of the knee joints. They also require a non-destructive method which enables visualisation of the specimen in its native form in three dimensions. The method should also be quick enough to prevent the specimen dehydrating. Light microscopy and scanning electron microscopy are commonly used to investigate meniscal structure (Bullough *et al*., 1970; Skaggs *et al*., 1994; Petersen and Tillmann, 1998; Stapleton *et al*., 2008; Pauli *et al*., 2011). However, these methods require destructive preparation of samples, and can be very time-consuming if a whole-tissue 3D investigation is required.

This study aimed to non-invasively observe the internal architecture of the natural knee meniscus on MRI. The principal target of the study was porcine meniscus due do its anatomical similarity to the human meniscus and its ready availability. The medial meniscus was chosen because the higher incidence of injury compared to the lateral meniscus (Boyd and Myers, 2003).

Several 2D short-TE Spin Echo scans of porcine menisci were run prior to protocol development and optimisation to evaluate the capability of 9.4 Tesla scanner to demonstrate meniscal tissue with ultra short T2. The resulting images could show some intrameniscal structure that could hardly be seen on a 1.5 Tesla MRI, particularly the ones with shorter TE (7.9 ms). This provided very important information on the useful TE range for imaging the meniscus.

However, due to the limits imposed on minimal slice thickness in the 2D acquisition methods, the intrameniscal signal was blurred and therefore not suitable for depicting and reconstruction of the intrameniscal architecture. FLASH 3D sequences were chosen in a series of trial scans, with the TE being set to a possible minimum value within the range of 3 to 10 ms. To reduce scan duration, a rapid 3D FISP imaging sequence was tested. The SNR and relative contrast of the 3D FISP image were both compromised. In addition, the matrix size on the phase encoding (P2) direction, or the slice direction, can only be set as half of the size on the other two directions (read and in-plane phase encoding). This has turned out to be inconvenient when attempting to set up an isotropic scan, especially for a transverse scan as described in Figure 5.2a.

The post-acquisition image analysis mainly focused on comparison of the quality of images from different protocols. Quantitative measurements such as spatial resolution, signal-to-noise ratio (SNR) and relative contrast (reCon) were performed, as well as qualitative image assessment. High spatial resolution, also known as high definition, allows demonstration of very fine details of small tissues. The higher the spatial resolution, the more details could be seen on the image providing the SNR is sufficiently high. The signal-to-noise ratio is very crucial in any imaging technology including MRI. The two meniscal MR images in Figure 5.12 showed the importance of SNR. The relative contrast of MR image is also important to differentiate two adjacent components. The intrameniscal signal is not homogeneous, the branch-like structure is always the brightest, and is surrounded by areas of lower signal intensity. Therefore, it would be helpful to acquire an image sequence with high relative contrast among internal components for characterising them. The perceived sharpness of image can be related to the spatial frequency (lp/mm) where the modulation transfer function (MTF) is 50%. In MRI, a custom made phantom can be used to calibrate the sharpness of the system. In this work, full quantitative analysis of image sharpness was not performed. Instead, the perceived sharpness of meniscal MRI was described qualitatively (as sharp or blurred).

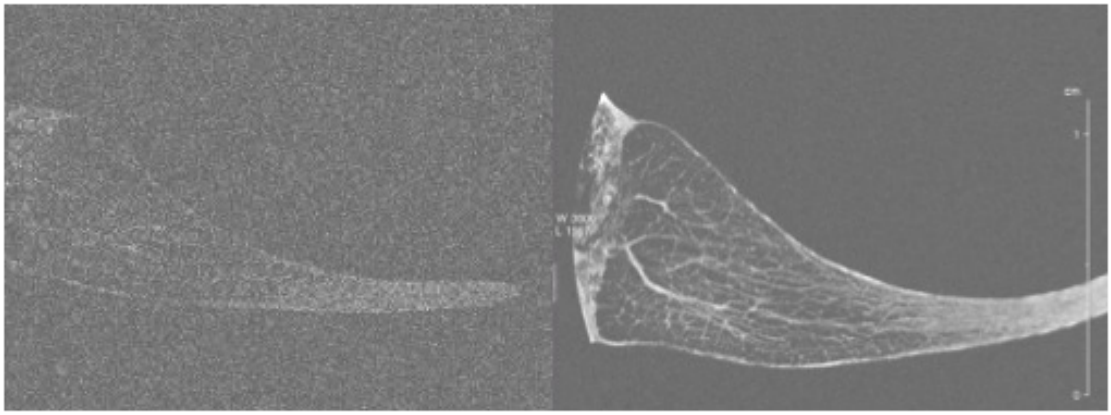

Figure 5.12 MR images of porcine menisci. The two images have the same spatial resolution while as the image on the left has much lower SNR than the one on the right. Many factors can influence image SNR, in this example, the image on the right was acquired with more average times (repeat times) than the left image, therefore the signal was stronger than the signal on the left.

A 10-hour 3D FLASH scan at 9.4 Tesla provided spatial resolution and SNR ratio that were sufficiently high to demonstrate 3D meniscal architecture and provided a virtual cross-sectional view of the internal architecture of the entire meniscus at any desired angle without any physical cut. Therefore, MRI is an eligible examine method to allowed preservation of the integrity of tissue.

At 3.0 Tesla, 3D FLASH also demonstrated it is superior to the other routine knee sequences in the examination of internal structures of the excised meniscus. A 20-minute 3D FLASH scan was able to demonstrate major architecture of the meniscus, though the signals were obviously less detailed than a longer 3D FLASH scan at 9.4 Tesla.

To minimise the influence of the tissue deformation, particularly during a long scan which lasted for over hours, two supporting pads made of polyester foam material were used. These foam pads showed no MR signal on any of the images but can firmly maintain the position of the meniscus sample in the

holder. However, dehydration of the tissue could occur during a long scan, which would result in blurring of the images. A 4.5% per hour linear height decrease of meniscal tissue has been reported to demonstrate the dehydration rate of the meniscus to air (Pham and Hull, 2007). In the future study, the application of accelerated MRI acquisition techniques may reduce the required scanning time, whilst preserving image quality.

The internal architecture of the meniscal tissue can be clearly depicted on the MR images, especially on the UHF MRI. However, it was challenging to interpret the findings due to the low specificity of conventional MRI in characterisation and differentiation of tissues. Attempt was made to increase MRI specificity in this study by using contrast agent. However, the intake rate of contrast agent of excised porcine meniscus was unknown. A porcine meniscus sample was soaked in the gadodiamide injection solution for 12 hours before 9.4T MRI scan. The image showed no significant changes of internal signals on plain MR images. Due to the limitation of availability of MRI sources for this study, advanced contrast-enhanced *in vivo* MRI techniques such as dGEMRIC (delayed gadolinium enhanced MRI of cartilage) GAG mapping (Gray *et al*., 2007; Sigurdsson *et al*., 2010) were not investigated in this *in vitro* study. Instead, histological staining techniques were chosen to serve as gold standard in the characterisation of tissues. The internal branch-like architectures of the meniscus on MR images showed high consistency with the structures visualised by the Sirius Red and the H&E staining (Figure 5.x). The porcine knees used in this study were from skeletally immature 5- to 6-month-old animals. It is known that immature menisci were more vascularised than mature menisci (Meller *et al*., 2009). Therefore, to investigate whether part of the intrameniscal signals seen on MRI were from blood vessels, collagen IV staining which was highly sensitive in revealing blood vessels in soft tissue, was done on the same meniscal sample at the same marked position. Under parallel comparison with MR and other histological images, the collagen IV staining showed much weaker agreement with others. In addition, the MRI of human cadaver menisci at 9.4T could show the similar high signal branch-like structures in almost entire area of the

tissue. The PBS prepared cadaver meniscus used in this study was from a 44-year old female, hence at least two thirds of the tissue should be avascular (Boyd and Myer, 2003). This may indicate that the majority of the architectures shown by MRI were fibrous structures of meniscal tissue.

The initial design of generation of meniscal tear model was to obtain spontaneously torn menisci after the friction and wear simulation testing. However, no lesions could be seen on the MR images of tested porcine medial menisci. The meniscal damage created in this study was done using scalpel blades. Therefore it had limitations to mimic the naturally occurred tears and the disruption of the meniscal architecture observed might differ from the natural tear signal.

5.5 Conclusion

In conclusion, MRI is a promising technique to non-destructively examine the internal structural components and damage/wear of meniscal tissue in 3D. The 3D FLASH imaging sequence should be considered as one of the preliminary MRI protocols for examination of the knee meniscus. The proof of concept measurements presented in this study illustrates the potential of non-invasive 3D MRI microscopy to bring new unique contribution to the field of functional cartilage/meniscus biomechanics and biotribology. Future study will involve development of *in vitro* contrast-enhanced imaging to help characterisation of meniscal components, characterisation of meniscal wear volume, and minimisation of the effect of dehydration and deformation using more sophisticated sample preparation and faster imaging protocols.

Chapter 6. Overall Discussion

The overall aim of this study was to utilise optimised magnetic resonance imaging at two different magnetic field strengths to quantify cartilage wear and damage as a consequence of meniscal defects, and to gain a better understanding of the internal architecture of knee meniscus on MRI. Porcine cartilage samples from the friction simulator tests and porcine medial menisci were investigated at both 9.4 Tesla and 3.0 Tesla MRI. In addition, the repeatability and accuracy of MRI-based cartilage defect quantification methods were assessed using a Pycnometer.

The requirement for MRI assessment of knee cartilage and meniscus is driven by the fact that cartilage and meniscal defects leading to knee osteoarthritis (OA) are increasingly reported in the younger population due to multiple reasons such as participation in extreme sports. Non-destructive assessment of tissues in the knee is useful to detect any tissue degeneration/damage at its early stage to determine the optimal form of treatment. MRI offers the capability for non-destructively visualising structural abnormalities and pathologies. The high sensitivity of MRI in the detection of degeneration and morphological changes of articular cartilage has been shown to be useful for diagnosing knee OA. MRI is also a powerful tool for research into cartilage such as cartilage biology, biomechanics and biotribology. The objective of this project was to develop optimised MR imaging protocols on both 9.4- and 3.0-Tesla MRI systems, to quantitatively assess the tribological response of cartilage to meniscectomy, and to delineate of the intrameniscal structure and meniscal tears in order to improve the understanding of the correlation between intrameniscal structure and meniscal functions in possible future studies.

The approach applied in this study was to develop an in vitro model of an animal medial knee compartment, which had similar anatomy to the human joint. The model requirements were that it could be tested in the pendulum

friction simulator and was small enough to be scanned on the 9.4 Tesla laboratory MRI system after testing. The porcine knee met these requirements, and it was also readily available. The medial tibiofemoral joint was chosen due to the higher incidence of injury/degradation compared to the lateral joint (Boyd and Myers, 2003).

The pendulum friction simulator testing, described in Chapter 3, applied the basic protocol described by McCann *et al*. (2009) in which a bovine half knee model was studied. The *in vitro* porcine medial knee joint model contained the whole medial tibiofemoral compartment and allowed follow-up laboratory MRI investigation of both the femoral and tibial components. The experimental study investigated three different medial knee conditions: with the intact meniscus, with partially removed meniscus, and without the meniscus. The introduction of full-scale medial porcine tibiofemoral model without capsule and ligaments to the pendulum friction simulation system was, however, not successful in friction measurement due to the geometrical constraints within the system. The complexity of porcine knee geometry and immaturity of porcine tissue should therefore be considered in the future studies when new whole knee friction simulation systems are available. However, the partial meniscectomy model, along with a series of meniscal damage/post-meniscectomy models, which were created artificially, will be of some value in future investigations of meniscal protection of cartilage when an advanced friction measurement device becomes available.

The intact meniscus (control) group showed no signs of cartilage wear after 3,600 cycles of testing. Meniscectomy, however, had a direct impact on degradation and wear of the articular cartilage surface as an average 10-mm^3 cartilage loss was found on all femoral samples and an average 4-mm^3 cartilage loss was found on tibial samples. The wear measurement results further demonstrated the important protective functions of the meniscus in the knee. Even under the non-physiological higher loading (900N peak load), the with-meniscus model rarely showed visible cartilage wear after 3,600 cycles of simulator testing. In the experimental investigation of the total

meniscectomy group, femoral and tibial wear models were successfully generated for the follow-up MRI studies which were described in Chapter 4.

With regard to the morphological quantification MRI study of cartilage, the *in vitro* MRI quantification of simulator-tested porcine cartilage samples was compared, for the first time, between an ultra high field 9.4T MRI system and a 3.0T clinical MRI system. The MRI was sensitive to cartilage loss at both magnetic field strengths. Ultra high field laboratory MRI showed superior image spatial resolution, SNR and CNR compared to high field clinical MRI. However, the laboratory MRI had very strict sample size requirements due to its narrow magnet bore (maximum 30mm diameter). The clinical MRI scanner used in this study has a magnet bore of 700 mm diameter, which allows *in vitro/ in vivo* cartilage wear quantification in whole organ MRI scans, thus it tremendously extends the application of MRI cartilage assessment after the biomechanical and biotribological experiments of either whole joints or sections. The two MRI-based measurement methods demonstrated good consistency with very low variation. Excellent precision and accuracy were shown by MRI-based methods compared to Pycnometer measurement at different magnetic field levels (all concordance correlation coefficients were greater than 0.998 with $R^2 > 0.997$).

Overall, the current study demonstrated that *in vitro* MRI cartilage wear quantification was a highly feasible and repeatable tool in biomechanics and biotribology to allow non-destructive investigations of the cartilage morphological changes following in vitro simulations.

The investigation of intrameniscal architecture by MRI was described in Chapter 5. The high definition three-dimensional internal structures of the knee meniscus were for the first time non-destructively demonstrated by MRI. A meniscal tear and consequent disruption of the structural network was clearly visible on MR images. A 3D FLASH imaging sequence was shown to

be suitable for MRI examination of the knee meniscus. A 10-hour 3D FLASH scan at 9.4 Tesla provided spatial resolution and SNR ratio that were sufficiently high to demonstrate 3D meniscal architecture and provided a virtual cross-sectional view of the internal architecture of the entire meniscus at any desired angle without any physical cut. At 3.0 Tesla, the 3D FLASH sequence also demonstrated superiority compared to other routine knee sequences in the examination of internal structures of the excised meniscus. A 20-minute 3D FLASH scan was able to demonstrate major architecture of the meniscus, though the images were obviously less detailed than a longer 3D FLASH scan at 9.4 Tesla.

Histological staining was used on the same meniscal sample at the same marked position to provide a gold standard for the characterisation of meniscal tissues. The collagen IV staining was highly sensitive in revealing blood vessels in the tissue. Sirius Red and H&E staining were used to demonstrate the fibrous architectures. Under parallel comparison, internal branch-like architectures of the meniscus on MR images showed high consistency with the structures visualised by the Sirius Red and the H&E staining, while the collagen IV staining showed limited consistency with others. This study showed evidence that the majority of the high intrameniscal MRI signal could be derived from fibrous structures. The sample set-up and imaging protocols optimised in this study show tremendous potential in the study of functional meniscus biomechanics. Future studies will involve development of *in vitro* contrast-enhanced imaging and MRI-derived parameter analyses to improve the specificity of MRI in studies of meniscal components and meniscal morphology, and to minimise the effect of dehydration and deformation using more sophisticated sample preparation and faster imaging protocols.

The work described in this thesis has several limitations in its current form. The limitations can be broadly classified into methods used in the tribological

experiments and in MRI post-acquisition analysis. Future work based on this thesis should aim to address the limitations discussed below.

As discussed above, the skeletal immaturity of the pigs used in the in vitro tribological model resulted in high tissue softness, mobility and deformability. These characteristics led to instability of the model during the tribological experiments. The pendulum friction simulator itself was initially designed for the measurement of friction in the hip joint that had simpler geometry than the knee joint. The introduction of partial meniscectomy surgery to the porcine medial compartment model, which had complex geometry and the meniscus of which had high mobility due to immaturity, was found to be beyond the capability of the simulator to correctly measure the friction and resulted in failure of testing of partial meniscectomy models. Limited understanding of porcine knee physiology and motion undermined the design of the experiment such as peak loading and flexion-extension motion settings. The small size of the porcine model benefitted the MRI investigation of the intact whole meniscal and cartilage tissue, but it also had a small contact area compared to bovine models, which resulted in the unsuitability for studies of contact stress using Fuji sensitive films as discussed in Chapter 3.

Dehydration of specimens during MRI scanning has to be considered in the current experiments. No solutions were used to immerse meniscus and cartilage samples (except for 3.0T meniscal MRI) to achieve better image contrast. The samples were therefore directly exposed to air and were unavoidably dehydrated. This issue was particularly noticeable in the meniscal MRI scan at 9.4 Tesla since normally a 10-hour acquisition time was required for one sample. Attempts were made to minimise the effect of deformation using purposefully cut supporting pads, and the sample holder was also tightly sealed to restrict airflow. The internal architecture of the meniscal tissue could be well depicted on the MR images, especially on the UHF MRI. However, it was challenging to interpret the findings due to the limited specificity of plain MRI in characterisation of tissues which have similar

signal density, and also the possible image artefacts derived from tissue shrinkage.

The two semi-automatic MR wear quantification methods were customised for use in this study. Excellent repeatability and accuracy was found using both methods. However, these image-based methods, especially the 3D surface reconstruction method, were at an early stage of development, *e.g*., they still lacked a user friendly interface and were highly dependent on image interpretation by the trained observer. Human error needs to be formally and quantitatively investigated in future work by intra- and inter-observer studies.

Conclusions

An *in vitro* porcine medial tibio-femoral joint model, which contained the whole medial tibio-femoral compartment, was developed. Friction tests of this porcine model showed similar results to previous tests using a bovine model, which has further shown the protective role of the knee meniscus in the joint. This animal model allowed follow-up in vitro non-destructive MRI investigation of knee components. A series of clinically relevant models were also developed, which would be of value in future investigations of the impact of various meniscal lesions such as damage/tear and post-surgery when an advanced simulator is available.

Cartilage MRI protocols were optimised for *in vitro* morphological quantification in this study. Two image-based semi-automatic quantification methods, combined with MR images acquired at two different magnetic field strengths, were validated by a Pycnometer. Results showed good sensitivity of defect detection and excellent repeatability and accuracy of cartilage MRI wear quantification. This study demonstrated the great potential of *in vitro* morphological MRI imaging in cartilage research in which either a small tissue section or whole joint could be non-destructively quantified after experiments.

A novel and non-destructive method to examine meniscus architecture was successfully developed at 9.4 Tesla MRI. The intrameniscal structure was for the first time revealed in 3D. Changes and damage were clearly visible on MRI with disruption of structural networks. Interpretation of image findings, which was assisted by using several gold-standard histological staining techniques, showed that the intrameniscal MR signal is most likely derived from fibres. MRI of cadaver menisci showed similar tree-branch-like architecture at 9.4 Tesla, while at 3.0 Tesla, only the major branching fibres could be identified. These image findings may provide evidence that the intrameniscal signal that is occasionally seen on clinical MRI knee examination may not necessarily be indicative of meniscus pathology.

REFERENCES

Abdelkafy, A. (2007) Modified cruciate suture technique for arthroscopic meniscal repair: a technical note. *Knee Surg. Sports Traumatol. Arthrosc*., 15: 1116-20.

Adams, M. E. and Muir, H. (1981) The glycosaminoglycans of canine menisci. *J. Biochem.*, 197: 385-389.

Adesida, A. B., Grady, L. M., et al. (2006) The matrix-forming phenotype of cultured human meniscus cells is enhanced after culture with fibroblast growth factor 2 and is further stimulated by hypoxia. *Arthritis Research & Therapy*, 8 (3): R61.

Ahmed, A. M., Burke, D. L. (1983) In-vitro measurement of static pressure distribution in synovial joints: Part I. Tibial surface of the knee. *J. Biomech. Eng.*, 105 (3): 216-225.

Ahmed, A. M., Burke, D. L., Yu, A. (1983) In-vitro measurement of static pressure distribution in synovial joints: Part II. Retropatellar surface. *J. Biomech. Eng.*, 105 (3): 226-236.

Ahn, J. H., Lee, Y. S., Chang, J. Y., Chang, M. J., Eun, S. S., Kim, S. M. (2008) Arthroscopic all inside repair of the lateral meniscus root tear. *The Knee*, doi:10.1016/j. knee.2008.07.008.

Aichroth, P. M., Cannon, W. D., Patel, D. V. (1992) *Knee Surgery: Current Practice*. Lippincott Williams and Wilkins

Alberts, B., Bray, D., Hopkin, K., Johnson, A., Lewis, J., *et al*. (2006) *Essential Cell Biology (2nd edition)*. Academic Internet Publishers Incorporated, United States.

Allen, C. R., Wong, E. K., Livesay, G. A., Sakane, M., Fu, F. H., Woo, S. L. (2000) Importance of the medial meniscus in the anterior cruciate ligament-deficient knee. *J. Orthop. Res.,*18:109-115.

Al-Turaiki, M. H. S. (1986) *The Human Knee-Functional Anatomy, Biomechanics, and Instabilities & Assessment Techniques.* Joint Centre for Research in Prosthetics and Orthotics.

An, Y. H., Martin, K. L. (2003) *Handbook of Histology Methods for Bone and Cartilage*. New Jersey; Human Press.

Andersson-Molina, H., Karlsson, H., Rockborn, P. (2002) Arthroscopic partial and total meniscectomy. *Arthroscopy: The Journal of Arthroscopic & Related Surgery*, 18 (2): 183-189.

Andriacchi, P. T., Andersson, G. B. J, Fermier, R. W., Stern, D., Galante, J. O. (1980) A study of lower-limb mechanics during stair-climbing. *J Bone Joint Surg [Am]*, 62:749-757.

Armstrong, C. G. and Mow, V. C. (1982) Variations in the intrinsic mechanical properties of human articular cartilage with age, degeneration and water content. *J Bone Joint Surg [Am]*, 64(1):88-94.

Armstrong, C. G. and Mow, V. C. (1983) The mechanical properties of articular cartilage. *Bull. Hosp. Jt. Dis. Orthop. Inst.*, 43(2):109-117.

Arnoczky, S. P. (1999). Building a meniscus. Biologic considerations. *Clin. Orthop. & Relat. Res.*, 367: s244-253.

Ashraf, S., Wibberley, H., Mapp, P. I., Hill, R., *et al*. (2011) Increased vascular penetration and nerve growth in the meniscus: a potential source of pain in osteoarthritis. *Ann Rheum Dis.*, 70(3): 523-529.

Assimakopoulos, A. P., Katonis, P. G., Agapitos, M. V., *et al*. (1992) The innervation of the human meniscus. *Clin Orthop Relat Res*, 275: 232–236.

Ateshian, G. A., Soltz, M. A., Mauck, R. L., Basalo, I. M., Hung, C. T., Lai, W. M. (2003) The role of osmotic pressure and tension-compression non-linearity in the frictional response of articular cartilage. *Transport in Porous Media*, 50(1-2): 5-33.

Badylak, S. F. (2002) The extracellular matrix as a scaffold for tissue reconstruction. *Seminars in Cell & Developmental Biology*, 13: 377-383.

Badylak, S. F. (2004) Xenogeneic extracellular matrix as a scaffold for tissue reconstruction. *Transplant Immunology*, 12: 367-377.

Bahr, R., Mahlum, S. (editors); Bolic, T. (Medical illustrator) (2004) *Clinical Guide to Sports Injuries*. Human Kinetics Publishers.

Baliunas, A. J., Hurwitz, D. E., Ryals, A. B., Karrar, A., Case, J. P. and Block, J. A., *et al*. (2002) Increased knee joint loads during walking are present in subjects with knee osteoarthritis. *Osteoarthritis & Cartilage*, 10: 573–579.

Baratz M. E., Fu F.H., Mengato R. (1986) Meniscal tears: the effect of meniscectomy and of repair on intraarticular contact areas and stress in the human knee. *Am. J. Sports Med.*, 14: 270-274.

Bashir, A., Gray, M. L., Burstein, D. (1996) Gd-DTPA^{2-} as a measure of cartilage degradation. *MRM*, 36: 665-673.

Bauer, J. S., Krause, S. J., Ross, C. J., Krug, R., *et al*. (2006) Volumetric cartilage measurements of porcine knee at 1.5-T and 3.0-T MR imaging: evaluation of precision and accuracy. *Radiology*, 241(2): 399-406.

Becker, R., Brettschneider, O, Grobel, Karl-Heinz, *et al*. (2006) Distraction forces on repaired bucket-handle lesions in the medial meniscus. *Am. J. Sports Med.*, 34(12): 1941-1947.

Bell, C. J., Ingham, E., Fisher, J. (2006) Influence of hyaluronic acid on the time-dependent friction response of articular cartilage under different conditions. *Proc Inst Mech Eng [H]*, 220:23–31.

Bencsik, M., Bowtell, R., Bowley, R. (2007) Electric fields induced in the human body by time-varying magnetic field gradients in MRI: numerical calculations and correlation analysis. *Phys. Med. Biol*., 52: 2337–2353.

Bendele, A. M., Hulman, J. F. (1988) Spontaneous cartilage degeneration in guinea pigs. *Arthritis and Rheumatism*, 31 (4): 561-565.

Bloch, F., Hansen, W. W., Packard, M. E. (1946) Nuclear induction. *Phys. Rev*., 69: 127.

Bolbos, R. I., Link, T. M., Benjamin Ma, C., *et al*. (2009) T1ρ relaxation time of the meniscus and its relationship with T1ρ of adjacent cartilage in knees with acute ACL injuries at 3T. *Osteoarthritis and Cartilage*, 17: 12-18.

Boxheimer, L., Lutz, A. M., Treiber, K., *et al*. (2004) MR imaging of the knee: position related changes of the menisci in asymptomatic volunteers. *Invest Radiol*, 39(5): 254–63.

Boyd, K. T., Myers, P. T. (2003) Meniscus preservation: rationale, techniques and results. *The Knee*, 10: 1-11.

Braz, P. R. P. and Silva, W. G. (2010) Meniscus morphometric study in humans. *J. Morphol. Sci*., 27(2): 62-66.

Breusegham, I. V., Bosmans, H. T. C., Elst, L. V., Maes, F., Pans, S. D., *et al*. (2004) T2 mapping of human femerotibial cartilage with turbo-mixed MR Imaging at 1.5 T: feasibility. *Radiology*, 233 (2): 609-614.

Broom, N. D. (1986) Structural consequences of traumatising articular cartilage. *Ann. Rheum. Dis*., 45: 225-234.

Brown, J. (2004) Soft tissue injuries of the knee. *Orthopaedic surgery*, p40-44.

Brukner, P. and Khan, K. (2001) *Clinical sports medicine*, *2nd edition*. Roseville, NSW; London: McGraw-Hill.

Bullough, P. G., Munuera, L., Murphy, J., *et al*. (1970) The strength of the menisci of the knee as it related to their fine structure. *J Bone Joint Surg*. 52:564-567.

Buma, P., Ramrattan, N. N., van Tienen, T. G., Veth, R. P. H. (2004) Tissue engineering of the meniscus. *Biomaterials*, 25:1523-1532.

Buma, P., van Tienen, T. & Veth, R. P. (2007). The collagen meniscus implant. *Expert Review of Medical Devices*, 4: 507-516 (abstract).

Burrage, P. S., Brinckerhoff, C. E. (2007) Molecular targets in osteoarthritis: metalloproteinases and their inhibitors. *Curr Drug Targets*, 8 (2): 293-303.

Carlson, C. S., Kraus, V. B., Vail, T. P., *et al*. (1999) Articular cartilage damage following complete medial meniscectomy in dogs is predicted by synovial fluid biomarker levels. *Trans. ORS*, 24: 194 (Abstract).

Campbell, S. E., Sanders, T. G., Morrison, W. B. (2001) MR imaging of meniscal cysts: incidence, location, and clinical significance. *Am J Roentgenol*, 177(2): 409–413.

Cawston, T. E. and Wilson, A. J. (2006) Understanding the role of tissue degrading enzymes and their inhibitors in development and disease. *Best practice & Research clinical Rheumatology*, 20(5): 983-1002.

Chang, H. C., Nyland, J., *et al*. (2005) A comparison of the meniscal viper repair system, the vertical mattress FastT-Fix device, and vertical mattress ethibond sutures. *The American Journal of Sports Medicine*, 33(12): 1846-1852.

Changoor, A., Nelea, M., Methot, S., Tran-Khanh, N., Chevrier, A., Restrepo, A. (2011) Structural characteristics of the collagen network in human normal, degraded and repair articular cartilages observed in polarized light and scanning electron microscopies. *Osteoarthritis and Cartilage*, 19: 1458-1468.

Charnley, J., 1960. The lubrication of animal joints in relation to surgical reconstruction by arthroplasty. *Ann. Rheum. Dis*., 19: 10-19.

Chen, F. H., Rousche, K. T., Tuan, R. S. (2006) Technology Insight: adult stem cells in cartilage regeneration and tissue engineering. *Nature Clinical Practice Rheumatology*, 2: 373-382.

Chen, Y., Crawford, R. W., Oloyede, A. (2007) Unsaturated phosphatidylcholines lining on the surface of cartilage and its possible physiological roles. *J Orthop Surg*., 2: 14.

Christoforakis, J., Pradhan, R., Sanchez-Ballester, J., Hunt, N., Strachan, R. K. (2005) Is there an association between articular cartilage changes and degenerative meniscus tears? *Arthroscopy: The journal of Arthroscopy and Related Surgery*, 21 (11): 1366-1369 (abstract).

Ciliz, D., Ciliz, A., Elverici, E., *et al*. (2008) Evaluation of postoperative menisci with MR arthrography and routine conventional MRI. *Clinical Imaging*, 32: 212-219.

Collins, J. J. (1995) The redundant nature of locomotor optimization laws. *J Biomech*, 28: 251-67.

Colombo, C., Butler, M., O'Byrne, E., *et al*. (1983) A new model of osteoarthritis in rabbits, I, development of knee joint pathology following lateral meniscectomy and section of the fibular collateral and sesamoid ligaments. *Arthritis and Rheumatism*, 26 (7): 875-886.

Cook, J. L., Tomlinson, J. L., Kreeger, J. M., Cook, C. R. (1999) Induction of meniscal regeneration in dogs using a novel biomaterial. *Am. J. Sports Med.*, 27: 658-665.

Cook, J. L., Tomlinson, J. L., Arnoczky, S. P., Fox, D. B., Cook, C. R., Kreeger, J. M. (2001) Kinetic study of the replacement of porcine small intestinal submucosa grafts and the regeneration of meniscal-like tissue in large avascular meniscal defects in dogs. *Tissue Engineering*, 7 (3): 321-336.

Cook, J. L., Fox, D. B., Malaviya, P., Tomlinson, J. L., Kuroki, K., Cook, C. R., Kladakis, S. (2006) Long-term outcome for large meniscal defects treated with small Intestinal submucosa in a dog model. *Am. J. Sports Med*., 34: 32-42.

Costa, C. R., Morrison, W. B., Carrino, J. A. (2004) Medial meniscus extrusion on knee MRI: is extent associated with severity of degeneration or type of tear? *Am J Roentgenol*, 183(1): 17–23.

Cox, J. S., Nye, C. E., Schaefer, W. W., Woodstein, I. J. (1975) The degenerative effects of partial and total resection of the medial meniscus in dogs knees. *Clinical Orthopaedics & Related Research*, 109: 178-183.

Crema, M. D., Guermazi, A., Sayre, E. C., Roemer, F. W., *et al*. (2011) The association of magnetic resonance imaging (MRI)-detected structural pathology of the knee with crepitus in a population-based cohort with knee pain: the MoDEKO study. *Osteoarthritis and Cartilage*, 19: 1429-1432.

Crues, J. V. III, Mink, J., Levy, T. L., *et al*. (1987) Meniscal tears of the knee: accuracy of MR imaging. *Radiology*, 164: 445-448.

Damion, R. A., Pawaskar, S. S., Ries, M. E., Ingham, E., *et al*. (2012) Spin-lattice relaxation rates and water content of freeze-dried articular cartilage. *Osteoarthritis and Cartilage*, 20(2): 184-190.

DeHaven, K., Arnoczky, S. P. (1994) Meniscal repairs: part 1: basic science, indications for repair, and open repair. *J. Bone Joint Surg. Am*, 76: 140-152.

De Maeseneer, M., Shahabpour, M., Vanderdood, K., *et al*. (2002) Medial meniscocapsular separation: MR imaging criteria and diagnostic pitfalls. *Eur J Radiol*, 41(3): 242–252.

De Smet, A. A., Norris, M. A., Yandow, D. R., *et al*. (1993) MR diagnosis of meniscal tears of the knee: impor- tance of high signal in the meniscus that ex- tends to the surface. *Am J Roentgenol*,161(1): 101–107.

Di Lullo, G. A., Sweeney, S. M., Korkko, J., *et al*. (2002) Mapping the Ligand-binding Sites and Disease-associated Mutations on the Most Abundant Protein in the Human, Type I Collagen. *J of Biolog. Chem*., 277 (6): 4223-4231.

Ding, C. H., Martel-Pelletier, J., Pelletier, J. P., *et al*. (2007) Meniscal tear as an osteoarthritis risk factor in a largely non-osteoarthritic cohort: a cross-sectional study. *J. Rheumotology*, 34 (4): 776-784.

Disler, D. G., McGauley, T. R., Kelman, C. G., *et al*. (1996) Fat-suppressed three-dimensional spoiled gradient-echo MR imaging of hyaline cartilage defects in the knee: comparison with standard MR imaging and arthroscopy. *AJR Am J Roentgenol.*, 167(1): 127-132.

DiSilvestro, M. R., Suh, J. K. (2002) Biphasic poroviscoelastic characteristics of proteoglycan-depleted articular cartilage: simulation of degeneration. *Ann. Biomed. Eng.*, 30: 792-800.

Dowson, D. and Wright, V. (1981) *Introduction to the Biomechanics of Joints and Joint Replacement (1st edition)*. Wiley-Blackwell.

Dowson, D., Jin, Z. M. (1986) Micro-elastohydrodynamic lubrication of synovial joints. *Eng. Med*., 15: 63-65.

Dowson, D. (1990). Biotribology of natural and replacement synovial joints. In *Biomechanics of diarthroidal joints*, edited by Mow, V. C., Ratcliffe, A., Woo, S. L. Y. New York, Springer-Verlag. II: 305-345.

Dunn, T. C., Lu, Y., Jin, H., Ries, M. D., Majumdar, S. (2004) T2 relaxation time of cartilage at MR Imaging: comparison with severity of knee osteoarthritis. *Radiology*, 232 (2): 592-598.

Dürselen, L., Hebisch, A., Claes, L. E., Bauer, G. (2003) Gapping phenomenon of longitudinal meniscal tears. *Clinical Biomechanics*, 18: 505-510.

Eckstein, F., Cicuttini, F., Raynauld, J. P., F. R. C. P. C. (2006) Magnetic resonance imaging (MRI) of articular cartilage in knee osteoarthritis (OA): morphological assessment. *Osteoarthritis & Cartilage*, 14: A46-A75.

Eckstein, F. (2011) Quantitative Assessment of cartilage using MRI and its relation to OA. *Seminars in Arthritis and Rheumatism*, 41(1): 91-92.

Eisenberg, S. R., Grodzinsky, A. J. (1987) The kinetics of chemically induced nonequilibrium swelling of articular cartilage and corneal stroma. *ASME J Biomech Eng*, 109:79-89.

Englund, M., Roos, E. M., Lohmander, L. S. (2001) Patient-relevant outcomes fourteen years after meniscectomy: influence of type of meniscal tear and size of resection. *Rheumatology*, 40: 631-639.

Englund, M., Roos, E. M., Lohmander, L. S. (2003) Impact of type of meniscal tear on radiographic and symptomatic knee osteoarthritis: a sixteen-year followup of meniscectomy with matched controls. *Arthritis Rheum*, 48:2178-87.

Erbagci, H., Gumusburun, E., Bayram, M., *et al*. (2004) The normal menisci: in vivo MRI measurements. *Surg Radiol Anat*, 26: 28-32.

Ericson, M.O., Nisell, R. (1986) Tibiofemoral joint forces during ergometer

cycling. *Am J Sports Med*, 14:285-90.

Ericson, M.O., Nisell, R. (1987) Patellofemoral joint forces during ergometric cycling. *Phys. Ther*.; 67:1365-1369.

Eyre, D. R., Muir, H. (1975) The distribution of different molecular species collagen in fibrous, elastic and hyaline cartilage of the pig. *J. Biochem*., 151: 595-602.

Eyre, D. R. (1980) Collagen: molecular diversity in the body's protein scaffold. *Science,* 207: 1315-1322.

Eyre, D. R., Wu, J. J. (1983) Collagen of fibrocartilage: a distinctive molecular phenotype in bovine meniscus. *FEBS lett*; 158:265-270.

Fankhauser (2008) Features of major joints. Access via the Internet:

http://biology.clc.uc.edu/Fankhauser/Labs/Anatomy_&_Physiology/A&P201/Articulations/Joints.htm

Favenesi, J. A., Shaffer, J. C., Mow, V. C. (1983) Biphasic mechanical properties of knee meniscus. *Orthop. Trans*., 8:174.

Fischer, S. P., Fox, J. M., Delpizzo, W., *et al*. (1991) Accuracy of diagnoses from magnetic-resonance-imaging of the knee- a multicenter analysis of 1014 patients. *Journal of Bone and Joint Surgery Am*. 73A(1): 2-10.

Fithian, D. C., Schmidt, M. B., Ratcliffe, A., Mow, V. C. (1989) Human meniscus tensile properties: Regional variation and biochemical correlation. *Orthop. Trans*., 14:205.

Fithian, D. C., Kelly, M. A., Mow, V. C. (1990) Material properties and structure-function relationships in the menisci. *Clin. Orthop. & Relat. Res*., 252: 19-31.

Forsey, R. W., Fisher, J., Thompson, J., Stone, M. H., Bell, C., Ingham, E. (2006) The effect of hyaluronic acid and phospholipid based lubricants on friction within a human cartilage damage model. *Biomaterials*, 27:4581–90.

Fosang, A.J., Hardingham, T. E. Matrix proteoglycans. In: Comper, W. D., ed. (1996) *Extracellular matrix (1st edition)*. CRC Press.

Forster, H., Fisher, J. (1996) The influence of loading time and lubricant on the friction of articular cartilage. *Proc Inst Mech Eng*., [H] 210(2): 109-119.

Fragonas, E., Mlynarik, V., Jellus, V., Micali, F., *et al*. (1998) Correlation between biochemical composition and magnetic resonance appearance of articular cartilage. *Osteoarthritis and Cartilage*, 6(1): 24-32.

Freeman, M. E., Furey, M. J., Love, B. J. & Hamptom, J. M. (2000) Friction, wear and lubrication of hydrogels as synthetic articular cartilage. *Wear*, 241: 129-135.

Freeman, M. A. R. and Pinskerova, V. (2005) The movement of the normal tibio-femoral joint. *Journal of Biomechanics*, 38: 197-208.

Fukubayashi, T., Kurosawa, H. (1980) The contact area and pressure distribution pattern of the knee: a study of normal and osteoarthrotic knee joints. *Acta Orthopaedica*, 51: 871-879.

Fukuda, Y., Takai, S., Yoshino, N. *et al*. (2000) Impact load transmission of the knee joint-influence of leg alignment and the role of meniscus and articular cartilage. *Clinical Biomechanics*, 15: 516-521.

Gatehouse, P. D., He, T., Puri, B. K., Thomas, R. D., Resnick, D., Bydder, G, M. (2004) Contrast-enhanced MRI of the menisci of the knee using ultrashort echo time (UTE) pulse sequences: imaging of the red and white zones. *The British Journal of Radiology*, 77: 641–647.

Ghosh, P., Taylor, T.K., Pettit, G.D., *et al*. (1983) Effect of postoperative immobilization on the regrowth of the knee joint semilunar cartilage: an experimental study. *J Orthop Res*. 1:153-164.

Goertzen, D. J., Rudney, D. R., Cinats, J. G. (1997) Methodology and apparatus to determine material properties of the knee joint meniscus. *Medical Engineering & Physics*, 19(5): 412-419.

Gold, G. E., Suh, B., Sawyer-Glover, A., Beaulieu, C. (2004). Musculoskeletal MRI at 3.0 T: Initial clinical experience. *Am. J. Roentgenol*., 183:1479–1486.

Gray, M., Burstein, D., Kim, Y. J., Maroudas, A. (2007) Magnetic Resonance Imaging of Cartilage Glycosaminoglycan: Basic Principles, Imaging Technique, and Clinical Applications. *J. Orthop. Res*., 281-291.

Griffin, N., Joubert, I., Lomas, D. J., Bearcroft, P. W. P., Dixon, A. K. (2008) High resolution imaging of the knee on 3-Tesla MRI: a pictorial review. *Clin. Ana*.,21: 374-82.

Guivel-Scharen, V., Sinnwell, T., Wolff, S. D., Balaban, R. S. (1998) Detection of proton chemical exchange between metabolites and water in biological tissues. *J. Mag. Res*., 133: 36-45.

Haklar, U., Kocaoglu, B., Nalbantoglu, U., Tuzuner, T., Guven, O. (2008) Arthroscopic repair of radial lateral menicus tear by double horizontal sutures with inside–outside technique. *The Knee*, 15: 355-359.

Hallén, L. G. and Lindahl, O., (1966). The “screw-home” movement in the knee joint. *Acta Orthopedica Scandinavia*, 37: 97–106.

Hardingham, T. E. (1981) Proteoglycans: their structure, interactions and molecular organization in cartilage. *Biomech. Soc. Trans*., 9: 489-497.

Hardingham, T. E. and Fosang, A. J. (1992) Proteoglycans: many forms and many functions. *FASEB J*., 6: 861-870.

Hardingham, T. E. and Bayliss, M. (1990) Proteoglycans of articular cartilage: changes in aging and in joint diseases, *Semi. Arth. Rheum., Suppl*., 1: 12-33.

Harper, K. W., Helms, C. A., *et al*. (2005) Radial meniscal tears: significance, incidence, and MR appearance. *AJR*, 185: 1429-1434.

Hellio Le Graverand, M. P., Reno, C., *et al*. (1999) Gene expression in menisci from the knees of skeletally immature and mature female rabbits. *J. Orthop. Res*., 17: 738-744.

Hopker, W. W., Angres, G., Klingel, K., Komitowski, D., Schuchardt, E. (1986) Changes in the elastin compartment of the human meniscus. *Virch Arch (Path Anat)*, 408: 575-592

Horton, H. R. *et al*. (2006) *Principles of Biochemistry (4th Edition)*. Prentice Hall.

Hsieh, H. H. and Walker, P. S. (1976) Stabilizing mechanisms of the loaded and unloaded knee joint. *J. Bone Joint Surg. Am*., 58: 87-93.

Hunter, D. J., Zhang, Y. Q., Niu, J. B., *et al*. (2006) The association of meniscal pathologic changes with cartilage loss in symptomatic knee osteoarthritis. *Arthritis Rheum*, 54:795-801.

Hunter, D. J., Bowes, M. A., Eaton, C. B., Holmes, A. P., Mann, H., *et al*. (2010) Can cartilage loss be detected in knee osteoarthritis (OA) patients with 3-6 months' observation using advanced image analysis of 3 T MRI? *Osteoarthritis and Cartilage*, 18: 677-683.

Hwang, S. H., Jung, K. A., Lee, W. J., Yang, K. H., *et al*. (2012) Morphological changes of the lateral meniscus in end-stage lateral compartment osteoarthritis of the knee. *Osteoarthritis and Cartilage*, 20 (2): 110-116.

Ihn, J. C., Kim, S. J., Park, I. H. (1993) In vitro study of contact area and pressure distribution in the human knee after partial and total meniscectomy. *International Orthopaedics*, 17: 214-218.

Imer, R., Akiyama, T., De Rooij, N. F., *et al*. (2009) The measurement of biomechanical properties of porcine articular cartilage using atomic force microscopy. *Archives of Histology and Cytology*, 72: 251-259.

Israelachvili, J. N. (1985). *Intermolecular and Suflace Forces with Applications to Colloidal and Biological Systems*. New York; Academic Press, Page: 201-207.

Jay, G. D. (1992) Characterization of a bovine synovial fluid lubricating factor. I. Chemical, Surface activity and lubricating properties. *Connective Tissue Res*., 28:171 -88.

Jay, G. D., Haberstroh, K., Cha, C. J. (1998) Comparison of the boundary-lubricating ability of bovine synovial fluid, lubricin, and Healon. *J. Biomed. Mater. Res*., 40:414–8.

Jerosch, J., Hoffstetter, I., Reer, R., Assheuer, J. (1994) Strain-related long-term changes in the menisci in asymptomatic atheletes. *Knee Surg, Sports Traumatol, Arthroscopy*, 2: 8-13.

Johal, P., Williams, A., Wragg, P., Hunt, D., Gedroyc, W. (2005) Tibio-femoral movement in the living knee. A study of weight bearing and non-weight bearing knee kinematics using 'interventional' MRI. *Journal of Biomechanics*, 38: 269-276.

Johnson, R., Kettelkamp, D. B., Clark, W., Leaverton, P. (1974) Factors affecting later results after meniscectomy. *J. Bone Joint Surg. Am*, 56: 719-729.

Kamimura, T., Ishii, Y., Andoh, K. and Korenaga, T. (1999) MRI of the medial meniscus in patients over 40 years of age with osteoarthritic knees. *The Knee*, 6: 103-108.

Katta, J., Pawaskar, S. S., Jin, Z. M., Ingham, E., Fisher, J. (2007) Effect of load variation on the friction properties of articular cartilage. *Proc Inst Mech Eng [J]: Engineering Tribology*, 221, 175-181.

Katta, J., Jin, Z., Ingham, E., Fisher, J. (2008a) Biotribology of articular cartilage: a review of the recent advances. *Med. Eng. Phy*., doi: 10.1016/j.medengphy. 2008.09.004.

Katta, J., Stapleton, T., Ingham, E., Jin, Z., Fisher, J. (2008b) The effect of glycosaminoglycan depletion on the friction and deformation of articular cartilage. *Proc Inst Mech Eng, (H) -J Eng Med*, 222:1–11.

Keenan, K. E., Besier, T. F., Pauly, J. M., Han, E., Rosenberg, J., *et al*. (2011) Prediction of glycosaminoglycan content in human cartilage by age, T1r and T2 MRI. *Osteoarthritis and Cartilage*, 19: 171-179.

Kohn, D. (1993) Autograft meniscus replacement: experimental and clinical results. *Knee Surg., Sports Traumatol., Arthroscopy*,1: 123-125.

Kohn, D., Rudert, M., Wirth, C. J., Plitz, W., Reiss, G., Maschek, H. (1997) Medial meniscus replacement by a fat pad autograft. An experimental study in sheep. *International Orthopaedics (SICOT)*, 21: 232–238.

Koo, S., Gold, G. E., Andriacchi, T. P. (2005) Considerations in measuring cartilage thickness using MRI: factors influencing reproducibility and accuracy. *Osteoarthritis and Cartilage*, 13: 782-789.

Kornick, J., Trefeiner, E., McCarthy, S., Lange, R., Lynch, K., Jokl, P. (1990) Meniscal abnormalities in the asymptomatic population at MR imaging. *Radiology*, 177:463-465.

Krause, W. R., Pope, M. H., Johnson, R. J., Wilder, D, G. (1976) Mechanical changes in the knee after meniscectomy. *J. Bone Joint Surg. Am*, 58: 599-604.

Kuster, M. S., Wood, G. A., Stachowiak, G. W., Gachter, A. (1997) Joint load considerations in total knee replacement. *J. Bone Joint Surg. Br*, 79 (1): 599-604.

Lai, W. M. and Mow, V. C. (1980) Drag-induced compression of articular cartilage during a permeation experiment. *Biorheology*, 17 (1-2): 111-23.

Lai, W. M., Mow, V. C. & Roth, V. (1981). Effects of non-linear strain-dependent permeability and rate of compression on the stress behaviour of articular cartilage. *J Biomech. Eng*., 103: 61-66.

Lamoreaux, L. W. (1971) Kinematic measurements in the study of human walking. *Bul. of Pros. Res*., (cited from Al-Turaiki, 1986).

Lauterbur, P. C. (1973). "Image Formation by Induced Local Interactions: Examples of Employing Nuclear Magnetic Resonance". *Nature*, 242 (5394): 190–191

Lawrence, M., *et al*. (2006). *Thieme atlas of anatomy: general anatomy and musculoskeletal system*. Stuttgart, Thieme.

Lechner, K., Hull, M. L., Howell, S. M. (2000) Is the circumferential tensile modulus within a human medial meniscus affected by the test sample location and cross-sectional area? *J. Orthop. Res*., 18: 945-951.

Lee, J. H. E., Singh, T. T., Bolton, G. (2002) Axial fat-saturated FSE imaging of knee: appearance of meniscal tears. *Skeletal Radiol*., 31:384–395.

Lee, S. J., Aadalen, K., Malavlya, P., *et al*. (2006) Tibiofemoral contact mechanics after serial medial meniscectomies in the human cadaveric knee. *The American Journal of Sports Medicine*, 34(8): 1334-1344.

Levy, I. M., Torzilli, P. A., Warren, R. F. (1982) The effect of medial meniscectomy on anterior-posterior motion of the knee. *J. Bone Joint Surg*. Am, 64:883-888.

Levy, I. M., Torzilli, P. A., Gould, J. D., Warren, R. F. (1989) The effect of lateral meniscectomy on motion of the knee. *J. Bone Joint Surg. Am*., 71:401-406.

Lewis, P. R., McCutchen, C. W. (1959) Experimental evidence for weeping lubrication in mammalian joints. *Nature*, 184: 1284-1285.

Lin, P. C., Irrechukwu, O., Roque, R., Hancock, B., Fishbein, K. W. and Spencer, R. G. (2011) Multivariate analysis of cartilage degradation using the support vector machine algorithm. *Magnetic Resonance in Medicine*, DOI: 10.1002/mrm.23189.

Ling, W., Regatte, R. R., Navon, G., Jerschow, A. (2008a) Assessment of glycosaminoglycan concentration in vivo by chemical exchange-dependent saturation transfer (gagCEST). *PNAS*, 105 (7): 2266-2270.

Ling, W., Regatte, R. R., Navon, G., Jerschow, A. (2008b) gagCEST & NOE: Assessment of Glycosaminoglycan Concentration in Vivo. *Proc. Intl. Soc. Mag. Reson. Med.*, 16: 323.

Lipshitz, H., Etheredge, 3rd. R., Glimcher, M. J. (1975) In vitro wear of articular cartilage. *J. Bone Joint Surg. Am*., 57:527–34.

Lotysch, M., Mink, J., Crues, J. V., Schwartz, S. A. (1986) Magnetic resonance imaging in the detection of meniscal injuries. *Magnetic Resonance Imaging*, 4(2): 185.

MacConail, M. A. (1932) The function of intra-articular fibrocartilages, with special references to the knee and inferior radio-ulnar joints. *J. Anat*., 66: 210-227.

Mankin, H. J., Dorfman, H., Lippiello, L., *et al*. (1971) Biomechanical and metabolic abnormalities in articular cartilage from osteo-arthritic human hips. *J. Bone Joint Surg. Am*., 53:523-537.

Mankin, H. J. and Thrasher, A. Z. (1975) Water content and binding in normal and osteoarthritic human cartilage. *J Bone Joint Surg Am*, 57:76-80.

Mankin, H. J. (1982) The response of articular cartilage to mechanical injury. *J Bone Joint Surg Am*., 64: 460-466.

Maquet, P. G., Van de Berg, A. J., Simonet, J. C. (1975) Femorotibial weight-bearing areas. Experimental determination. *J Bone Joint Surg Am*, 57:766-771.

Martin, U., Kiessig, V., Blusch, J. H., *et al*. (1998) Expression of pig endogenous retrovirus by primary porcine endothelial cells and infection of human cells. *Lancet*, 352: 692-694.

Martinek, V., Ueblacker, P., Bräun, K., Nitschke, S., Mannhardt, R., Specht, K., Gansbacher, B., Imhoff, A. B. (2006). Second generation of meniscus transplantation: in-vivo study with tissue engineered meniscus replacement. *Archives of Orthopaedic and Trauma Surgery*, 126: 228-234.

Mastrokalos, D. S., Papagelopoulos, P. J., Mavrogenis, A. F., Hantes, M. E., Karachalios, T. S., Paessler, H. H. (2005) Changes of meniscal interhorn distances: an in vivo magnetic resonance imaging study. *The Knee*,12(6): 441–6.

Matthews, L. S., Sonstegard, D. A., Henke, J. A. (1977) Load bearing characteristics of the patello-femoral joint. *Acta. Orthop. Scand.*, 48:511-516.

McCann, L., Udofia, I., Graindorge, S., Ingham, E., Jin, Z., Fisher, J. (2008) Tribological testing of articular cartilage of the medial compartment of the knee using a friction simulator. *Tribology International*, 41: 1126– 1133.

McCann, L. (2009) Influence of the meniscus on friction and degradation of cartilage in the natural knee joint. *Osteoarthritis and Cartilage*, doi:10.1016/j.joca.2009.02.012.

McCutchen, C. W. (1959) Sponge-hydrostatic and weeping bearings. *Nature*, 184: 1284-1285.

McDermott, I. D., Amis, A, A, (2006) The consequences of meniscectomy. *J Bone Joint Surg Br*, 88 (12): 1549-1556.

McDermott, I. D., *et al*. (2008) Biomechanics of the menisci of the knee. *Current Orthopaedics*, 22, 193-201.

McDevitt, C. A. and Webber, R. J. (1990) The ultrastructure and biochemistry of meniscal cartilage. *Clinical Orthopaedics & Related Research*, 252: 8-18.

McGibbon, C. A. and Trahan, C. A. (2003) Measurement accuracy of focal cartilage defects from MRI and correlation of MRI graded lesions with histology: a preliminary study. *Osteoarthritis and Cartilage*, 11: 483-493.

McGinty, J. B., Guess, L. F., Marvin, M. D., Falls, N. L. (1977) Partial or total meniscectomy. *J Bone Joint Surg Am*, 59: 763-766.

McGinty, J.B., Burkhart, S.S., Jackson, R.W., Johnson, D.H., Richmond, J.C. (2002) *Operative Arthroscopy (3rd edition)*: page 222.

Meller, R., Schiborra, F., Brandes, G., *et al*. (2009) Postnatal maturation of tendon, cruciate ligament, meniscus and articular cartilage: A histological study in sheep. *Annals of Anatomy*, 191: 575-585.

Menashe, L., Hirko, K., Losina, E., *et al*. (2012) The diagnostic performance of MRI in osteoarthritis: a systematic review and meta-analysis. *Osteoarthritis and Cartilage*, 20: 13-21.

Messner, K. (1994) Review: the concept of a permanent synthetic meniscus prosthesis: a critical discussion after 5 years of experimental investigations using Dacron and Teflon implants. *Biomaterials*, 15 (4): 243-250.

Messner, K., Gao, J. (1998) The menisci of the knee joint. Anatomical and functional characteristics, and a rationale for clinical treatment. *J. Anatomy*, 193: 161-178.

Moffet, H., Richards, C. L., Malouin, F., Bravo, G., Paradis, G. (1998) Effects of the type of meniscal lesion on knee function. *Journal of Electromyography and Kinesiology*, 8: 411–422.

Moon, M. S., Kim, J. M., Ok, I. Y. (1984) The normal and regenerated meniscus in rabbits, morphologic and histologic studies. *Clin Orthop & Related Res.*, 182:264-269.

Mosher, T. J., Liu, Y. and Torok, C. M. (2010) Functional cartilage MRI T2 mapping: evaluating the effect of age and training on knee cartilage response to running. *Osteoarthritis and Cartilage*, 18(3): 358-364.

Mow, V.C., Kuei S.C., Lai W.M., Armstrong C.G. (1980a) Biphasic creep and stress relaxation of articular cartilage in compression: theory and experiments. *J Biomech Eng*, 102:73-84.

Mow, V. C., Lai, W. M. (1980b) Recent developments in synovial joint biomechanics. *SIAM Rev*., 22:275–317.

Mow, V. C., Gibbs, M. C., Lai, W. M., Zhu, W. B., Athanasiou, K. A. (1989) Biphasic indentation of articular cartilage II a numerical algorism and an experimental study. *J. Biomechanics*, 22 (8/9): 853-861.

Mow, V. C., Ratcliffe, A. (1992) Cartilage and diarthrodial joints as paradigms for hierarchical materials and structures. *Biomaterials*, 13 (2): 67-97.

Mow, V. C., Ateshian, G. A.. (1997). Friction, lubrication and wear of diarthrodial joints. In *Basic Orthopaedic Biomechanics*, edited by Mow, V. C. and Hayes, W. C., New York, Raven Press.

Mow, V. C., Hayes, W. C. (1997) *Basic Orthopaedic Biomechanics*. New York, Raven Press..

Mow, V.C. and Huiskes, R. (2005) *Basic orthopaedic biomechanics and mechano-biology* (third edition).

Muir, H. (1983) Proteoglycans as organizers of the intercellular matrix. *Biochem. Soc. Trans*., 11: 613-622.

Mukherjee, N. and Waynee, J. S. (1998) Loading sharing between solid and fluid phases in articular cartilage: I- experimental determination of in situ mechanical conditions in a porcine knee. *J. Biomech. Eng*., 120: 614-619.

Nakano, T., Thompson, J. R. , Aherne, F. X. (1986) Distribution of glycosaminoglycans and the nonreducible collagen crosslink, pyridinoline in procine menisci. *Can J Vet Res*. 50:532-536.

Nakata, K., Shino, K., Hamada, M., Mae, T., *et al*. (2001) Human meniscus cells. Characterization of the primary culture and use for tissue engineering. *Clin Orthop & Related Res*., 391S: s208-s218.

Narmoneva, D. A., Wang, J. Y., Setton, L. A. (2001) A noncontacting method for material property determination for articular cartilage from osmotic loading. *Biophysical J*., 81: 3066-3076.

Newbould, R. D., Miller, S. R., Tielbeek, J. A. W., *et al*. (2012) Reproducibility of sodium MRI measures of articular cartilage of the knee in osteoarthritis. *Osteoarthritis and Cartilage*, 20: 29-35.

Nieminen, M. T., Rieppo, J., Toyras, J., *et al*. (2001) T2 relaxation reveals spatial collagen architecture in articular cartilage: a comparative quantitative MRI and polarized light microscopic study. *Magnetic Resonance in Medicine*, 46:487–493.

Nisell, R. (1985) Mechanics of the knee: a study of joint and muscle load with clinical applications. *Acta Orthop Scand*, 56: [Supp] 216.

Nishimura, I., Muragaki, Y., Olsen, B. R. (1989) Tissue-specific forms of type IX collagen-proteoglycan arise from the use of two widely separated promoters. *J. Biol. Chem.*, 264: 20033-20041.

Noble, J., Hamblen, D. L. (1975) The pathology of the degenerate meniscus lesion. *J Bone Joint Surg. Br.*, 57: 180-186.

Nordin, M., Frankel, V. H. (2001) *Basic Biomechanics of the Musculoskeletal System*. Philadelphia; Lippincott Williams & Wilkins.

Northwood, E., Fisher, J. & Kowalski, R. (2007) Investigation of the friction and surface degradation of innovative chondroplasty materials against articular cartilage. *Proc Inst Mech Eng [H]: Engineering in Medicine*, 221: 263-279.

Noto, A., Beltran, J. and Mosure, J. (1986) High resolution MRI of the knee in humans and experimental animals. *Magnetic Resonance Imaging*, 4(2): 185.

Noyes, F. R., Barber-Westin, S. D. (2000) Arthroscopic repair of meniscus tears extending into the avascular zone with or without anterior cruciate ligament reconstruction in patients 40 years of age and older. *Arthroscopy*, 16: 822 –829 (abstract).

Noyes, F. R., Barber-Westin, S. D., Rankin, M. (2004) Meniscal transplantation in symptomatic patients less than fifty years old. *J Bone Joint Surg Am*, 86: 1392-1404.

Nugent, A. E., Reiter, D. A., Fishbein, K. W., McBurney, D. L., *et al*. (2010) Characterization of ex vivo-generated bovine and human cartilage by immunohistochemical, biochemical, and magnetic resonance imaging analyses. *Tissue Engineering, Part A*, 16(7): DOI: 10.1089/ten.tea.2009.0717.

Oei, E. H. G., Nikken, J. J., Verstijnen, A. C. M., Ginai, A. Z., Hunink, M. G. M. (2003) MR imaging of the menisci and cruciate ligaments: a systematic review. *Radiology*, 837-848.

Omoumi, P., Bydder, G., Znamirowski, R. M., *et al*. (2010) Infrastructure of menisci with MR imaging. The website of Carnegie Mellon University. eta2.bio.cmu.edu/ISMRM/.../files/3180_7258.pdf

Pakin, S. K., Cavalcanti, C., *et al*. (2006) Ultra-high-field MRI of knee joint at 7.0T: preliminary experience. *Academic Radiology*, 13(9): 1135-1142.

Park, S., Krishnan, R., Nicoll, S. B., Ateshian, G. A. (2003) Cartilage interstitial fluid load support in unconfined compression. *J Biomech*, 36: 1785-1796.

Pauli, C., Grogan, S. P., Patil, S., Otsuki, S., *et al*. (2011) Macroscopic and histopathologic analysis of human knee menisci in aging and osteoarthritis. *Osteoarthritis and Cartilage*, doi:10.1016/j.joca.2011.05.008.

Peterfy, C. G., Guermazi, A., Zaim, S., Tirman, P. F. J., Miaux, Y., White, D., *et al*. (2004) Whole-organ magnetic resonance imaging score (WORMS) of the knee in osteoarthritis. *Osteoarthritis Cartilage*, 12:177-190.

Peterfy, C. G., Gold, G., Eckstein, F. (2006) MRI protocols for whole-organ assessment of the knee in osteoarthritis. *Osteoarthritis and Cartilage*, 14: A95-A111.

Peters, T.J., Smillie I.S. (1972) Studies on the chemical composition of the menisci of the knee joint with special reference to the horizontal cleavage lesion. *Clin Orthop & Related Res*., 86: 245-252.

Petersen, W. and Tillmann, B. (1995) Age-related blood and lymph supply of the knee menisci. *Acta Orthopaedica Scandinavia*, vol. 66, p. 308-312.

Petersen, W., Tillmann, B. (1998) Collagenous fibril texture of the human knee joint menisci. *Anat. Embryol*., 197: 317-324.

Pham, A. and Hull, M. L. (2007) Dehydration rates of meniscus and articular cartilage in vitro using a fast and accurate laser-based coordinate digitizing system. *J Biomechanics*, 40: 3223-3229.

Pickard, J., Ingham, E., Egan, J., Fisher, J. (1998) Investigation into the effect of proteoglycan molecules on the tribological properties of cartilage joint tissues. *Proc. Instn Mech Engrs*, 212 (H): 177-182.

Pineda, S., Pollack, A., Stevenson, S., *et al*. (1992) A semiquantitative scale for histologic grading of articular cartilage repair. *Acta Anat*.,143: 335-340.

Proctor C.S., *et al*. (1989) Material properties of the normal medial bovine meniscus. *J. of Orthop. Res*., 7:771-782.

Purcell, E. M., Torry, H. C, Pound, C. V. (1946) Resonance absorption by nuclear magnetic moments in a solid. *Phys. Rev.*, 69: 37.

Ralphs, J.R. and Benjamin, M. (1994) Review, The joint capsule: structure, composition, ageing, disease. *J. Anat*., 184:503-509.

Rath, E., Richmond, J. C., Yassir, W., Albright, J. D., Gundogan, F. (2001) Meniscal allograft transplantation: two- to eight-year results. *Am. J. Sports Med*., 29: 410-414.

Record, R. D., Hillegonds, D., Simmons, C., Tullius, R., Rickey, F. A., Elmore, D., Badylak, S. F. (2001) In vivo degradation of ^{14}C-labeled small intestinal submucosa (SIS) when used for urinary bladder repair. *Biomaterials*, 22: 2653-2659.

Regatte, R. R. and Schweitzer, M. E. (2007) Ultra-high-field MRI of the musculoskeletal system at 7.0T. *J. Magn. Reso. Imaging*, 25: 262-269.

Reicher, M. A., Bassett, L. W. and Gold, R. H. (1985) High resolution MRI of the knee joint: pathologic correlations. *AJR*, 145: 903-909.

Reicher, M. A., Hartzman, S., Duckwiler, G. R., Bassett, L. W., Anderson, L. J., Gold, R. H. (1986) Meniscal injuries: detection using MR imaging. *Radiology*, 159: 753-757.

Reiter, D. A., Irrechukwu, O., Lin, P. C., Moghadam, S., Thaer, S. V., Pleshko, N., Spencer, R. G. (2012) Improved MR-based characterization of engineered cartilage using multiexponential T2 relaxation and multivariate analysis. *NMR in Biomedicine*, 25(3): 476-488.

Remesz, O. (2007) File: vertical mattress suture. Wikimedia, link:

http://commons.wikimedia.org/wiki/File:Vertical_mattress_suture.svg.

Robinson, E. M., Mackenzie, I. S., Freemont, A., Jasani, M. K. (1988) High resolution nuclear magnetic resonance imaging of pig knees at 4.7T. *Magnetic Resonance Imaging*, 6: 591-594.

Rodeo, S. A. (2007) Meniscus transplantation and cartilage resurfacing: considerations, indications, and approach. In: Williams, R. J. (edited) *Cartilage Repair Strategies*. New Jersey: Humana Press. Page: 271-282.

Rodkey, W. G., Briggs, K. K., Steadman, J. R., Hawkins, S. (2008) Survivorship of collagen meniscus implants (CMI) compared to meniscectomy only: a 5-year analysis in chronic knee patients. *Osteoarthritis and Cartilage*, 16 (Suppl. 4): s200-s201.

Roeddecker, K., Muennich, U., Nagelschmidt, M. (1994) Meniscal healing: a biomechanical study. *J. Surg. Res*., 56: 20-27.

Roberts, R. O. (2004) Bull's handbook of sports injuries (2nd ed.).

Roemer, F. W., Kwoh, C. K., Hannon, M. J., Crema, M. D., Moore, C. E., *et al*. (2011) Semiquantitative assessment of focal cartilage damage at 3 T MRI: A comparative study of dual echo at steady state (DESS) and intermediate-weighted (IW) fat suppressed fast spin echo sequences. *European Journal of Radiology*, 80: e126-e131.

Rosenberg, L. (1971) Chemical basis for the histological use of Safranin O in the study of articular cartilage. *J. Bone Joint Surg. Am*., 53:69-82.

Roughley, P. J., White, R. J. (1992) The dermatan sulfate proteoglycans of the adult human meniscus. *J Orthop. Res*., 10: 631-637.

Rubenstein, J. D., Kim, J. K., Morova-Protzner, I., Stanchev, P. L., Henkelman, R. M. (1993) Effects of collagen orientation on MR imaging characteristics of bovine articular cartilage. *Radiology*,188:219–226.

Ryu, K. N., Kim, I. S., Kim, E. J., *et al*. (1998) MR imaging of tears of discoid lateral menisci. *Am J Roentgenol*, 171(4): 963–967.

Sarma, A. V., Powell, G. L., LaBerge, M. (2001) Phospholipid composition of articular cartilage boundary lubricant. *J Orthop Res*., 19 (4): 671-676.

Sandell, L. J., Morris, N., Robbins, J. R., *et al*. (1991) Alternatively spliced type II procollagen mRNA define distinct populations of cells during vertebral development: differential expression of the amino-propeptide. *J. Cell Biol*., 114: 1307-1319.

Schmidt, M. B., Mow, V. C., Chun, L. E., Eyre, D. R. (1990) Effects of proteoglycans extraction on the tensile behavior of articular cartilage. *J Orthop Res*., 8 (3): 353-363.

Schumacher, B. L., Schmidt, T. A., Voegtline, M. S., *et al*. (2005) Proteoglycan 4 (PRG4) synthesis and immunolocalization in bovine meniscus. *J Orthop. Res*., 23: 562-568.

Seedhom, B. B., Dowson, D., Wright, V. (1974) Functions of the menisci. A preliminary study. *J. Bone Joint Surg. (Br)*, 56 B: 381-382.

Seedhom, B. B. (1979) Transmission of the load in the knee joint with special reference to the role of the menisci. *Engineering in Medicine*, 8 (No. 4): 207-219.

Sergerie, K., Lacoursiere, M., Levesque, M., *et al*. (2009) Mechanical properties of the porcine growth plate and its three zones from unconfined compression tests. *J. Biomechanics*, 42: 510-516.

Setton, L. A., Zhu, W., Mow, V. C. (1993) The biphasic poroviscoelastic behavior of articular cartilage: role of the surface zone in governing the compressive behavior. *J. Biomechanics*, 26(4/5): 581-592.

Shapiro, E. M., Borthakur, A., Gougoutas, A., Reddy, R. (2002) 23Na MRI accurately measures fixed charge density in articular cartilage. *Magn Reson Med*, 47(2): 284-291.

Shelbourne, K. D., Gray, T. (2000) Results of anterior cruciate ligament reconstruction based on meniscus and articular cartilage status at the time of surgery. Five- to 15-yr evaluations. *Am. J. Sports Med*., 28:446-452.

Sigurdsson, U., Tiderius, C. J., Siversson, E., *et al*. (2010) 3-D delayed gadolinium-enhanced MRI of cartilage (3-D dgemric) of knee meniscus and

cartilage: a dose response and time study in healthy volunteers. *Osteoarthritis and Cartilage*, 18 supplement 2: S218.

Simon, W. H. (1970) Scale Effects in Animal Joints. I. Articular Cartilage Thickness and Compressive Stress. *Arthritis and Rheum*, 13, 244-255.

Simon, W. H. (1971) Wear properties of articular cartilage in vitro. *J. Biomech*., 4:379–89.

Sittek, H., Eckstein, F., Gavazzeni, A., *et al*. (1996) Assessment of normal patellar cartilage volume and thickness using MRI: an analysis of currently available pulse sequences. *Skeletal Radiol*., 25:55–62.

Skaggs, D. L., Warden, W. H., Mow, V. C. (1994) Radial tie fibers influence the tensile properties of the bovine medial meniscus. *J. Orthopaedic Research*, 12: 176-185.

Soejima, T., Horibe, S., Abe, T., Tanaka, N., Noguchi, J., Maeda, T., Inoue, A. (1997) Deterioration of the femoral articular surface after meniscal repair evaluated by second-look arthroscopy: comparison with partial meniscectomy. *The Knee*, 4: 215-220.

Specke, V., Rubant, S., Denner, J. (2001) Productive Infection of Human Primary Cells and Cell Lines with Porcine Endogenous Retroviruses. *Virology*, 285: 177-180.

Spilker, R. L., Donzelli, P. S., Mow, V. C. (1992) A transversely isotropic biphasic finite element model of the meniscus. *J. Biomech*., 25:1027-1045.

Stahl, R., BBlumenkrantz, B. S., Carballido-Gamio, J., Zhao, S., Munoz, T., *et al*. (2007) MRI-derived T2 relaxation times and cartilage morphometry of the tibio-femoral joint in subjects with and without osteoarthritis during a 1-year follow-up. *Osteoarthritis and Cartilage*, 15(11): 1225-1234.

Stanescu, V. (1990) The small proteoglycans of cartilage matrix. *Semi. Arth. Rheum., Suppl*., 1: 51-64.

Stapleton, T. W., Ingram, J., Fisher, J., Ingham, E. (2008) Biocompatibility of an acellular porcine meniscal scaffold. *Tissue Engineering Part A*, 14 (5): 812.

Steadman, J. R. & Rodkey, W. G. (2005). Tissue-engineered collagen meniscus implants: 5- to 6-year feasibility study results. *Arthroscopy*, 21: 515-525 (abstract).

Stehling, C., Souza, R. B., Graverand, M. H., *et al*. (2011) Loading of the knee during 3.0 T MRI is associated with significantly increased medial meniscus extrusion in mild and moderate osteoarthritis. *Eur. J Radiol*. , doi:10.1016/j.ejrad.2011.05.027.

Stoller D. W., Martin, C., Crues, J. V. III, Kaplan, L, *et al*. 1987 Meniscal tears of the knee: accuracy of MR imaging. *Radiology*, 163: 731-735.

Stone, K. R., Rodkey, W. G., Webber, R., *et al*. (1990) Future directions, collagen-based prostheses for meniscal regeneration. *Clin. Orthop. and Relat. Res.*, 252: 129-135.

Stone, K. R., Rodkey, W. G., *et al*. (1992) Meniscal regeneration with copolymeric collagen scaffolds, in vitro and in vivo studies evaluated clinically, histologically, and biochemically. *The American Journal of Sports Medicine*, 20:104-111.

Stone, K. R., Stoller, D. W., Irving, S. G., *et al*. (1994) 3D MRI volume sizing of knee meniscus cartilage. *Arthroscopy: The Journal of Arthroscopic and Related Surgery*, 10(6): 641-644.

Stone, K. R. (1996). Meniscus replacement. *Clinics in Sports Medicine*, 15: 557-571.

Stone, K. R., Steadman, J. R., Rodkey, W. G., Li, S. T. (1997) Regeneration of meniscal cartilage with use of a collagen scaffold, analysis and preliminary data. *J. Bone Joint Surg. Am*., 79: 1770-1777.

Sun, Y., Berger, E. J., Zhao, C. F., An, K. N., *et al*. (2006) Mapping Lubricin in canine musculoskeletal tissues. *Connective Tissue Res*., 47: 215-221.

Swann, D. A., Slayter, H. S., Silver, F. H. (1981) The molecular structure of lubricating glycoprotein-I, the boundary lubricant for articular cartilage. *J. Biolo. Chem*., 256 (11): 5921-5925.

Swann, D. A., Silver, F. H., Slayter, H. S., Stafford, W., Shore, E. (1985) The molecular structure and lubricating activity of lubricin isolated from bovine and human synovial fluids. *Biochem J*., 225:195–201.

Sweigart, M. A., Aufderheide, A. C., Athanasiou, K. A. (2003) Fibrochondrocytes and their use in tissue engineering of meniscus. In: Topics in *Tissue Engineering*, Edited by: Ashammakhi, N. and Farretti, P., University of Oulu.

Takeda, Y., Ikata, T., Yoshida, S., Takai, H., Kashiwaguchi, S. (1998) MRI high-signal intensity in the menisci of asymptomatic children. *J. Bone Joint Surg. Br*, 80: 463-467.

Tanaka, T., Fujii, K., Kumagae, Y. (1999) Comparison of biochemical characteristics of cultured fibrochondrocytes isolated from the inner and outer regions of human meniscus. *Knee Surg., Sports Traumatol., Arthrosc*., 7 :75–80.

Tapper, E. M., Hoover, N. W. (1969) Late results after meniscectomy. *J. Bone Joint Surg. Am*, 51: 517-609.

Taylor, W. R., Heller, M. O., Bergmann, G., Duda, G. N. (2004) Tibio-femoral loading during human gait and stair climbing. *Journal of Orthopaedic Research*, 22: 625-632.

Taylor, W. R., Ehrig, R. M., Heller, M. O., Schell, H. (2006) Tibio-femoral joint contact forces in sheep. *Journal of Biomechanics*, 39: 791-798.
The sheep knee force data.

Thompson, Jr. R. C., Oegema, Jr. T. R. (1979) Metabolic activity of articular cartilage in osteoarthritis. An in vitro study. *J Bone Joint Surg Am*, 61:407–16.

Tienen, T. G., Buma, P., Scholten, J. G., van Kampen, A., Veth, R. P., Verdonschot, N. (2005) Displacement of the medial meniscus within the passive motion characteristics of the human knee joint: an RSA study in human cadaver knees. *Knee Surg Sports Traumatol Arthrosc*, 13(4): 287–92.

Tortora, G. and Derrickson B. (2006) *Principles of Anatomy and Physiology*. John Wiley & Sons.

Tregonning, R. J. A. (1983) Closed partial meniscectomy, early results for simple tears with meniscal symptoms. *J. Bone Joint Surg. Br*, 65 (4): 378-382.

Tsai, P. H., Chou, M. -C., Lee, H. -S., *et al*. (2009) MR T2 values of the knee menisci in the healthy young population: zonal and sex differences. *Osteoarthritis and Cartilage*, 17: 988-994.

Valiyaveettil, M., Mort, J. S., McDevitt, C. A. (2005) The Concentration, Gene Expression, and Spatial Distribution of Aggrecan in Canine Articular Cartilage, Meniscus, and Anterior and Posterior Cruciate Ligaments: A New Molecular Distinction Between Hyaline Cartilage and Fibrocartilage in the Knee Joint. *Connective Tissue Research*, 46: 83-91.

Van Arkel, E. R., De Boer, H. H. (1995) Human meniscal transplantation Preliminary results at 2 to 5-year follow-up. *J. Bone Joint Surg. Br*, 77: 589-95.

Van Mourik, J. B. A., Weerdenburg, J. P. G., Verhaar, J. A. N. (2001) Magnetic resonance imaging of multiple epiphyseal dysplasia (type 2) of the knee. *Radiography*, 7: 61-64.

Vedi, V., Williams, A., Tennant, S. J., *et al*. (1999) Meniscal movement. An in-vivo study using dynamic MRI. *J. Bone Joint Surg. Br*, 81: 37-41.

Verdonk, P. C. M., Van Laer, M. E. E., Verdonk, R. (2008) Meniscus replacement: fron allograft to tissue engineering. *Sports Ortho. and Traumatology*, 24(2): 78-82.

Voloshin, A. S. and Wosk, J. (1983) Shock absorption of the meniscectomized and painful knees: a comparative in vivo study. *J. Biomed. Eng*., 5: 157-161.

Walker, P. S., Erkman, M. J. (1975) The role of the menisci in force transmission across the knee. *Clin Orthop & Related Res*., 109: 184-192.

Wang, A., Essner, A., Polineni, V. K., Stark, C., Dumbleton, J. H. (1998). Lubrication and wear of ultra-high molecular weight polyethylene in total joint replacements. *Tribology International*, 31: 17-33.

Wang, M., McCann, L., Radjenovic, A., Tanner, S., Ries, M., Fisher, J., Jin, Z. (2008) Quantitative MRI study of cartilage tribology. Poster presentation for the 2nd OA Imaging Workshop, Boston, US.

Wang, M., Radjenovic, A., Stapleton, T. W., Venkatesh, R., Williams, S., Ingham, E., Fisher, J., Jin, Z. (2010) A novel and non-destructive method to examine meniscus architecture using 9.4 Tesla MRI. *Osteoarthritis and Cartilage*, 18: 1417-1420.

Ward, K. M., Aletras, A. H., Balaban, R. S. (2000) A new class of contrast agents for MRI based on proton chemical exchange dependent saturation transfer (CEST). *Journal of Magnetic Resonance*, 143: 79–87.

Wasser, L., Knorr, J., Accadbled, F., *et al*. (2011) Arthroscopic treatment of discoid meniscus in children Clinical and MRI results. *Orthopaedics & Traumatoology: Surgery & Research*, 97: 297-303.

Webber, R. J., Harris, M. G., Hough, A. J. (1985) Cell culture of rabbit meniscal fibrochondrocytes: proliferative and synthetic response to growth factors and ascorbate. *Journal of Orthopaedic Research*, 3: 36-42.

Weidow, J., Pak, J., Karrholm, J. (2002) Different patterns of cartilage wear in medial and lateral gonarthrosis. *Acta. Orthop. Scand*., 73 (3): 326–329.

Werner, F. W., Ayers, D. C., Maletsky, L. P., Rullkoetter, P. J. (2005) The effect of valgus/varus malalignment on load distribution in total knee replacements. *J. Biomechanics*, 38: 349-355.

Wheaton, A. J., Borthakur, A., Shapiro, E. M., Regatte, R. R., Akella, S. V. S., Kneeland, J. B., *et al*. (2004) Proteoglycan loss in human knee cartilage: quantitation with sodium MR imaging feasibility study. *Radiology*, 231:900-905.

Whiting, W. C., Zernicke, R. F. (1998) *Biomechanics of Musculoskeletal Injury*. Publisher: Human Kinetics.

Williams, A. and Logan, M. (2004) Understanding Tibio-femoral motion. *The Knee*, 11(2): 81-88.

Williams, A., Gillis, A., McKenzie, C., *et al*. (2004) Glycosaminoglycan Distribution in Cartilage as Determined by Delayed Gadolinium-Enhanced MRI of Cartilage (dGEMRIC): Potential Clinical Applications. *AJR*, 182: 167-172.

Wilson, W., van Rietbergen, B., van Donkelaar, C. and Huiskes, R. (2003) Pathways of load-induced cartilage damage causing cartilage degeneration in the knee after meniscectomy. *Journal of Biomechanics*, 36: 845-851.

Whipple, R. R., Wirth, C. J., Mow, V. C. (1985) Anisotropic and zonal variations in the tensile properties of the meniscus. *Orthop. Trans*., 10:367.

Wood, D. J., Minns, R. J. & Strover, A. (1990). Replacement of the rabbit medial meniscus with a polyester-carbon fibre bioprosthesis. *Biomaterials*, 11: 13-16.

Wright, V., Dowson, D. (1976) Lubrication and cartilage. *J. Anat*., 121 (1): 107-118.

Yao, J., Lancianese, S. L., Hovinga, K. R., Lee, J., Lerner, A. L. (2008) Magnetic Resonance Image analysis of meniscal translation and tibio-menisco-femoral contact in deep knee flexion. *J. Orthopaed. Res*., 673-84

Yildirim, G., Walker, P. S., Sussman-Fort, J., *et al*. (2007) The contact locations in the knee during high flexion. *The Knee*, 14: 379-384.

Zappone, B., Greene, G. W., Oroudjev, E., Jay, G. D., Israelachvili, J. N. (2008) Molecular aspects of boundary lubrication by human lubricin: effect of disulfide bonds and enzymatic digestion. *Langmuir*, 24:1495–508.

Zazirnyi, I. M. (1999) The current concepts of the etiology and pathogenesis of osteoarthrosis. *Lik Sprava* (2): 7-12.